

AD-A151 981

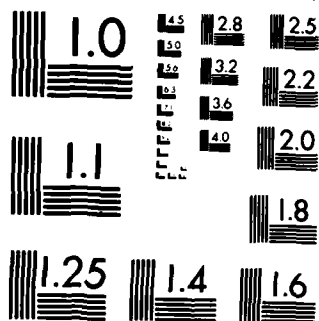
PARTICLE SHAPE CHARACTERIZATION(U) BOEING AEROSPACE CO
SEATTLE WA C D CAPPS OCT 84 N00014-83-C-2151

1/2

UNCLASSIFIED

F/G 20/6

NL



MICROCOPY RESOLUTION TEST CHART
NATIONAL BUREAU OF STANDARDS-1963-A

12

BOEING

Final Report

Particle Shape Characterization

Contract N00014-83-C-2151

AD-A151 981

DTIC FILE COPY

DTIC
ELC
MAR 27 1985
S
A

This document has been approved
for public release and sale; its
distribution is unlimited.

84 11 19 106

12

Final Report
Particle Shape Characterization
Contract N00014-83-C-2151

Submitted to
United States Navy
Naval Air Systems Command
Washington, D.C. 20361

October 1984

Boeing Aerospace Company
Seattle, Washington 98124

12

UNCLASSIFIED

SECURITY CLASSIFICATION OF THIS PAGE (When Data Entered)

REPORT DOCUMENTATION PAGE		READ INSTRUCTIONS BEFORE COMPLETING FORM
1. REPORT NUMBER	2. GOVT ACCESSION NO.	3. RECIPIENT'S CATALOG NUMBER
4. TITLE (and Subtitle) PARTICLE SHAPE CHARACTERIZATION		5. TYPE OF REPORT & PERIOD COVERED Final Report
		6. PERFORMING ORG. REPORT NUMBER
7. AUTHOR(s) C. D. Capps		8. CONTRACT OR GRANT NUMBER(s) N00014-83-C-2151
9. PERFORMING ORGANIZATION NAME AND ADDRESS Boeing Aerospace Company P.O. Box 3999 Seattle, WA 98124		10. PROGRAM ELEMENT, PROJECT, TASK AREA & WORK UNIT NUMBERS
11. CONTROLLING OFFICE NAME AND ADDRESS Naval Air Systems Command Washington, D.C. 20361		12. REPORT DATE October 1984
		13. NUMBER OF PAGES 90
14. MONITORING AGENCY NAME & ADDRESS (if different from Controlling Office)		15. SECURITY CLASS. (of this report) UNCLASSIFIED
		15a. DECLASSIFICATION/DOWNGRADING SCHEDULE
16. DISTRIBUTION STATEMENT (of this Report) <div style="border: 1px solid black; padding: 5px; width: fit-content; margin: 10px auto;"> This document has been approved for public release and its distribution is unlimited. </div>		
17. DISTRIBUTION STATEMENT (of the abstract entered in Block 20, if different from Report)		
18. SUPPLEMENTARY NOTES		
19. KEY WORDS (Continue on reverse side if necessary and identify by block number) Nonspherical particles Scattering Particle sizing Mie theory		
20. ABSTRACT (Continue on reverse side if necessary and identify by block number) An experimental apparatus was developed that stably suspends micron particles. Differential scattering cross sections were successfully measured in two orthogonal directions. Although the scattering data visibly change as a function of particle shape and size, a reliable computational method for extracting particle size from the data has not yet been found.		

UNCLASSIFIED

CONTENTS

<u>Section</u>		<u>Page</u>
	Figures	ii
	Tables	iv
I	Introduction	1
II	Experimental Arrangement	2
III	Particle Characterization	2
IV	Description of Data	5
V	Data Analysis	7
VI	Summary and Conclusions	12
	References	13

✓
Notes on file

A-1



FIGURES

<u>No.</u>		<u>Page</u>
1	Schematic Diagram of System	14
2	Photograph of System	15
3	Photographs of Particles 1, 2, and 3 in Electrodynamic Balance	16
4	Photographs of Particles 4, 5, and 6 in Electrodynamic Balance	17
5	Photomicrographs of Particle Samples	18
6	Image Geometry	19
7	Differential Scattering Cross Section, Channel A, Particle 1, Sample 1	20
8	Differential Scattering Cross Section, Channel B, Particle 1, Sample 1	21
9	Differential Scattering Cross Section, Channel A, Particle 1, Sample 2	22
10	Differential Scattering Cross Section, Channel B, Particle 1, Sample 2	23
11	Differential Scattering Cross Section, Channel A, Particle 1, Sample 3	24
12	Differential Scattering Cross Section, Channel B, Particle 1, Sample 3	25
13	Differential Scattering Cross Section, Channel A, Particle 2, Sample 1	26
14	Differential Scattering Cross Section, Channel B, Particle 2, Sample 1	27
15	Differential Scattering Cross Section, Channel A, Particle 2, Sample 2	28
16	Differential Scattering Cross Section, Channel B, Particle 2, Sample 2	29
17	Differential Scattering Cross Section, Channel A, Particle 2, Sample 3	30
18	Differential Scattering Cross Section, Channel B, Particle 2, Sample 3	31
19	Differential Scattering Cross Section, Channel A, Particle 3, Sample 1	32
20	Differential Scattering Cross Section, Channel B, Particle 3, Sample 1	33
21	Differential Scattering Cross Section, Channel A, Particle 3, Sample 2	34
22	Differential Scattering Cross Section, Channel B, Particle 3, Sample 2	35
23	Differential Scattering Cross Section, Channel A, Particle 3, Sample 3	36
24	Differential Scattering Cross Section, Channel B, Particle 3, Sample 3	37
25	Differential Scattering Cross Section, Channel A, Particle 4, Sample 1	38
26	Differential Scattering Cross Section, Channel B, Particle 4, Sample 1	39
27	Differential Scattering Cross Section, Channel A, Particle 4, Sample 2	40
28	Differential Scattering Cross Section, Channel B, Particle 4, Sample 2	41
29	Differential Scattering Cross Section, Channel A, Particle 4, Sample 3	42
30	Differential Scattering Cross Section, Channel B, Particle 4, Sample 3	43
31	Differential Scattering Cross Section, Channel A, Particle 5, Sample 1	44
32	Differential Scattering Cross Section, Channel B, Particle 5, Sample 1	45
33	Differential Scattering Cross Section, Channel A, Particle 5, Sample 2	46

FIGURES (Continued)

<u>No.</u>		<u>Page</u>
34	Differential Scattering Cross Section, Channel B, Particle 5, Sample 2	47
35	Differential Scattering Cross Section, Channel A, Particle 5, Sample 3	48
36	Differential Scattering Cross Section, Channel B, Particle 5, Sample 3	49
37	Differential Scattering Cross Section, Channel A, Particle 6, Sample 1	50
38	Differential Scattering Cross Section, Channel B, Particle 6, Sample 1	51
39	Differential Scattering Cross Section, Channel A, Particle 6, Sample 2	52
40	Differential Scattering Cross Section, Channel B, Particle 6, Sample 2	53
41	Differential Scattering Cross Section, Channel A, Particle 6, Sample 3	54
42	Differential Scattering Cross Section, Channel B, Particle 6, Sample 3	55
43	Mie Theory Fit, Channel A, Particle 1, Sample 1 (subset of Fig. 7)	56
44	Mie Theory Fit, Channel B, Particle 1, Sample 1 (subset of Fig. 8)	57
45	Mie Theory Fit, Channel A, Particle 2, Sample 1 (subset of Fig. 13)	58
46	Mie Theory Fit, Channel B, Particle 2, Sample 1 (subset of Fig. 14)	59
47	Mie Theory Fit, Channel A, Particle 3, Sample 1 (subset of Fig. 19)	60
48	Mie Theory Fit, Channel B, Particle 3, Sample 1 (subset of Fig. 20)	61
49	Diffraction Theory Fit, Channel A, Particle 1, Sample 1 (data from Fig. 7)	62
50	Diffraction Theory Fit, Channel B, Particle 1, Sample 1 (data from Fig. 8)	63
51	Diffraction Theory Fit, Channel A, Particle 2, Sample 1 (data from Fig. 13)	64
52	Diffraction Theory Fit, Channel B, Particle 2, Sample 1 (data from Fig. 14)	65
53	Diffraction Theory Fit, Channel A, Particle 3, Sample 1 (data from Fig. 19)	66
54	Diffraction Theory Fit, Channel B, Particle 3, Sample 1 (data from Fig. 20)	67
55	Channel Cross Section Versus Particle Equivalent Radius	68
56	Total Cross Section Versus Particle Equivalent Radius	69
57	Channel A Cross Section Versus a Semi-Axis	70
58	Channel B Cross Section Versus b Semi-Axis	71
59	Scatter Plot, Channel B Versus Channel A, Particle 1, Sample 1	72
60	Scatter Plot, Channel B Versus Channel A, Particle 1, Sample 2	73
61	Scatter Plot, Channel B Versus Channel A, Particle 1, Sample 3	74
62	Scatter Plot, Channel B Versus Channel A, Particle 2, Sample 1	75
63	Scatter Plot, Channel B Versus Channel A, Particle 2, Sample 2	76

FIGURES (Concluded)

<u>No.</u>		<u>Page</u>
64	Scatter Plot, Channel B Versus Channel A, Particle 2, Sample 3	77
65	Scatter Plot, Channel B Versus Channel A, Particle 3, Sample 1	78
66	Scatter Plot, Channel B Versus Channel A, Particle 3, Sample 2	79
67	Scatter Plot, Channel B Versus Channel A, Particle 3, Sample 3	80
68	Scatter Plot, Channel B Versus Channel A, Particle 4, Sample 1	81
69	Scatter Plot, Channel B Versus Channel A, Particle 4, Sample 2	82
70	Scatter Plot, Channel B Versus Channel A, Particle 4, Sample 3	83
71	Scatter Plot, Channel B Versus Channel A, Particle 5, Sample 1	84
72	Scatter Plot, Channel B Versus Channel A, Particle 5, Sample 2	85
73	Scatter Plot, Channel B Versus Channel A, Particle 5, Sample 3	86
74	Scatter Plot, Channel B Versus Channel A, Particle 6, Sample 1	87
75	Scatter Plot, Channel B Versus Channel A, Particle 6, Sample 2	88
76	Scatter Plot, Channel B Versus Channel A, Particle 6, Sample 3	89
77	Correlation Coefficient Versus Equivalent Radius	90

TABLES

<u>No.</u>		<u>Page</u>
I	Particle Dimensions Derived From the Photographic Images	5
II	Particle Dimensions Derived From Fitting	9

I. INTRODUCTION

The increasing accuracy of precision guided munitions which use a variety of electro-optic sensors has led to renewed interest in obscuring aerosols that can be used to protect intended targets from these devices. The first generation of obscurants, some of which were developed in World War I, created a smokescreen by burning a material, such as phosphorus, or vaporizing a substance, like fuel oil, which then condensed into a fog. These two materials created an aerosol composed of spherical, liquid droplets that was very effective in attenuating light, i.e., targets could be effectively hidden from human observers. Recent developments in electro-optics have produced viewing, designating, and tracking devices that operate in the infrared as well as the visible region of the electromagnetic spectrum. The earlier generation of obscurants has been found to be relatively ineffective in the infrared so improved aerosols are now being sought.

In general, the particles comprising the earlier generation of obscurants were spherical. Nonspherical particles have, in some cases, been shown to possess more desirable properties, such as broader spectral effectiveness and more obscuration per unit mass. However, the theoretical problem of predicting the interaction of electromagnetic radiation with a particle of arbitrary size, shape, and index of refraction has not been solved for particles with a size on the order of the wavelength of the radiation. Thus, it is difficult to predict or interpret data from experiments conducted on nonspherical particles. The work reported herein addresses this problem with a phenomenological approach. An electrodynamic balance was built that stably suspends individual micron-sized particles. Individual spheres and nonspheres were suspended and photomicrographs were made of the particles while their scattering cross sections were measured in two orthogonal directions. The photographs and cross sections were then analyzed in a search for correlations between particle size and shape and the scattering cross section.

This report is organized as follows. Section II contains a description of the experimental apparatus. Photographs of the particles, measurement methodology, and resulting size parameters are presented in Section III. Differential scattering cross-section plots are shown in Section IV and analysis and results described in Section V. Finally, results and conclusions are summarized in Section VI.

II. EXPERIMENTAL ARRANGEMENT

The heart of the experimental apparatus is an electrodynamic balance¹ used to suspend individual, micron-sized particles. The particles are given a static charge with a high-voltage source, then held in a stable position with a quadrupole-shaped alternating field. A dc field is used to counteract the gravitational force; otherwise, the particles would oscillate about the central point.

The suspended particle was illuminated with a 50-mW helium neon laser beam focused with a 250-mm focal length lens to increase the flux on the particle. The scattered light was collected by two EG&G Reticon RL1024G arrays located about 7 cm from the particle. These linear arrays were oriented with their axes orthogonal to each other and with the virtual intersection at the center of the laser beam. A schematic diagram of the system is shown in Figure 1 and a photograph in Figure 2. The array electronics were adjusted so that each pixel integrated for 8 ms. The array clockouts were synchronized and the readouts were made simultaneously with a Nicolet 2090 digital storage oscilloscope. The digitized data were then transferred to a Hewlett Packard 9825A computer where they were stored on cassette tape for later analysis. The microscope system for photographing the suspended particles will be described in the following section.

III. PARTICLE CHARACTERIZATION

In order to relate the measured scattering cross section to particle shape, size, and orientation, it was necessary to photograph each particle in the suspension chamber at the time scattering data were recorded. A microscope was set up with its optical axis 30 deg from the incident laser beam direction. Due to the electrode geometry, a long working distance (~50 mm) objective was required, which limited the system resolution. A photograph of a stage micrometer with laser illumination showed that the system resolution on film was 8 μ m. The suspended particles were photographed on Polaroid Polachrome transparency film at a magnification of 18X. One benefit of using this film with monochromatic illumination is that the emulsion records the image as a series of lines. Since these lines in the emulsion run parallel to the film edges, a permanent and precise record of the particle's orientation is achieved. This feature is especially convenient as the transparency image must be magnified for measurement.

The images used for measurement are shown in Figures 3 and 4 with a transparency-to-print magnification of 125X.

A sample of six particles was used in this study: three spheres and three nonspheres. The spheres are from a sample of 10- to 15- μm -diameter Particle Information Services (PIS) glass spheres; the nonspheres are agglomerates of 1- to 3- μm -diameter PIS glass spheres. White light photomicrographs of samples of the particles are shown in Figure 5. Particles 1, 2, and 3 are individual sphere samples and Particles 4, 5, and 6 are agglomerates.

The images were analyzed for size and shape information in the following manner. The lines in the emulsion defined the x-direction, the perpendicular direction being y. The emulsion lines are spaced regularly 1.4 μm apart in the object space. Figure 6 shows how the images were measured and a two-dimensional reconstruction of the image area was created. The image area is given by

$$\begin{aligned}
 A &= \iint dx \, dy \\
 &= \sum_{n=1}^N (y_n - y_{n-1}) (x_{n2} - x_{n1}) \\
 &= \Delta \sum_{n=1}^N (x_{n2} - x_{n1})
 \end{aligned} \tag{1}$$

We can define the radius of a circle of equal area RE as a measure of the overall particle size:

$$RE = \sqrt{A/\pi} \tag{2}$$

If RE, sometimes called the zeroth moment, were the only descriptor of the particle, we would have no way of distinguishing a circular from a noncircular image. The first moments of the x and y coordinates, \bar{x} , \bar{y} , give the location of the object's "center of mass", information not related to its scattering properties:

$$\begin{aligned}\bar{x} &= \langle x \rangle = \frac{1}{A} \iint x \, dx \, dy \\ &= \frac{1}{2} \sum_{n=1}^N (x_{n2}^2 - x_{n1}^2) / \sum_{n=1}^N (x_{n2} - x_{n1})\end{aligned}\quad (3)$$

$$\begin{aligned}\bar{y} &= \langle y \rangle = \frac{1}{A} \iint y \, dx \, dy \\ &= \frac{A}{2} \sum_{n=1}^N (2n-1) (x_{n2} - x_{n1}) / \sum_{n=1}^N (x_{n2} - x_{n1})\end{aligned}\quad (4)$$

The second moments about axes passing through the "center of mass" and parallel to the coordinate axes will contain information on the deviation of the image from a circular shape. Since the scattering cross sections were also measured in the x and y directions, it seems logical to search for correlations between the scattering cross sections and these moments. The second moments, M_x and M_y , are given by

$$\begin{aligned}M_x &= \langle (x - \bar{x})^2 \rangle = \frac{1}{A} \iint (x - \bar{x})^2 \, dx \, dy \\ &= -\bar{x}^2 + \frac{1}{3} \sum_{n=1}^N (x_{n2}^3 - x_{n1}^3) / \sum_{n=1}^N (x_{n2} - x_{n1})\end{aligned}\quad (5)$$

$$\begin{aligned}M_y &= \langle (y - \bar{y})^2 \rangle = \frac{1}{A} \iint (y - \bar{y})^2 \, dx \, dy \\ &= -\bar{y}^2 + \frac{A^2}{3} \sum_{n=1}^N (3n^2 - 3n+1) (x_{n2} - x_{n1}) / \sum_{n=1}^N (x_{n2} - x_{n1})\end{aligned}\quad (6)$$

The image can be related to an equivalent ellipse through the second moments. Given an ellipse with its "center of mass" at the origin and semi-axes a in the x-direction and b in the y-direction, the boundary equation, area, and moments are:

$$\frac{x^2}{a^2} + \frac{y^2}{b^2} = 1, \quad \text{Area} = \pi ab, \quad \langle x^2 \rangle = \frac{a^2}{4} \quad \text{and} \quad \langle y^2 \rangle = \frac{b^2}{4} \quad (7)$$

Combining Equations 5, 6, and 7 gives the semi-axes of the equivalent ellipse in terms of the moments of the reconstructed image:

$$\begin{aligned} a &= 2\sqrt{M_x} \\ b &= 2\sqrt{M_y} \end{aligned} \quad (8)$$

Table I lists the dimensions for the six particle images reported in this study. Note that Particle 3, which is from a sample of spheres, has an aspect ratio that differs significantly from 1.0. Either it was nonspherical or the dc field was not precisely adjusted and the particle oscillated in the y-direction. This question will be addressed in the following sections where the scattering cross sections of the particles are presented and analyzed.

Table I
Particle Dimensions Derived From the Photographic Images

Particle	A (μm^2)	RE (μm)	a (μm)	b (μm)	b/a
1	231	8.6	8.8	8.7	0.99
2	141	6.7	7.6	6.2	0.82
3	226	8.5	6.6	11.4	1.73
4	506	12.7	10.9	15.1	1.39
5	395	11.2	20.2	6.5	0.32
6	757	15.5	12.8	19.0	1.48

IV. DESCRIPTION OF DATA

As shown in Figure 1, the linear photodiode arrays were arranged in an orthogonal configuration. For convenience, we shall refer to the array with its axis parallel to the x-axis defined in the previous section as Channel A and the one parallel to the y-axis as Channel B. The laser beam was linearly polarized in a direction parallel to the y-axis. However, there were no polarization analyzers in front of the detectors. The

arrays lay in a plane perpendicular to the laser beam 7.2 cm from the particle, the detector element closest to the beam center being 1.3 cm from this reference. As the detector element spacing on these devices was 25.4 μm and there were 1024 elements, the scattering angles covered were from 10 to 28 deg with 0.018-deg resolution.

To obtain an absolute calibration for the system, the laser beam was spread out into a large, relatively uniform pattern using a spatial filter. The system response was recorded on computer tape while a Laser Precision RK5100 radiometer measured the flux incident on the arrays. Calibrated neutral density filters were placed in the beam to check the linearity of the system response. Later, a statistical analysis of the recorded data was made to determine responsivity and noise levels of the whole system. The system noise equivalent irradiance was found to be 0.1 $\mu\text{W}/\text{cm}^2$ and for large signal levels the relative uncertainty was 5%.

The flux incident on the particle was determined by placing a 25- μm -diameter pinhole aperture at the location of the particle and measuring the power in front of and behind it. Moving the aperture sideways and measuring the resulting power as a function of position showed that the beam profile was approximately Gaussian. Assuming it was exactly Gaussian yielded a derived $1/e^2$ diameter of 150 μm and a flux of 5 $\mu\text{W}/\mu\text{m}^2$ at the beam center.

The differential scattering cross section $d\sigma/d\Omega$ in the direction of the detector is defined by

$$\begin{aligned} \frac{d\sigma}{d\Omega} &= \frac{(\text{scattered flux on detector}) (\text{detector area normal to flux})}{(\text{incident flux}) (\text{solid angle subtended by detector})} \\ &= \frac{I z^2}{I_0 \cos^2 \theta} \quad (\mu\text{m}^2/\text{sr}) \end{aligned} \quad (9)$$

where I = measured scattered flux ($\mu\text{W}/\text{cm}^2$)
 θ = scattering angle
 z = distance from particle to detector plane
 $= 7.2 \text{ cm}$
 I_0 = flux incident on particle
 $= 5 \mu\text{W}/\mu\text{m}^2$

Figures 7 through 42 plot the measured differential scattering cross sections for both channels and each of the six particles. In addition, three cross-section measurements were made for each particle in order to evaluate the reproducibility of the measurements. Reproducibility was of special concern for nonspherical particles, where particle rotation could result in grossly changing cross sections. Visual examination of the results show that the cross sections were reproducible, indicating a stable orientation. Each plot contains the measurements from 1012 detectors; the results from the 12 detectors closest to the beam in each channel were eliminated because of noise contamination from the readout synchronization pulse. The differential scattering cross section is plotted in units of square microns per steradian and the scattering angle is in degrees. Note that some cross-section plots are slightly negative, due to the fact that background measured with no particle in the beam was subtracted from the scattering signal. With little or no signal, the differences in intrinsic noise samples caused negative values to appear. These data will be analyzed in the following section.

V. DATA ANALYSIS

The first attempt to interpret the data was to fit the curves from the spherical particles with Mie theory. If the particles were true spheres, there would be no cross polarization induced by the scattering, and Channel A would measure the perpendicular-polarized scattering and Channel B the parallel-polarized scattering. A numerical minimization routine was used to fit the data by varying an overall multiplication factor, the particle diameter, and the real index of refraction in the Mie theory, with the Mie cross sections calculated by the program DBMIE.² Due to computer time limitations, it was necessary to fit a subset of the data rather than the whole set. The data were reduced by selecting every 16th data point, giving a total sample of 64 points in each channel rather than 1012. The errors were calculated for each point using the parameters given in Section IV and the fit was performed by minimizing chi-square. It should be emphasized that Channels A and B were fit simultaneously with only one overall normalization parameter. The model that was fit to the data was:

$$\begin{aligned}\frac{d\sigma}{d\Omega_A} &= A k^{-2} |S_1(R, N, \theta)|^2 \\ \frac{d\sigma}{d\Omega_B} &= A k^{-2} |S_2(R, N, \theta)|^2\end{aligned}\tag{10}$$

where A = overall normalization (fitting parameter)
 R = particle radius (fitting parameter)
 N = real index of refraction (fitting parameter)
 $k = 2\pi/\lambda$, λ = wavelength of illumination
 θ = scattering angle
 S_1 = Mie scattering amplitude for perpendicular component
 S_2 = Mie scattering amplitude for parallel component

The subsets of the data that were fit, along with the associated errors and resulting fits, are shown in Figures 43 through 48. The mismatch between the data and theoretical curve, as well as the numerical value of chi-square, indicates that the data are not fit by the Mie theory. This could be due to the fact that the samples are not perfect spheres. Examination of the particle photographs offers some corroboration of this hypothesis, with an internal flaw being seen in Particle 1 and noncircular images being measured for Particles 2 and 3. We shall, however, continue referring to these particles as spherical even though they are only approximately so.

The next attempt to obtain particle size data by fitting the differential scattering cross section was based on a simple diffraction model. If the particle is assumed to be a planar disc or ellipse blocking the beam radiation, then by Babinet's Principle³ the diffraction caused by the particle is the same as for a complementary aperture. We can then use the basic Airy diffraction formula for a circular or elliptical aperture⁴ as a starting point for our model. In addition to the diffraction effect, a smooth background that did not increase with scattering angle was added. The model was then given by

$$\frac{d\sigma}{d\Omega} \approx A \left(\frac{2J_1(x)}{x} \right)^2 + B \exp(-C\theta) \quad (11)$$

where A,B,C,D ≥ 0 are the fitting parameters

θ = scattering angle

$J_1(x)$ = Bessel function of the first kind of order 1

$$x = \frac{\pi D \sin \theta}{\lambda}$$

D = particle diameter (fitting parameter)

This model was fit independently to the full 1012 cross-section values in each of the channels for all six particles. Reasonable fits were achieved for the spherical particles, with chi-squares per degree of freedom ranging from 2.3 to 9.6, but not for the nonspheres, where the chi-squares were an order of magnitude larger. The best fitting curves for the spheres are shown in Figures 49 through 54 and the derived semi-axis dimensions tabulated in Table II. Note that the fitting results support the hypothesis that Particle 3 is in fact nearly spherical and that the elongated photographic image is due to particle motion. This is for two reasons: adequate fits were not achieved for known nonspherical particles and the ratio of the independently derived semi-axes is very close to unity. However, there is approximately a factor of two difference between the photographically- and model-determined semi-axes for all three particles. This difference could be due to either photographic image enlargement as a result of flare and poor resolution, or the model may give a biased result. Further theoretical work is necessary to understand the consequences of this diffraction model, which treats the scattering from a three-dimensional object as if it were for a two-dimensional one.

Table II
Particle Dimensions Derived From Fitting

<u>Particle</u>	<u>a_F</u> <u>(μm)</u>	<u>b_F</u> <u>(μm)</u>	<u>b_F/a_F</u>
1	3.9	4.2	1.08
2	3.2	3.4	1.06
3	3.1	3.3	1.06

In addition to model fitting, the data were analyzed by plotting some phenomenological quantities derived from the data as a function of particle size and visually searching for trends. The first quantities defined were the total observed cross sections σ_A and σ_B in each channel:

$$\sigma_A = \sum_{i=1}^{1011} \frac{d\sigma}{d\Omega_{Ai}} \sin \theta_i (\theta_{i+1} - \theta_i) \quad (12)$$

$$\sigma_B = \sum_{i=1}^{1011} \frac{d\sigma}{d\Omega_{Bi}} \sin \theta_i (\theta_{i+1} - \theta_i) \quad (13)$$

$$\sigma_T = \sigma_A + \sigma_B \quad (14)$$

The channel cross sections σ_A and σ_B are plotted as a function of the particle's equivalent radius in Figure 55 and the total cross section as a function of radius in Figure 56. Particles with an equivalent radius less than $9 \mu\text{m}$ are spherical and those with a larger radius nonspherical. Figure 55 shows that the channel cross sections are different for only two of the three nonspherical particles. Particle 5, which has the most extreme aspect ratio, has the largest difference in channel cross section. Particle 6, with the intermediate aspect ratio, has the second largest difference. For Particle 4, which has the aspect ratio closest to 1.0, the channel cross sections are indistinguishable. There is not a clear connection, however, between the total observed cross section and equivalent radius, as illustrated in Figure 56. In this plot, the largest cross section is for a particle in the center of the radius range and the smallest is for the second largest particle. To test whether the total cross section versus equivalent radius was obscuring a relationship between cross section and size because of averaging over two orthogonal channels, the individual channel cross section versus the photographically-determined ellipse semi-axis in that direction is plotted in Figures 57 and 58. Again, there is no clear trend between size and cross section.

Given the large number of measurements of scattering cross section versus angle, a statistical analysis of this data might be used to obtain information about the particle. We know, for example, that the scattering pattern for a sphere is a set of light and dark rings on a screen perpendicular to the incident beam. This suggests that if we were to correlate the differential cross sections in Channels A and B, then spherical particles would exhibit a high degree of correlation. The concept of correlation can be visualized through the device of a scatter plot. In this plot a point (x_i, y_i) in a Cartesian coordinate system is created from the differential scattering cross section in each channel at a particular scattering angle θ_i , i.e.,

$$x_i = \frac{d\sigma}{d\Omega_A} (\theta_i)$$

$$y_i = \frac{d\sigma}{d\Omega_B} (\theta_i) \quad (15)$$

The points (x_i, y_i) are then plotted for all θ_i in figures 59 through 76, with one plot for each data set. If the points are highly correlated they will cluster along a line of positive slope. If they are anti-correlated, they will cluster along a line with negative slope. Uncorrelated points will cluster along a line parallel to one of the axes or will be randomly distributed throughout the space. Visually, the plots for the spherical particles show a high degree of correlation, as expected, whereas the plots for nonspheres are less correlated. The correlation is quantified in a statistical measure known as the correlation coefficient ρ , defined as

$$\rho = \frac{\langle (x - \bar{x})(y - \bar{y}) \rangle}{\langle (x - \bar{x})^2 \rangle \langle (y - \bar{y})^2 \rangle}^{-1/2} \quad (16)$$

which has the property

$$-1 \leq \rho \leq 1. \quad (17)$$

For the discrete case, such as our data, we have

$$\begin{aligned} \langle (x - \bar{x})^2 \rangle &= \frac{1}{N} \left[\sum_{i=1}^N x_i^2 - \frac{1}{N} \left(\sum_{i=1}^N x_i \right)^2 \right] \\ \langle (y - \bar{y})^2 \rangle &= \frac{1}{N} \left[\sum_{i=1}^N y_i^2 - \frac{1}{N} \left(\sum_{i=1}^N y_i \right)^2 \right] \\ \langle (x - \bar{x})(y - \bar{y}) \rangle &= \frac{1}{N} \left[\sum_{i=1}^N x_i y_i - \frac{1}{N} \left(\sum_{i=1}^N x_i \right) \left(\sum_{i=1}^N y_i \right) \right] \end{aligned} \quad (18)$$

Figure 77 shows the correlation coefficient as a function of the particle's equivalent radius. The correlation is near its upper limit for the spherical particles and is significantly less for the nonspherical particles. Therefore, the correlation coefficient of the differential scattering cross sections appears to be an indicator of the spherical or nonspherical shape of the particle.

VI. SUMMARY AND CONCLUSIONS

Results from the work reported here can be divided into two classes: experimental measurements and analysis of those measurements. From the differential scattering cross-section data, it appears that reproducible, high-resolution measurements can be made with the apparatus we have constructed. With relatively simple optical modification, this device can measure the differential cross sections from -30 to $+30$ deg in the two orthogonal directions. The use of a computer in the system to store the data means that relatively large, statistically significant sample runs can be contemplated. The microscope system for determining particle size and orientation should be improved to obtain better measurements of these quantities to be used in analysis, however.

Much more work remains to be done in the area of interpreting the experimental results. The cross sections plotted in Figures 7 through 42 exhibit a wealth of regular structure. However, only the data from nearly spherical particles could be fit to obtain a size estimate, and even in this case the diffraction model results do not yet yield an absolute size. The cross sections integrated over our observation angles could not be clearly related to particle size. The only reliable interpretative tool we found in this study was the correlation coefficient between the differential scattering cross sections in the two channels that separated spherical and nonspherical particles. This quantity contained no information, however, on particle size.

In conclusion, we have measured the differential scattering cross section of individual aerosol particles in two orthogonal directions. Although these data show visible differences as a function of particle shape and size, no reliable computational method was found to determine particle size. Further theoretical work is necessary to interpret the scattering data to obtain size information.

REFERENCES

1. E. J. Davis and A. K. Ray, *J. Colloid and Interface Sc.*, 75, 566 (1980).
2. J. V. Dave, IBM Palo Alto Scientific Center Document 320-3237 (1968).
3. M. Born and E. Wolf, Principles of Optics, Sixth Ed., 381 (1980).
4. Ibid., pp. 395-399.

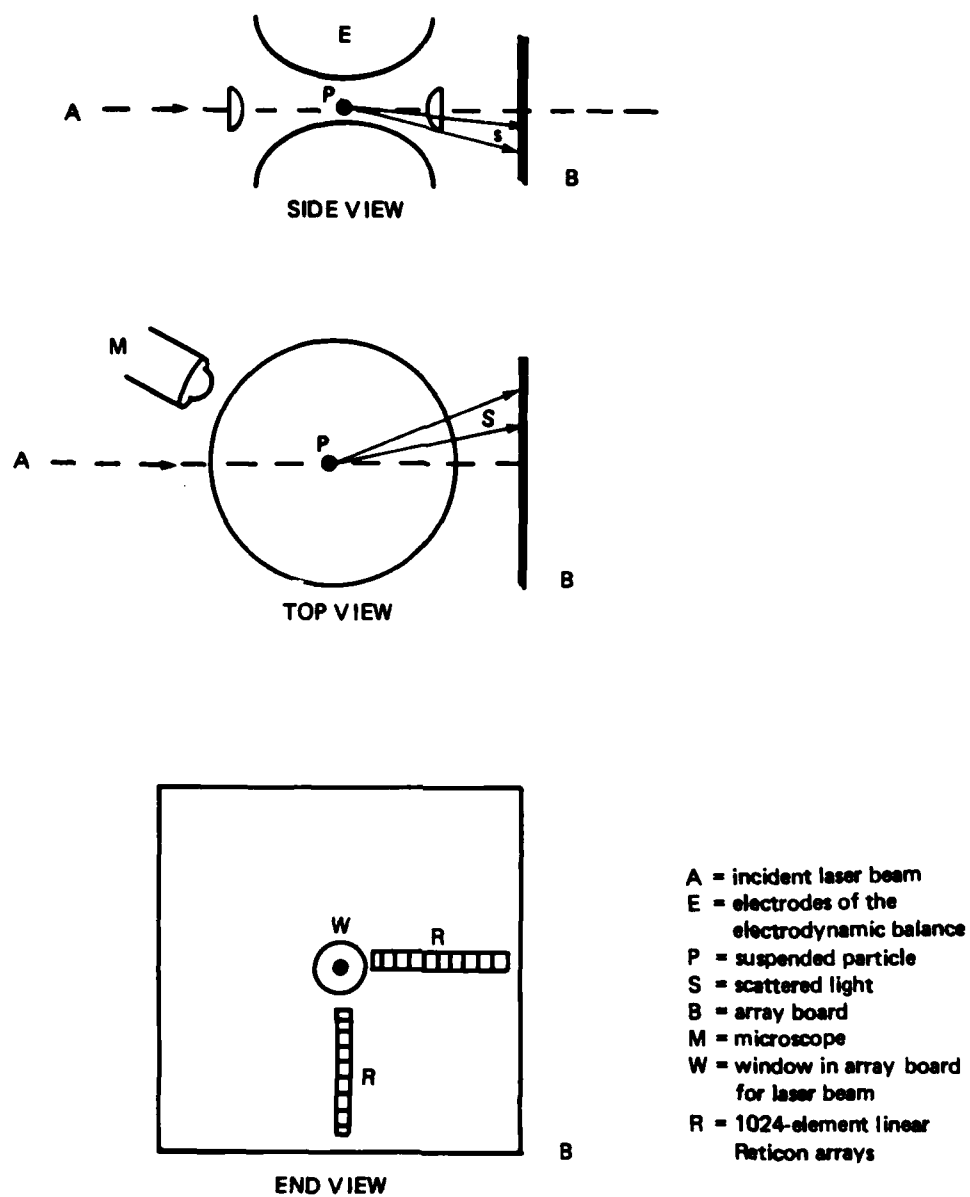


Figure 1. Schematic Diagram of System

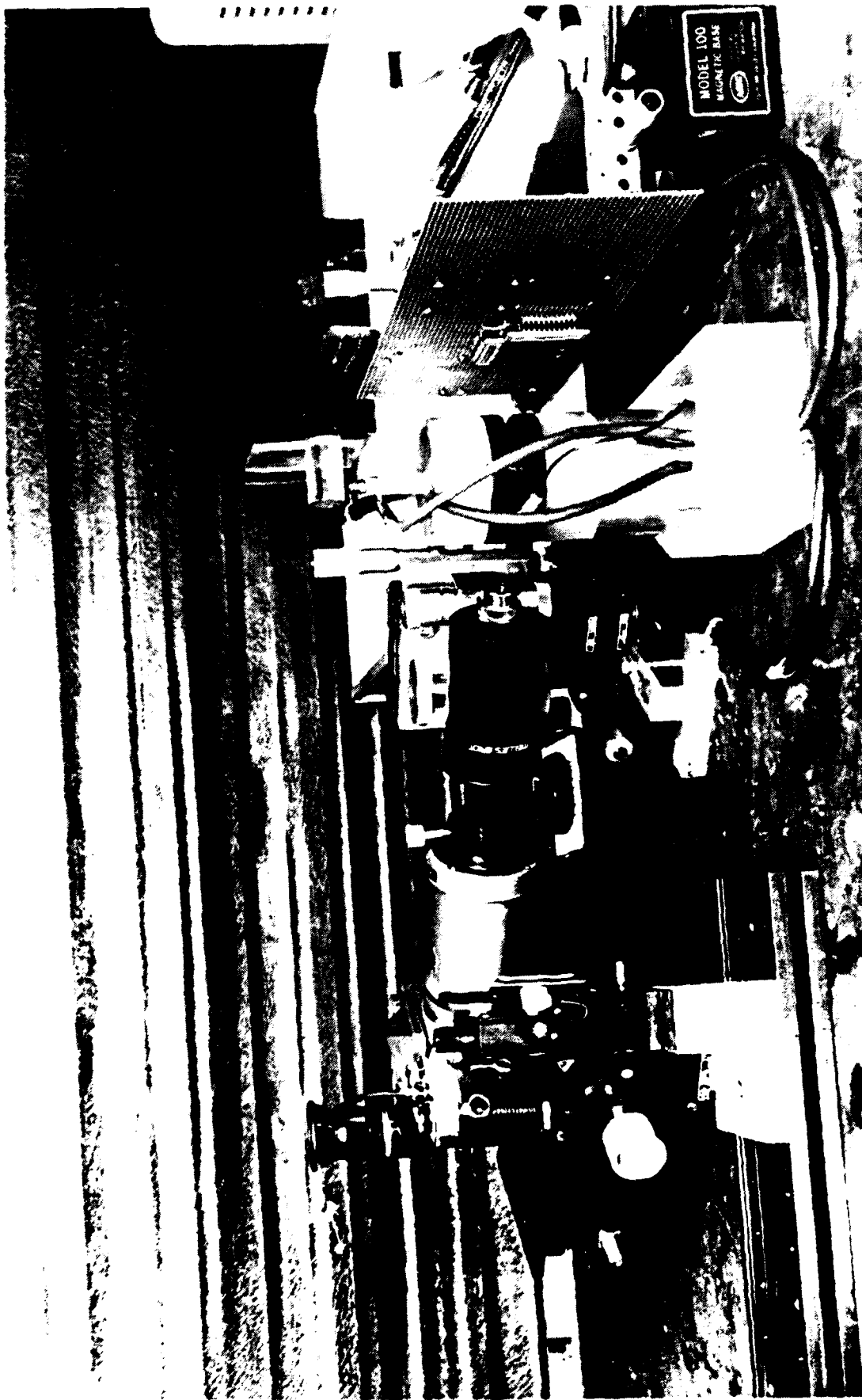
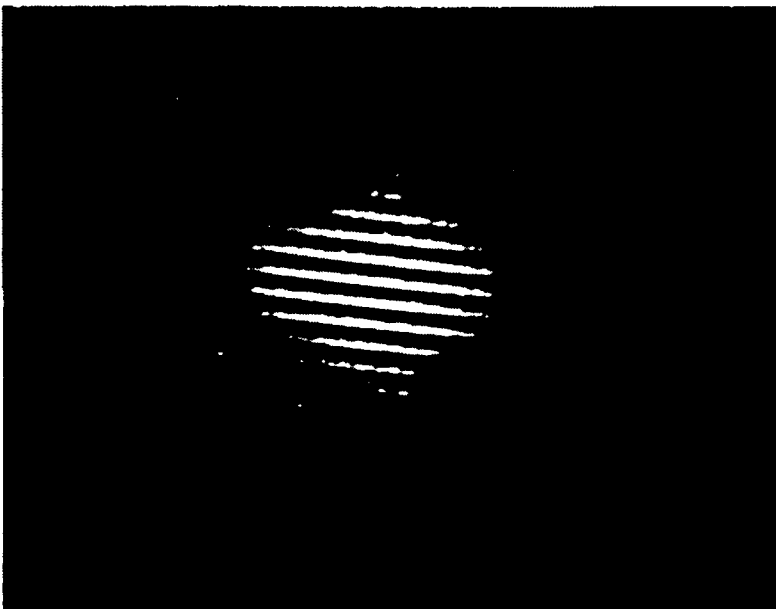


Figure 2. Photograph of System

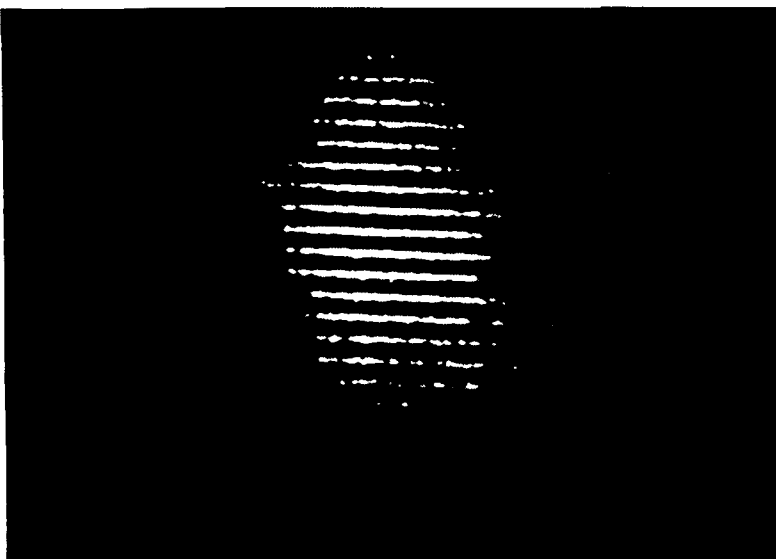
Particles in Electrodynamic Balance
(125X magnification of a 35mm transparency)



Particle 1



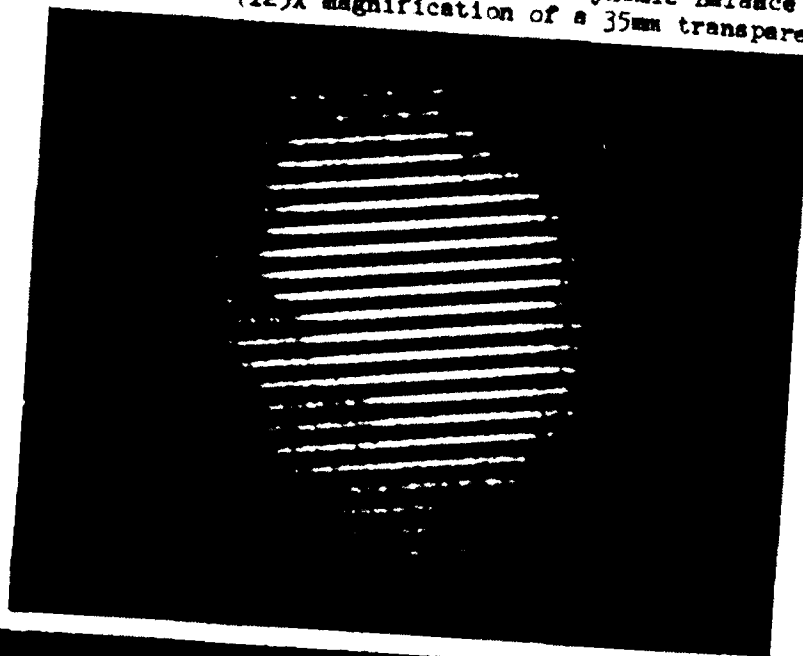
Particle 2



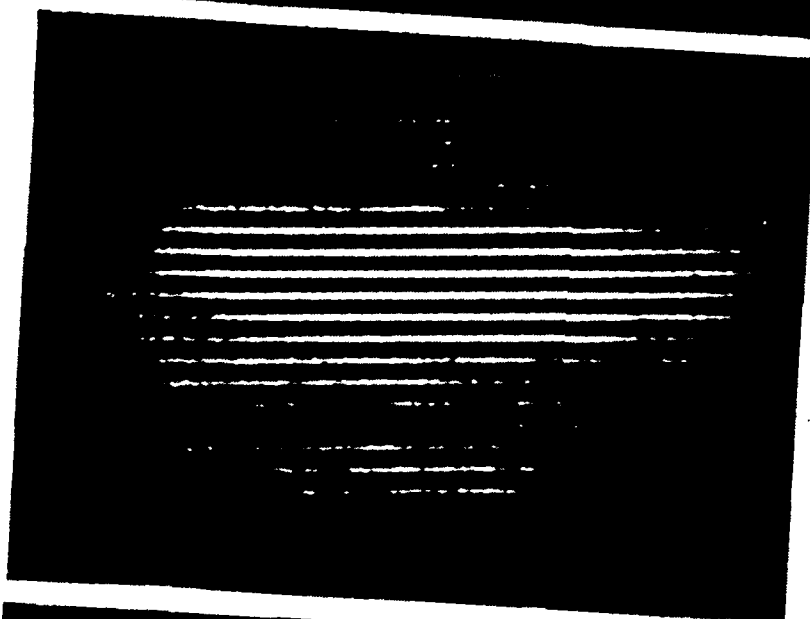
Particle 3

Figure 3. Photograph of
Particles 1, 2, and 3
in Electrodynamic Balance

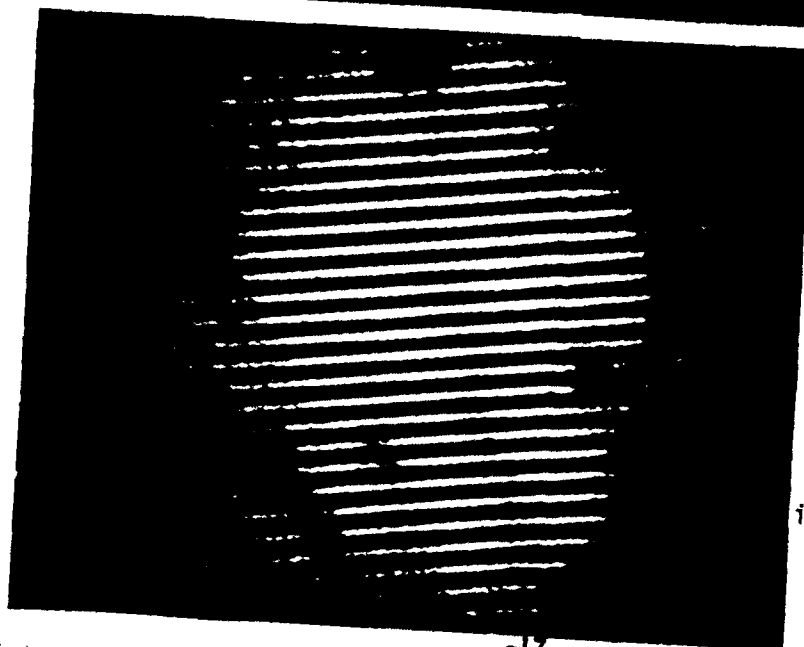
Particles in Electrodynemic Balance
(125X magnification of a 35mm transparency)



Particle 4



Particle 5



Particle 6

Figure 4. Photograph of
Particles 4, 5, and 6
in Electrodynemic Balance

Particle Information Services Glass Spheres

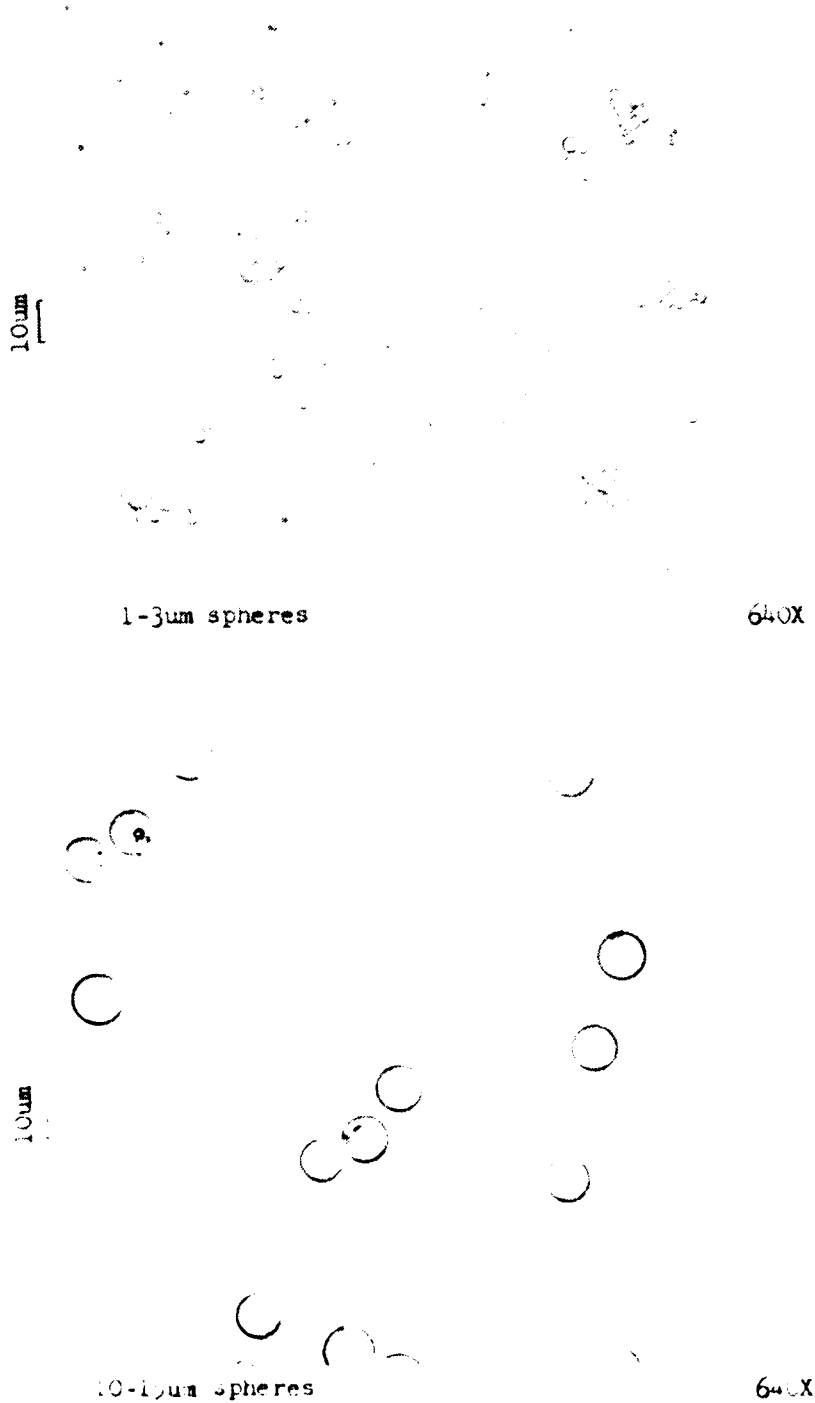


Figure 5. Photomicrographs of Particle Samples

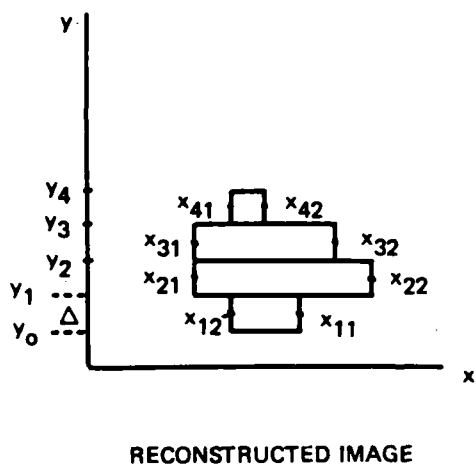
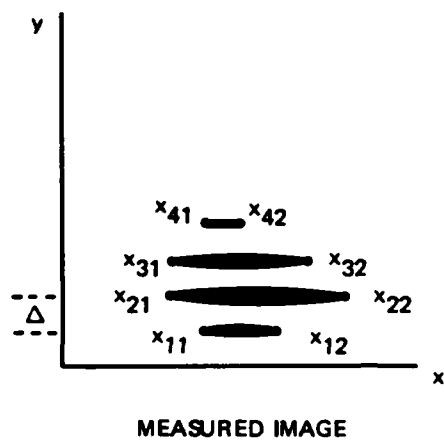


Figure 6. Image Geometry

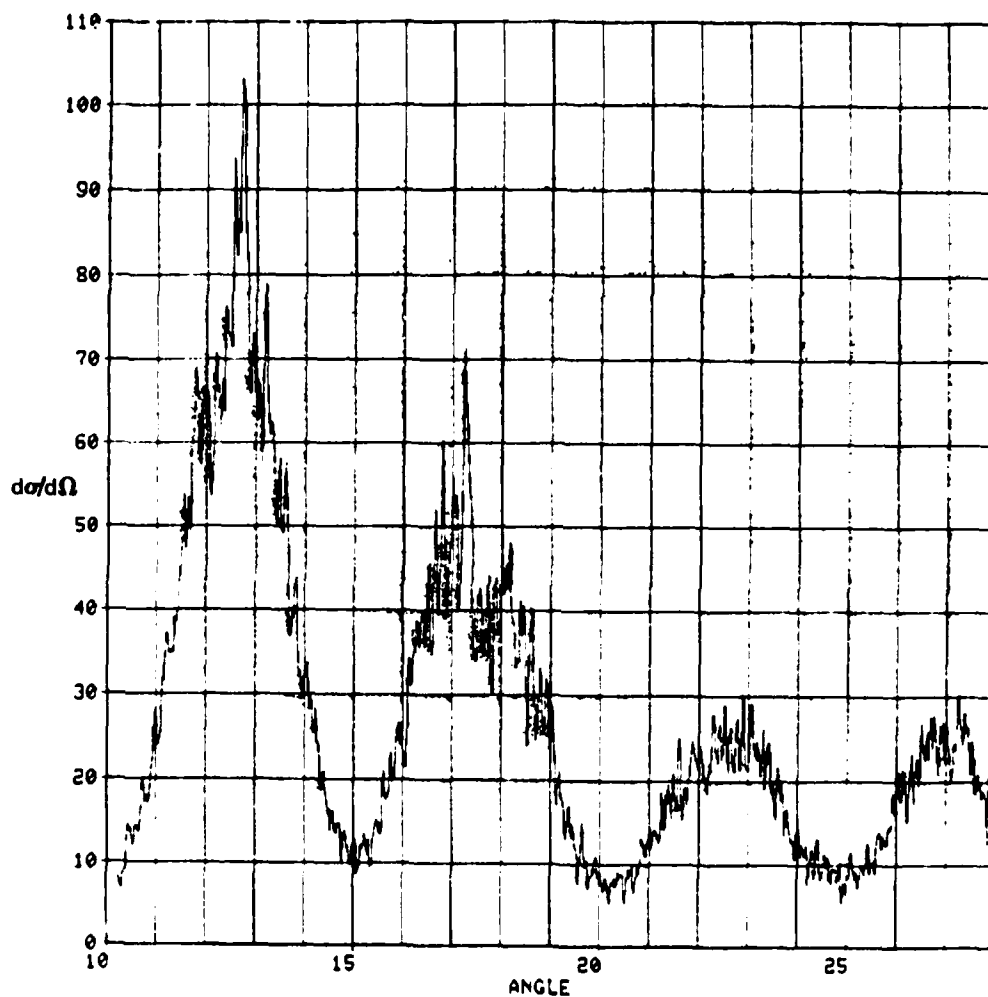


Figure 7. Differential Scattering Cross Section, Channel A, Particle 1, Sample 1

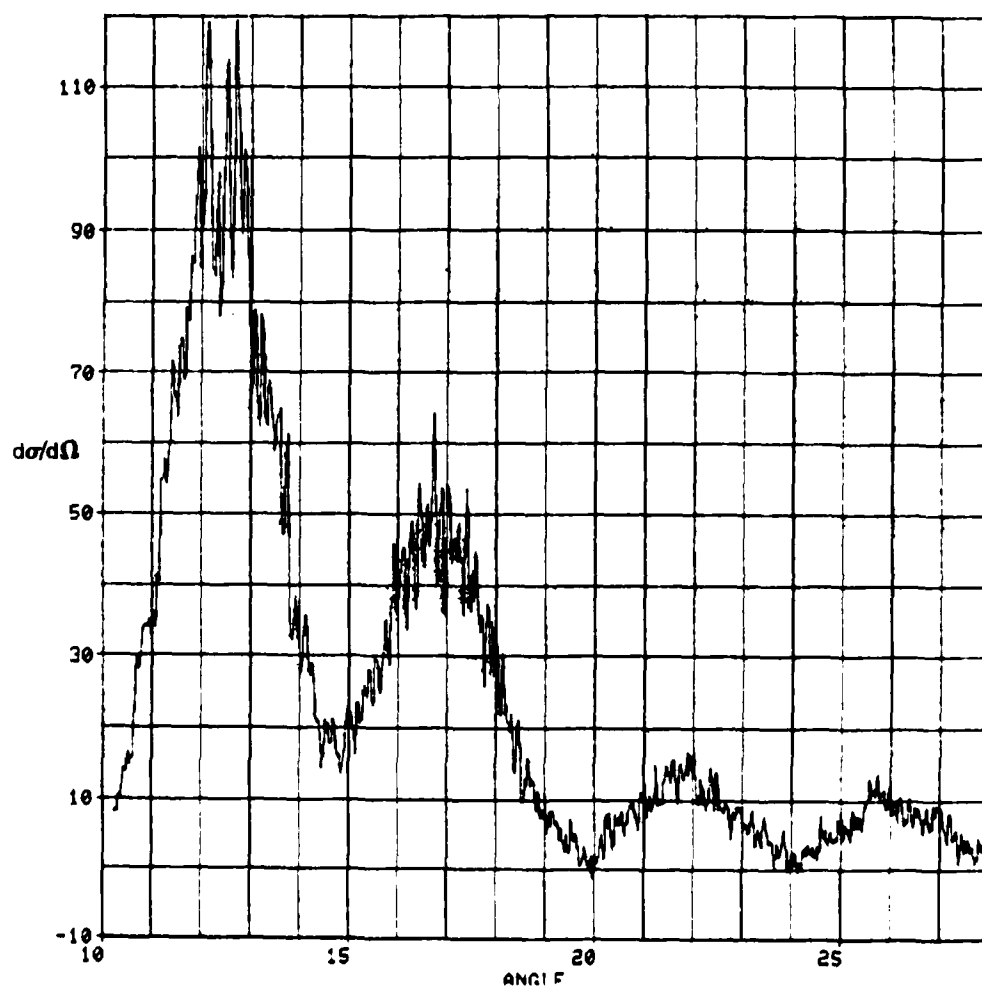


Figure 8. Differential Scattering Cross Section, Channel B,
Particle 1, Sample 1

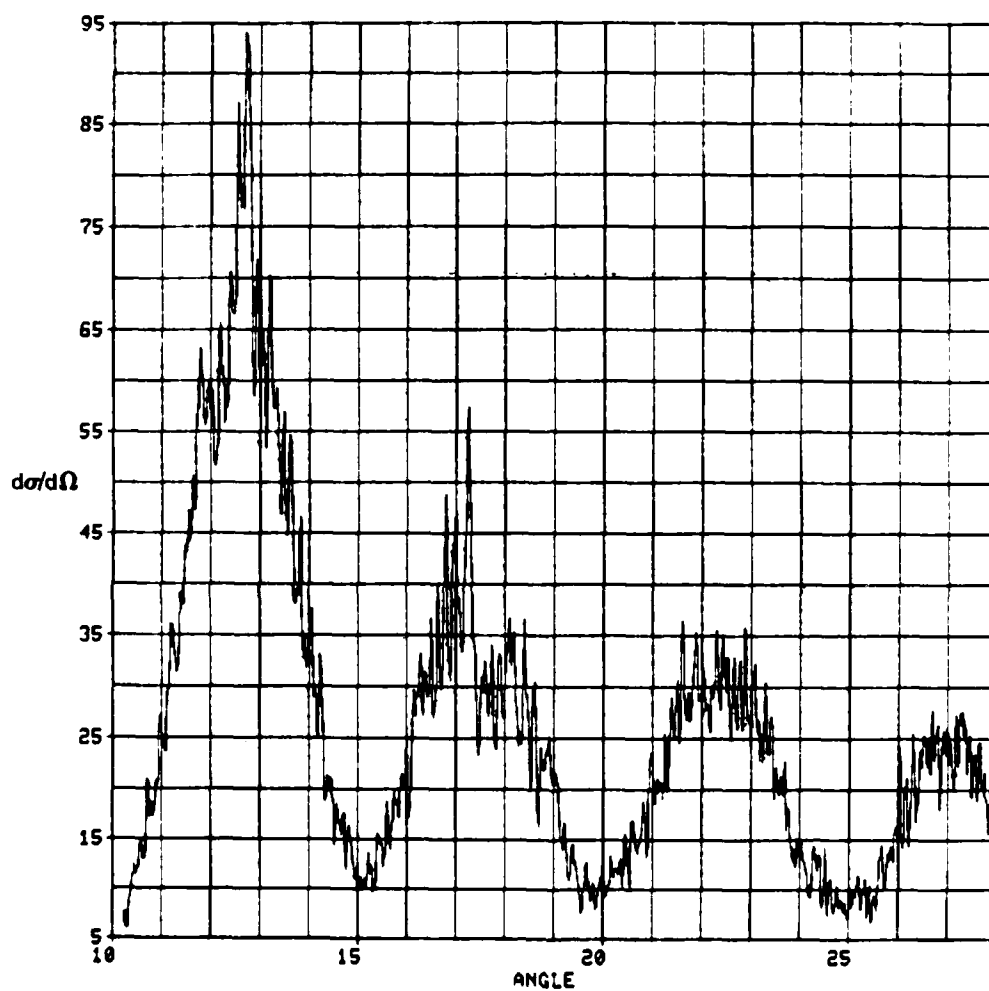


Figure 9. Differential Scattering Cross Section, Channel A,
Particle 1, Sample 2

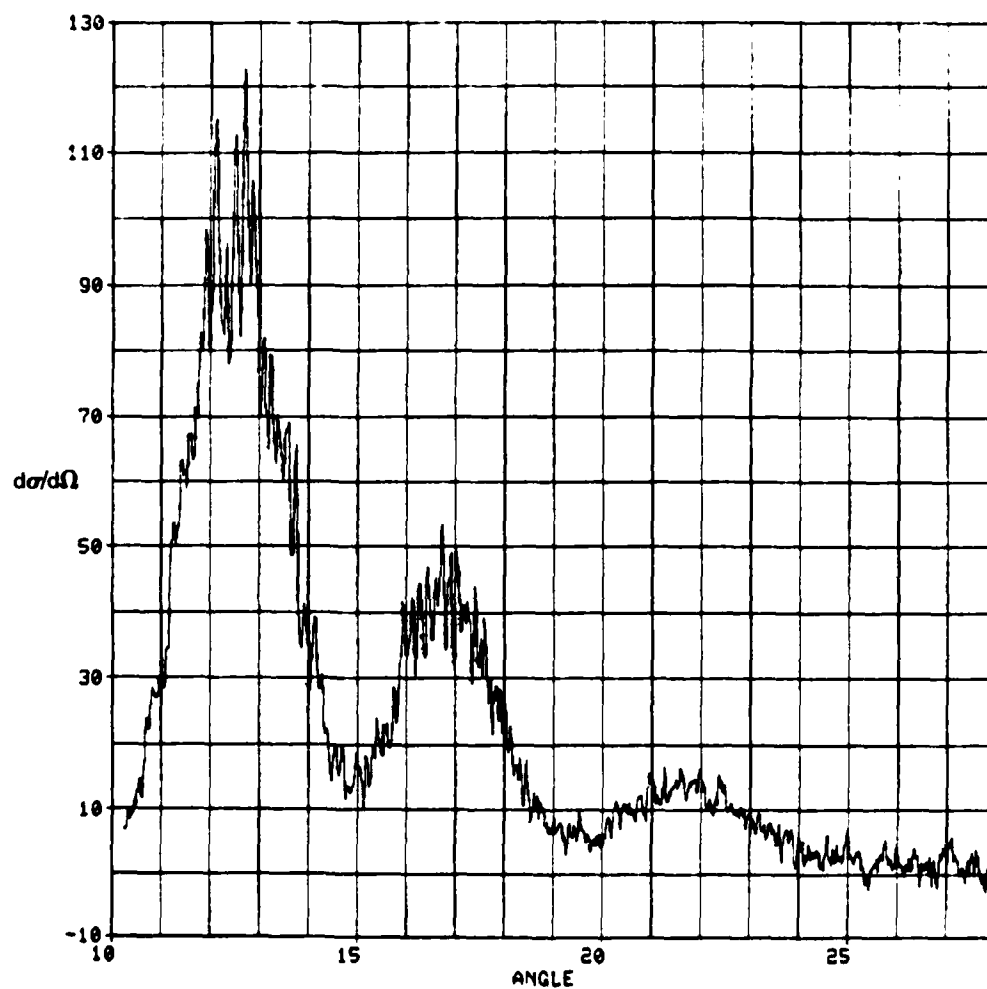


Figure 10. Differential Scattering Cross Section, Channel B,
Particle 1, Sample 2

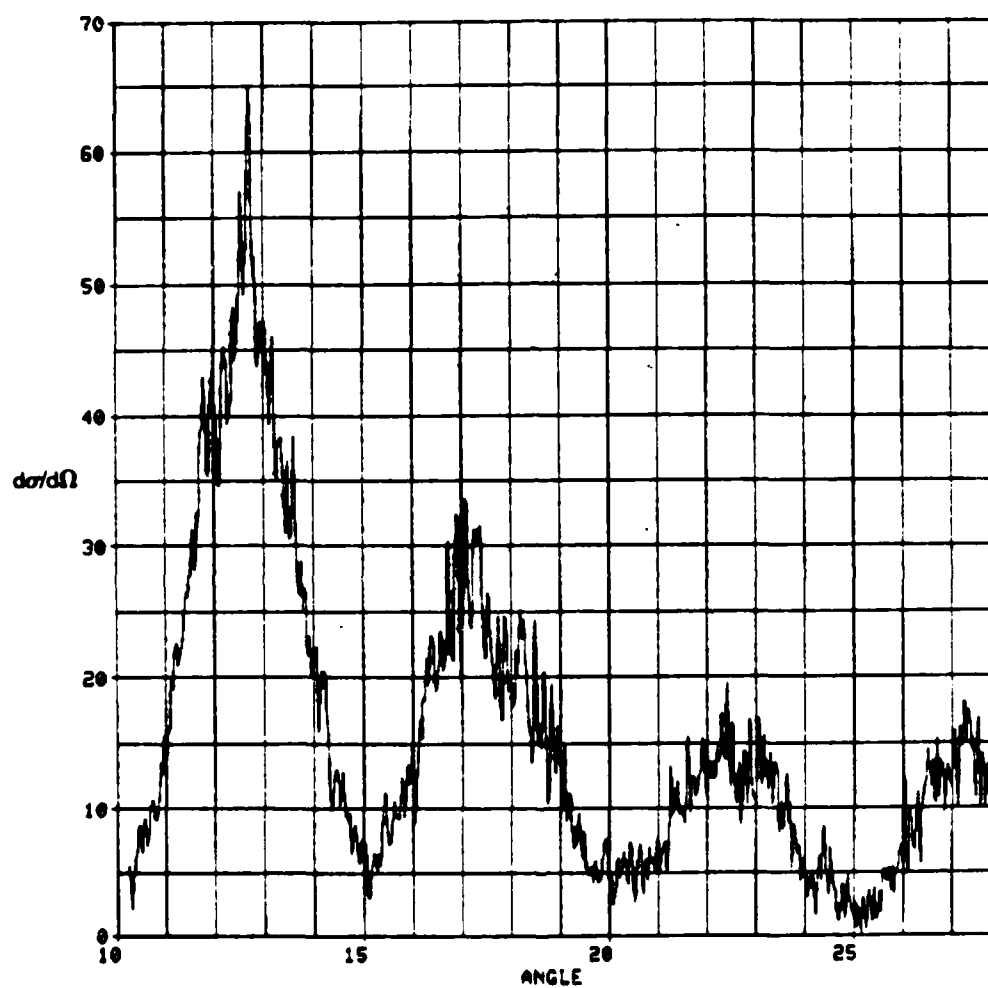


Figure 11. Differential Scattering Cross Section, Channel A,
Particle 1, Sample 3

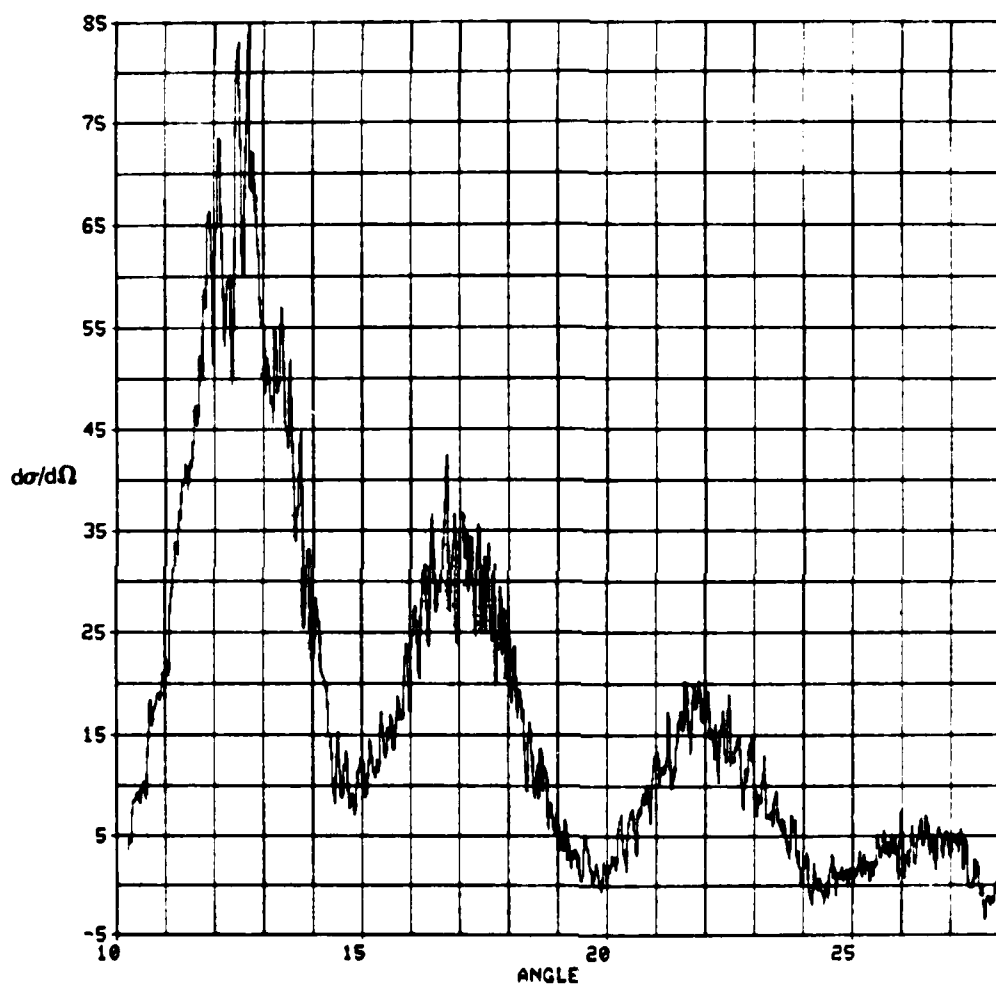


Figure 12. Differential Scattering Cross Section, Channel B,
Particle 1, Sample 3

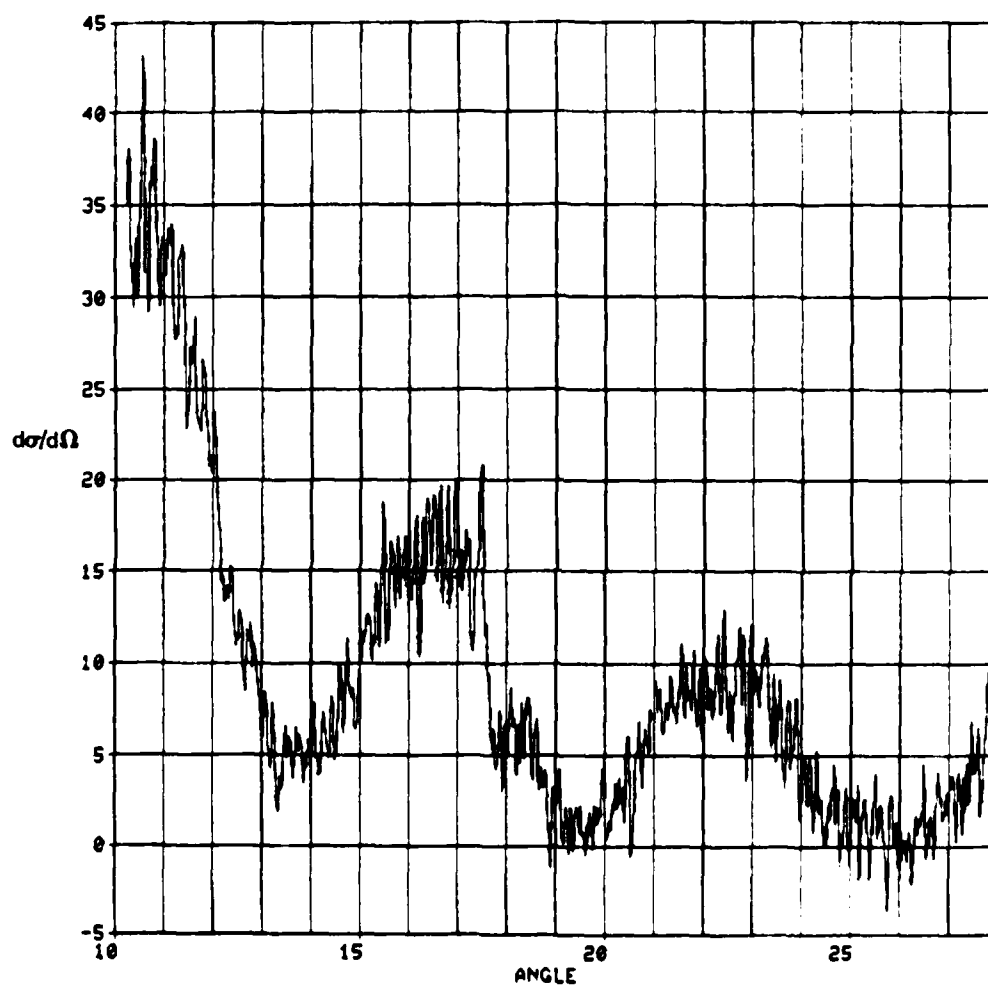


Figure 13. Differential Scattering Cross Section, Channel A,
Particle 2, Sample 1

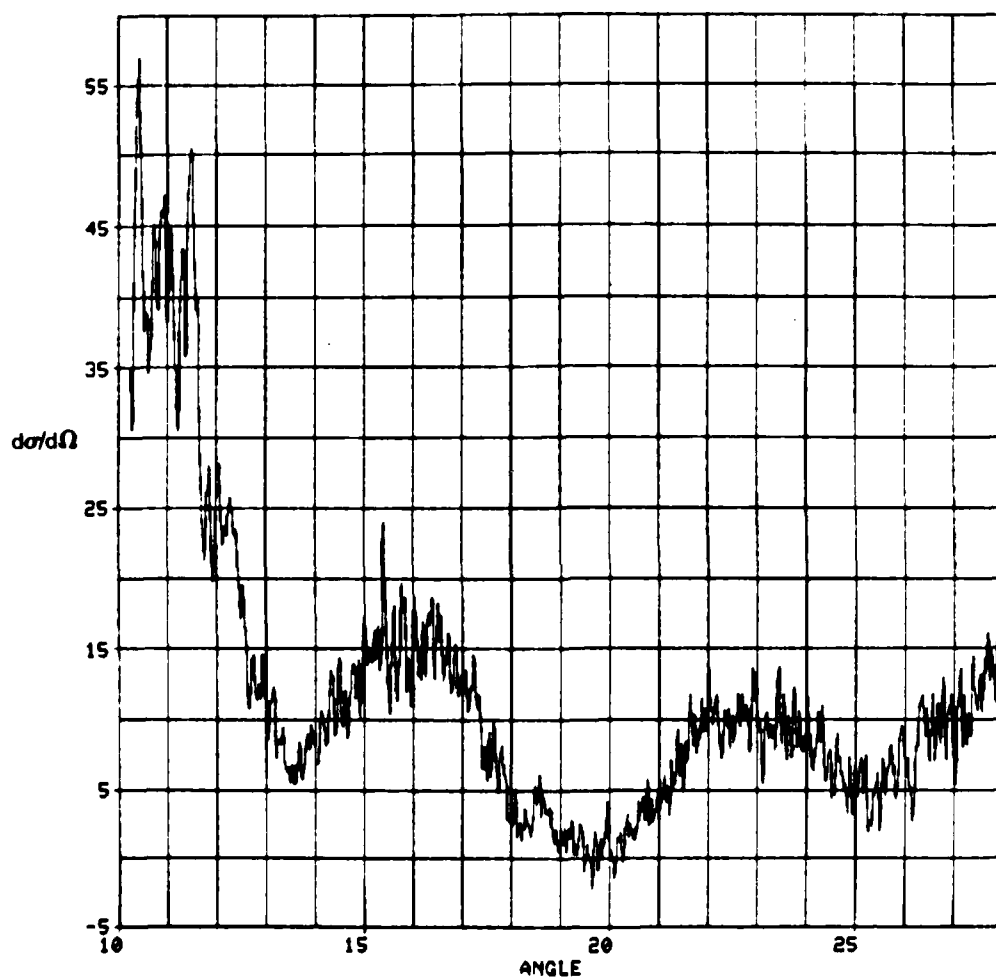


Figure 14. Differential Scattering Cross Section, Channel B,
Particle 2, Sample 1

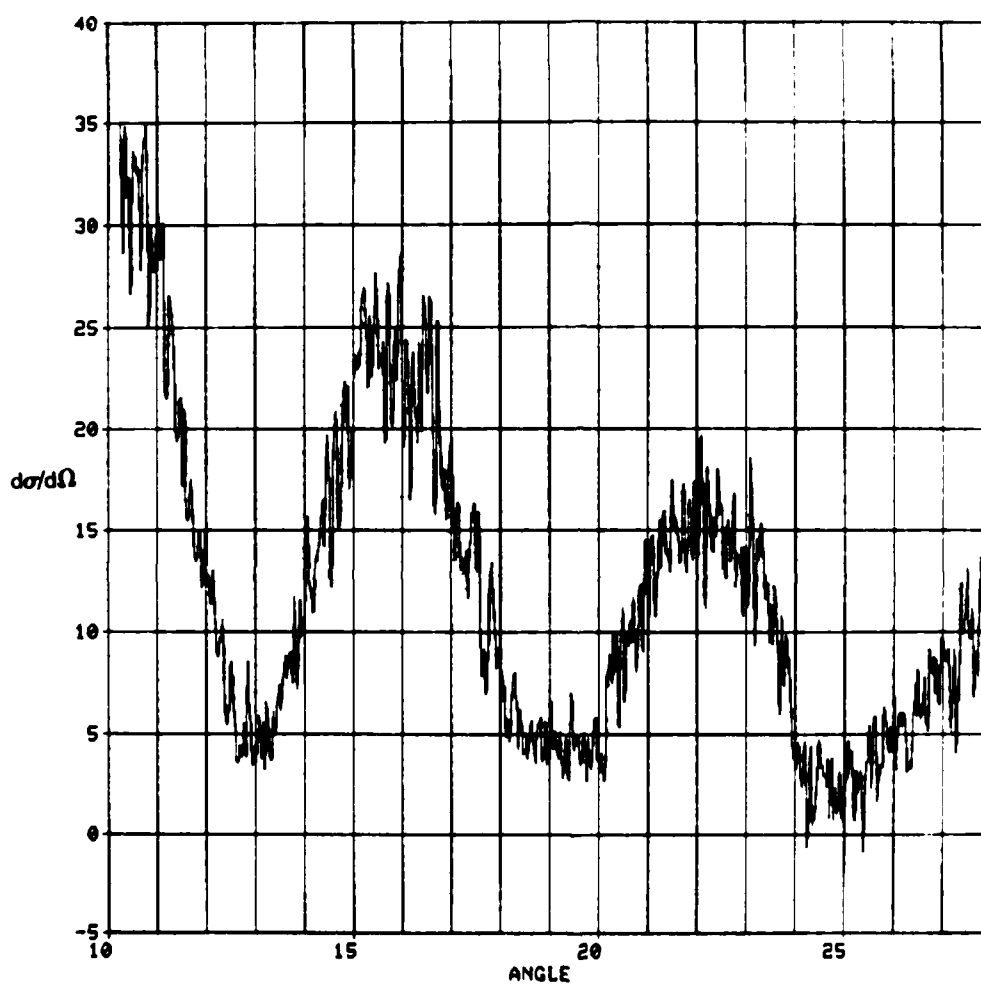


Figure 15. Differential Scattering Cross Section, Channel A, Particle 2, Sample 2

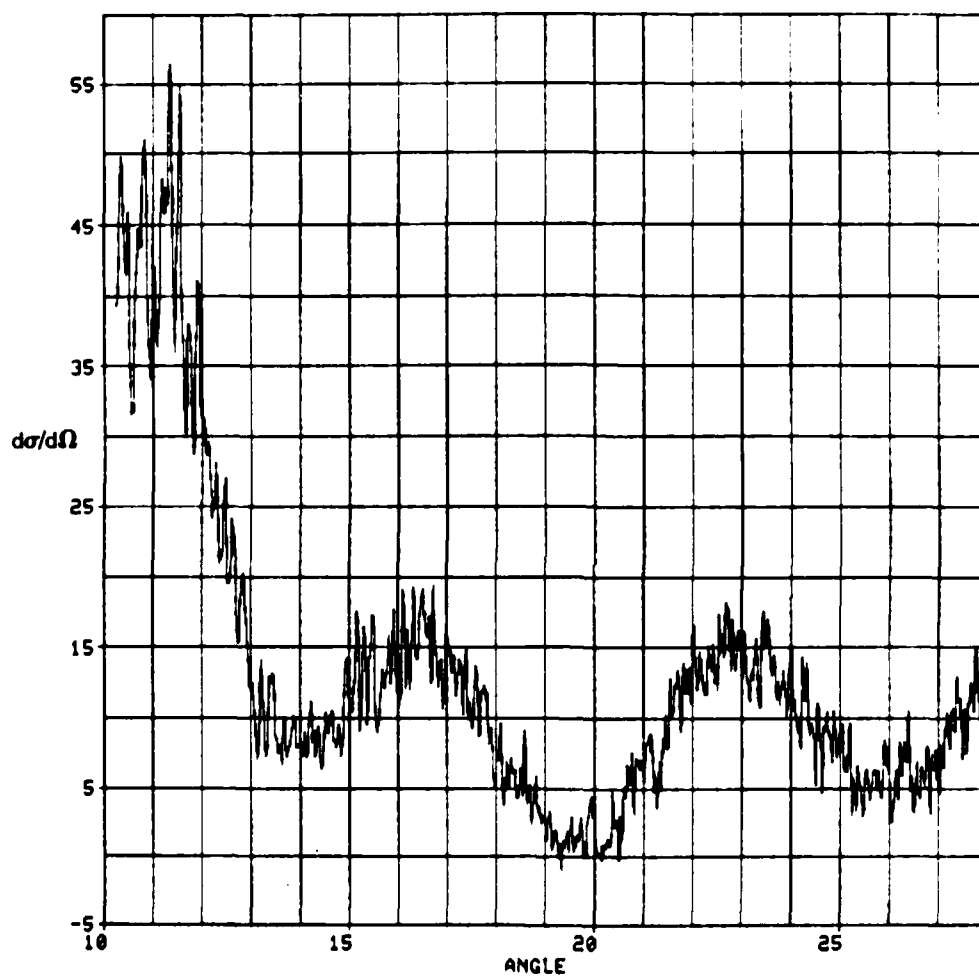


Figure 16. Differential Scattering Cross Section, Channel B,
Particle 2, Sample 2

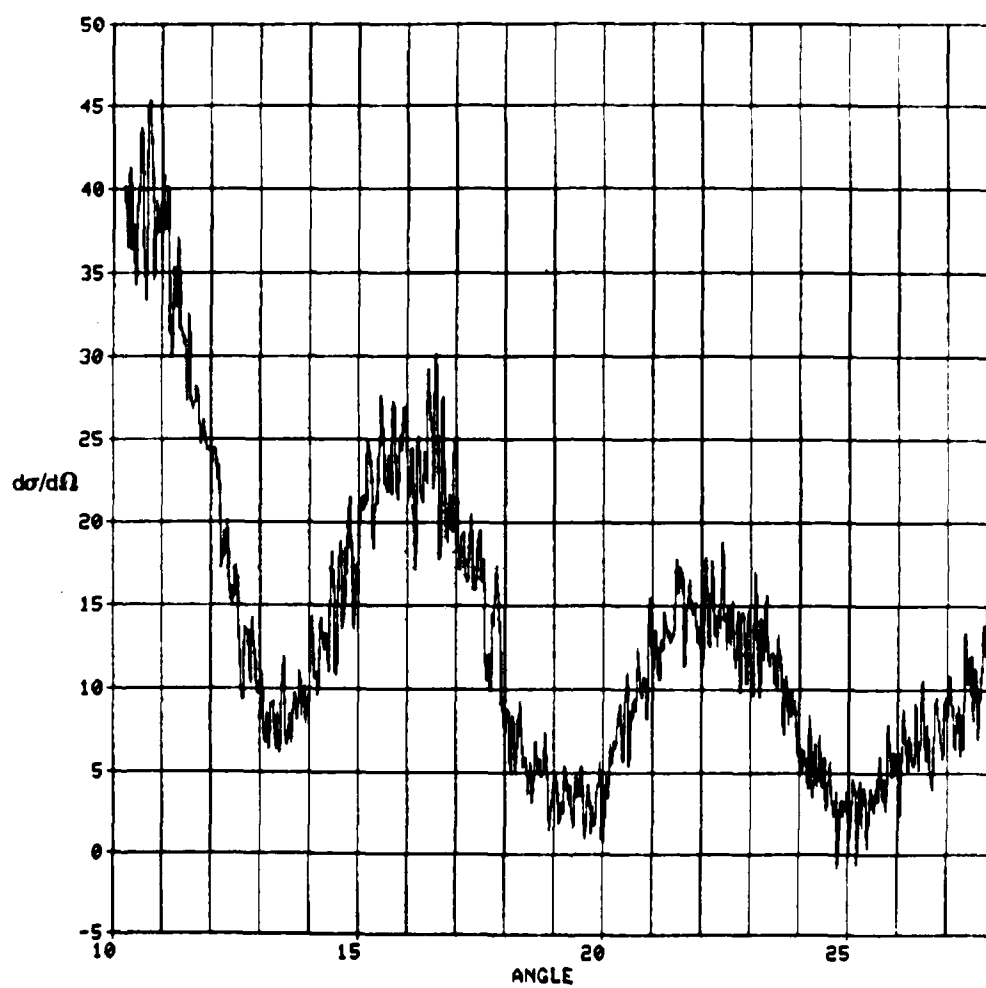


Figure 17. Differential Scattering Cross Section, Channel A, Particle 2, Sample 3

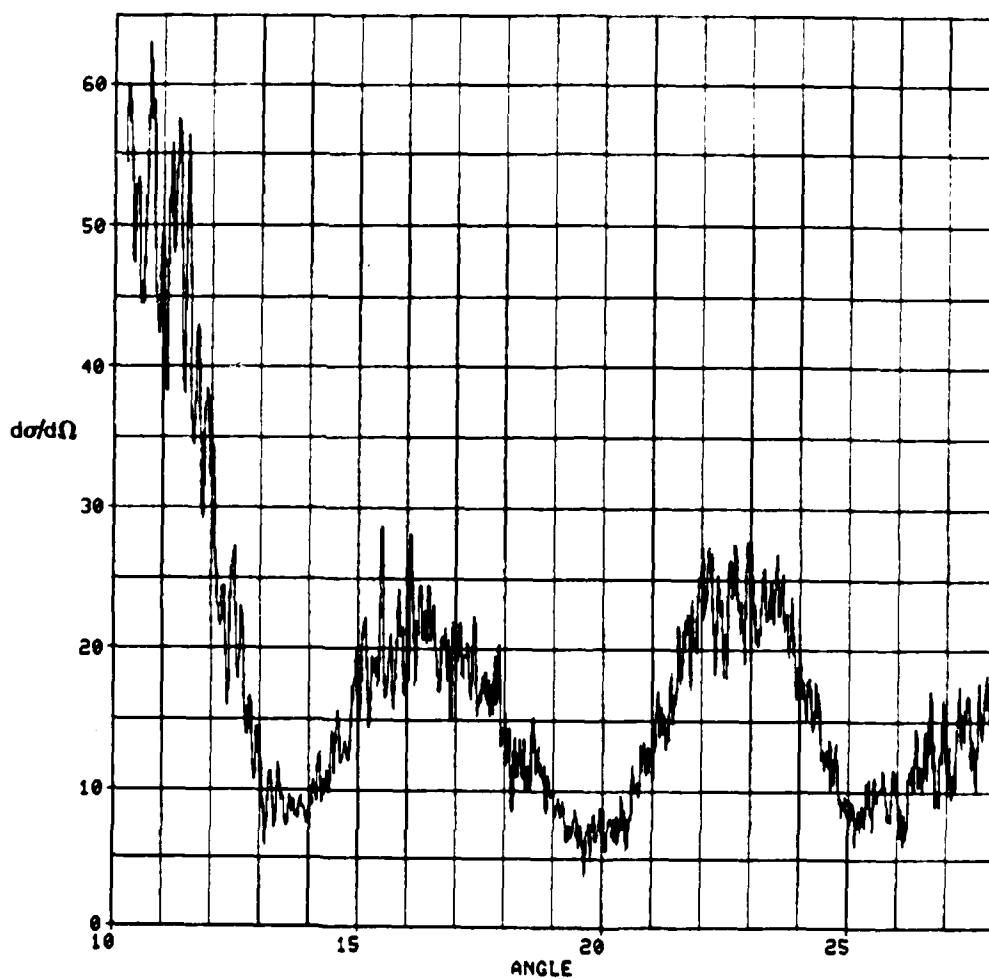


Figure 18. Differential Scattering Cross Section, Channel B,
Particle 2, Sample 3

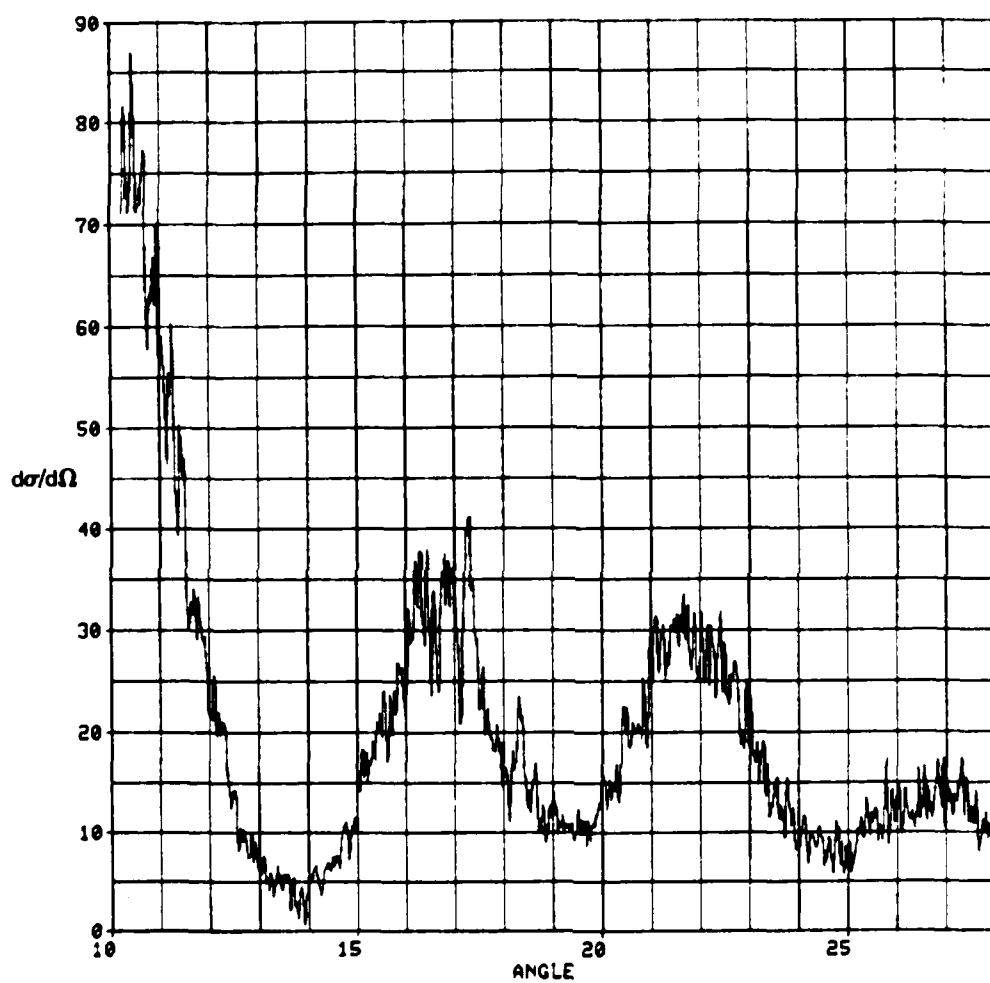


Figure 19. Differential Scattering Cross Section, Channel A, Particle 3, Sample 1

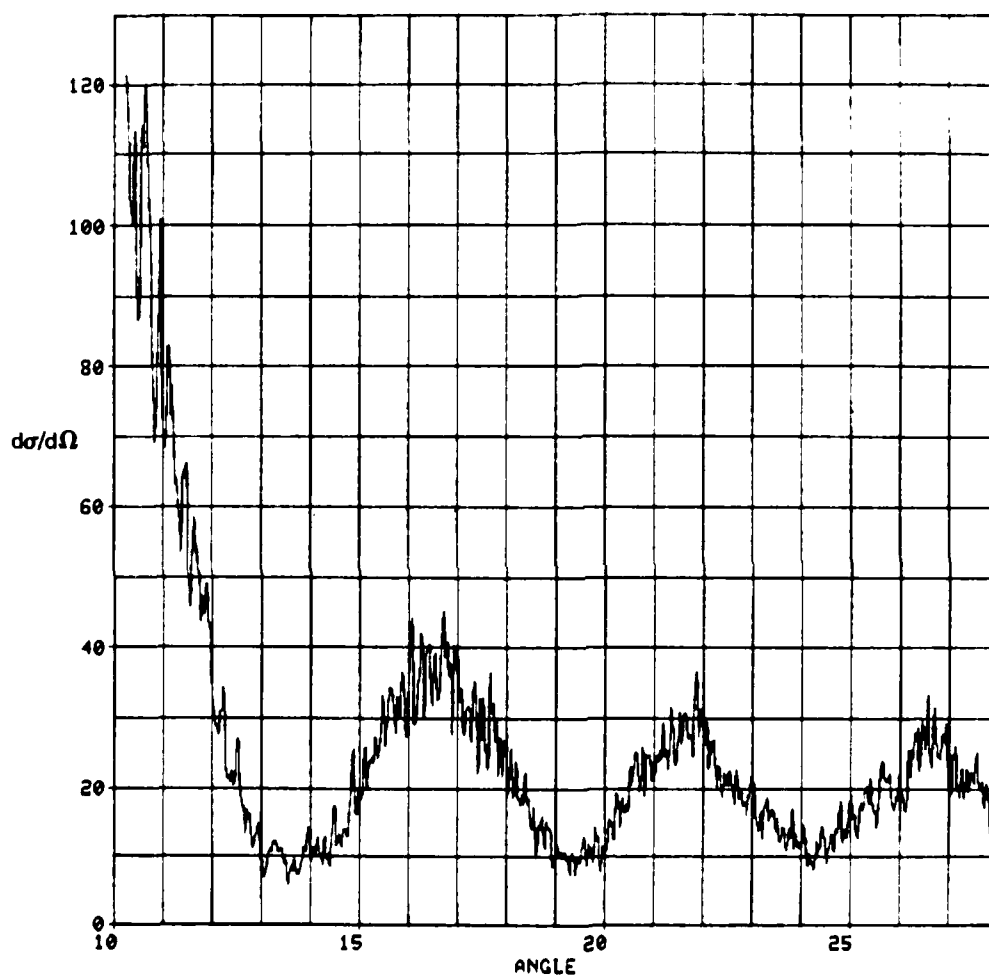


Figure 20. Differential Scattering Cross Section, Channel B, Particle 3, Sample 1

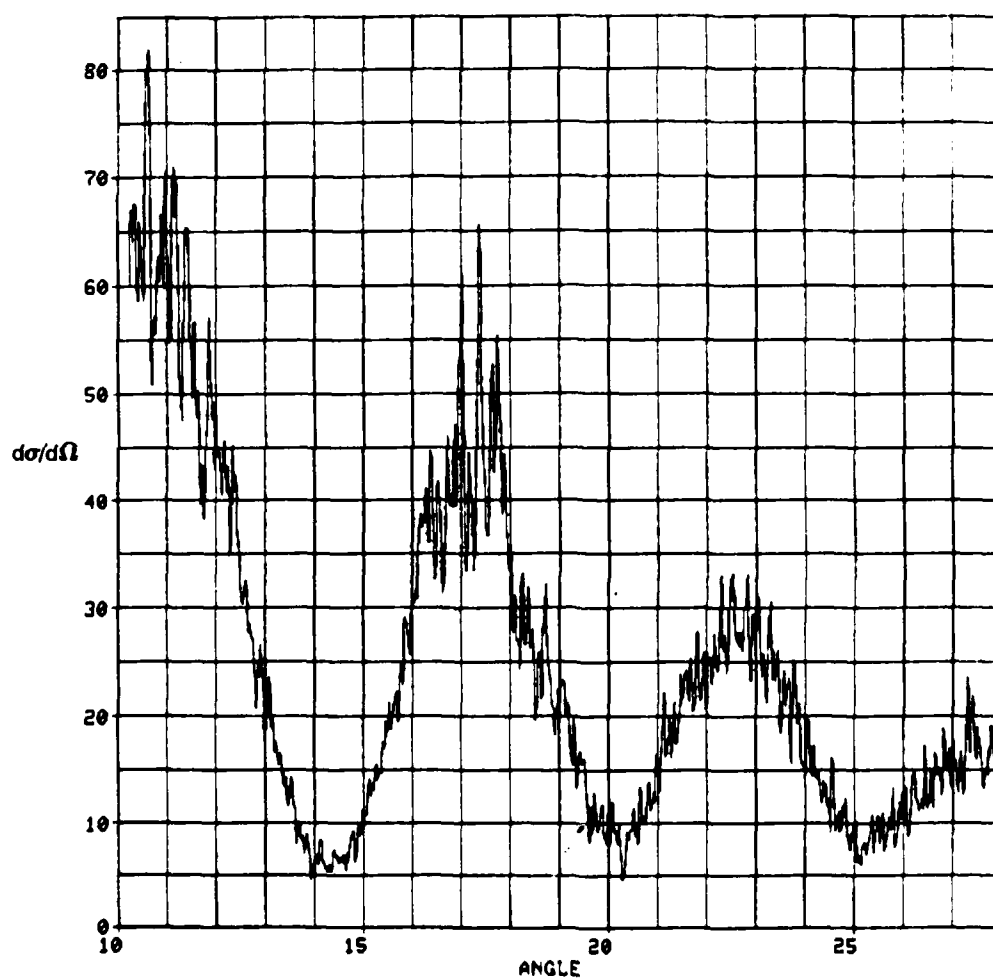


Figure 21. Differential Scattering Cross Section, Channel A, Particle 3, Sample 2

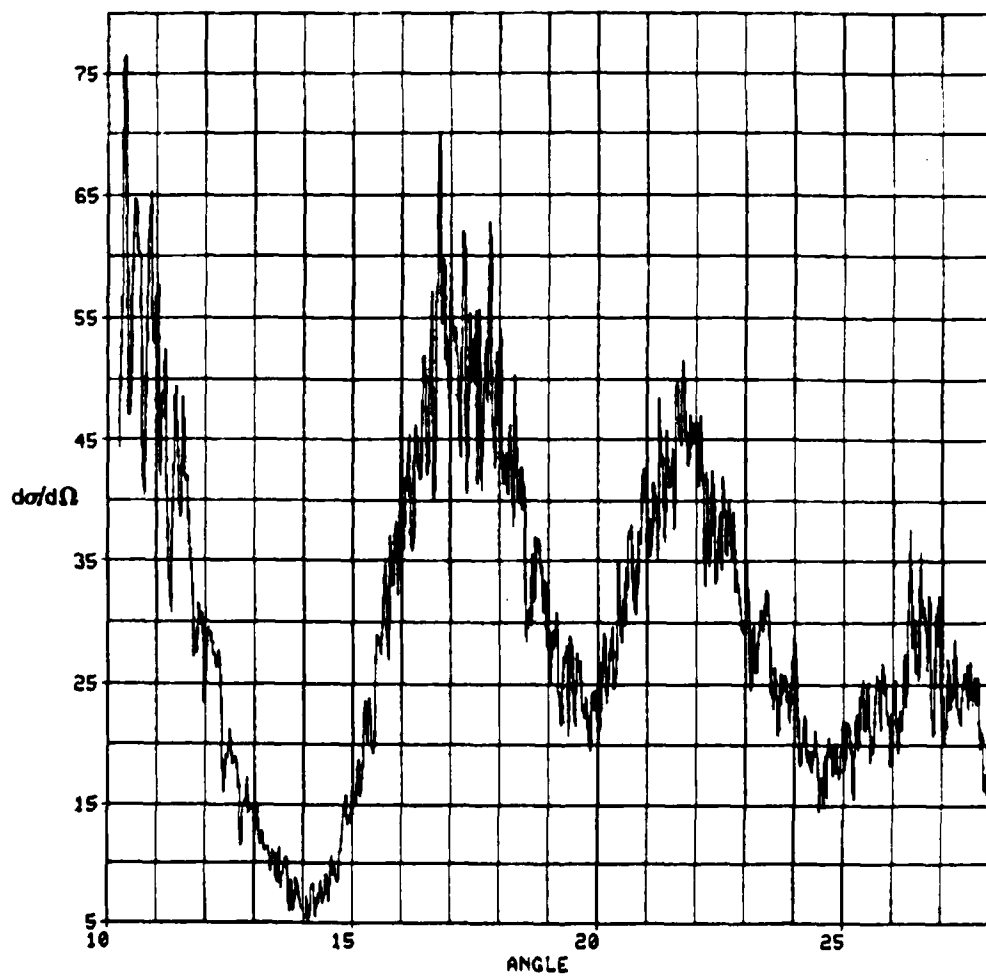


Figure 22. Differential Scattering Cross Section, Channel B,
Particle 3, Sample 2

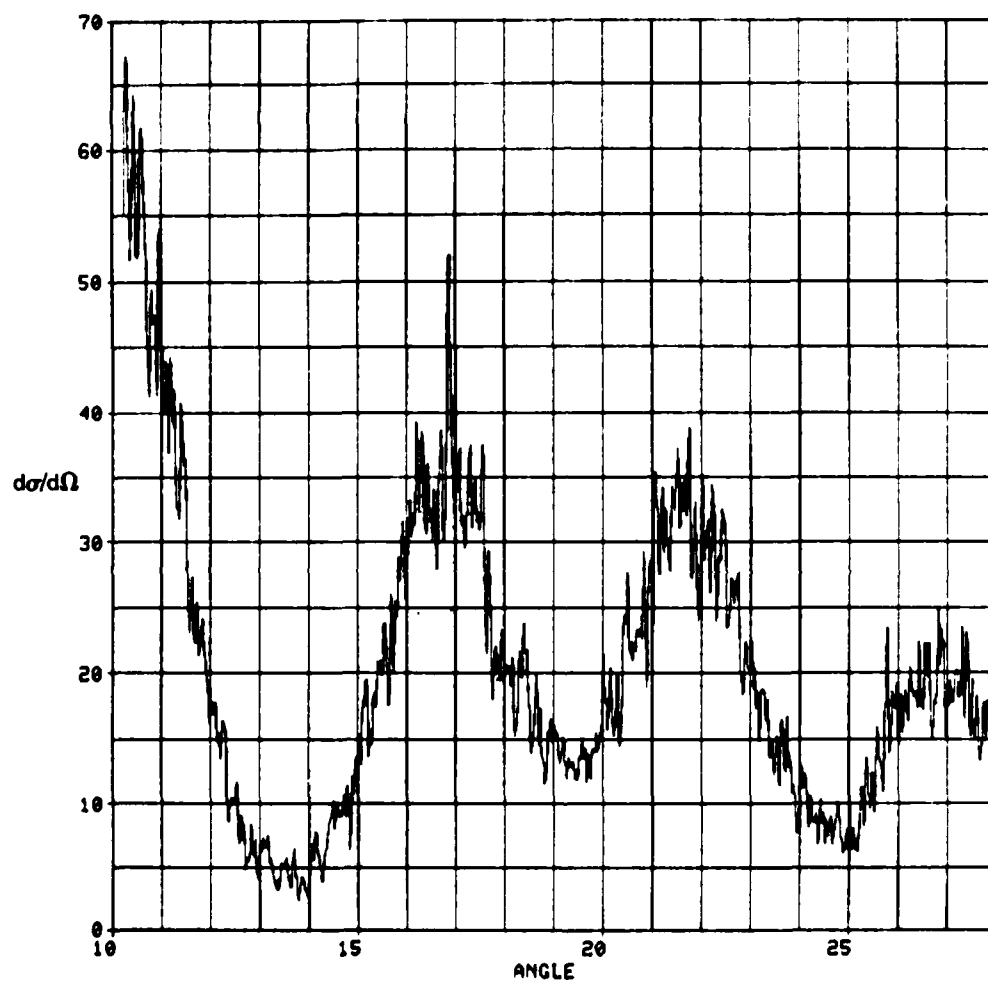


Figure 23. Differential Scattering Cross Section, Channel A,
Particle 3, Sample 3

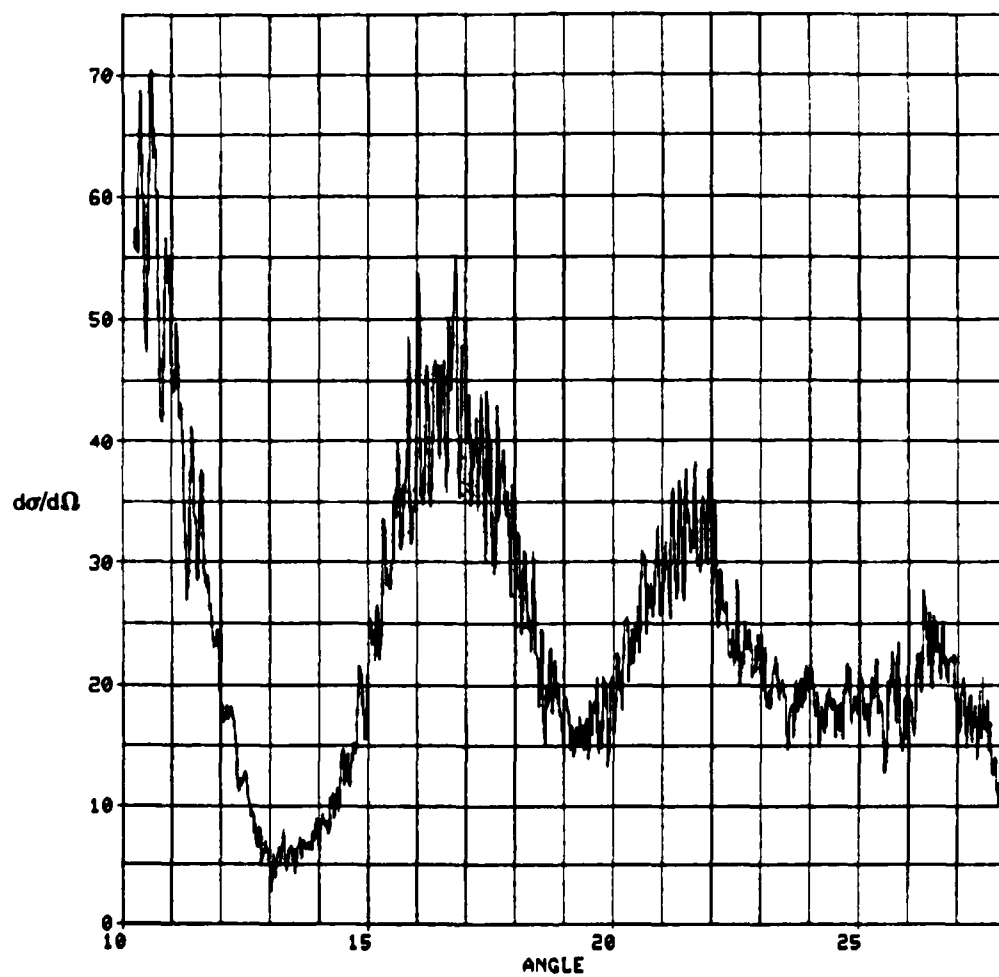


Figure 24. Differential Scattering Cross Section, Channel B,
Particle 3, Sample 3

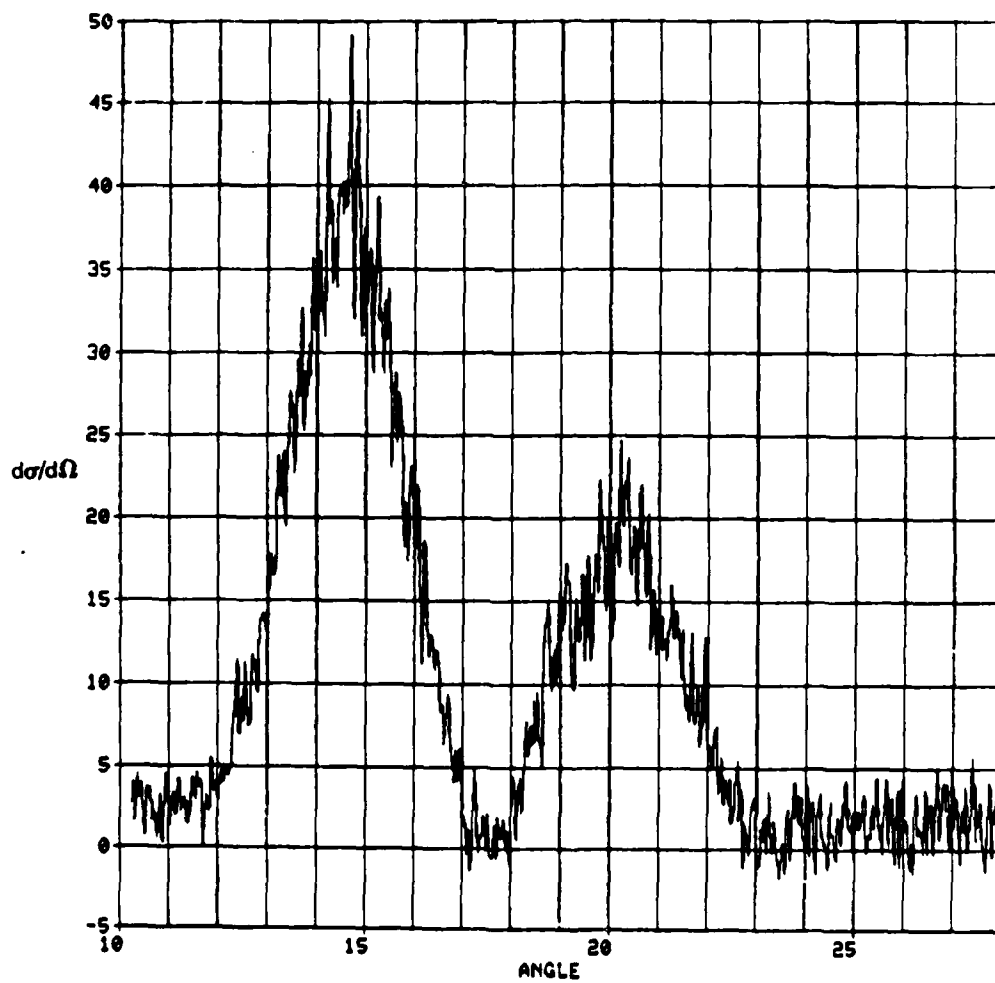


Figure 25. Differential Scattering Cross Section, Channel A, Particle 4, Sample 1

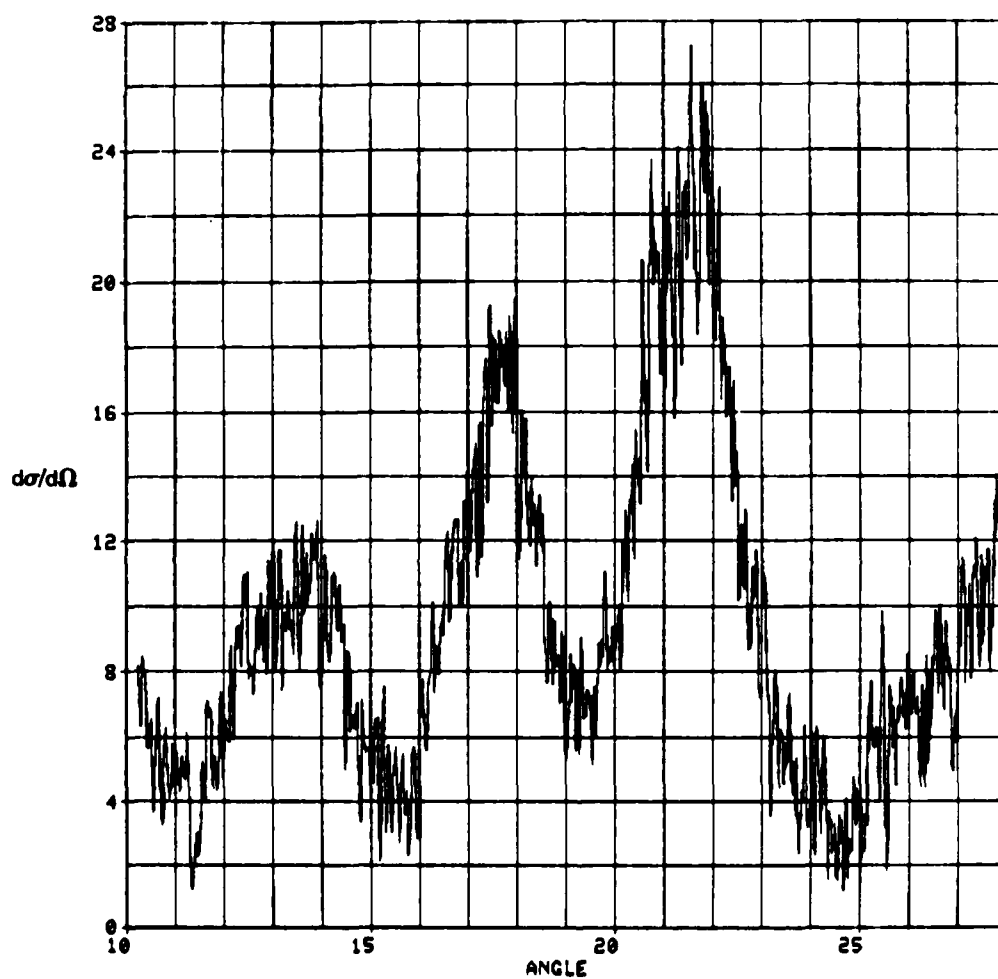


Figure 26. Differential Scattering Cross Section, Channel B,
Particle 4, Sample 1

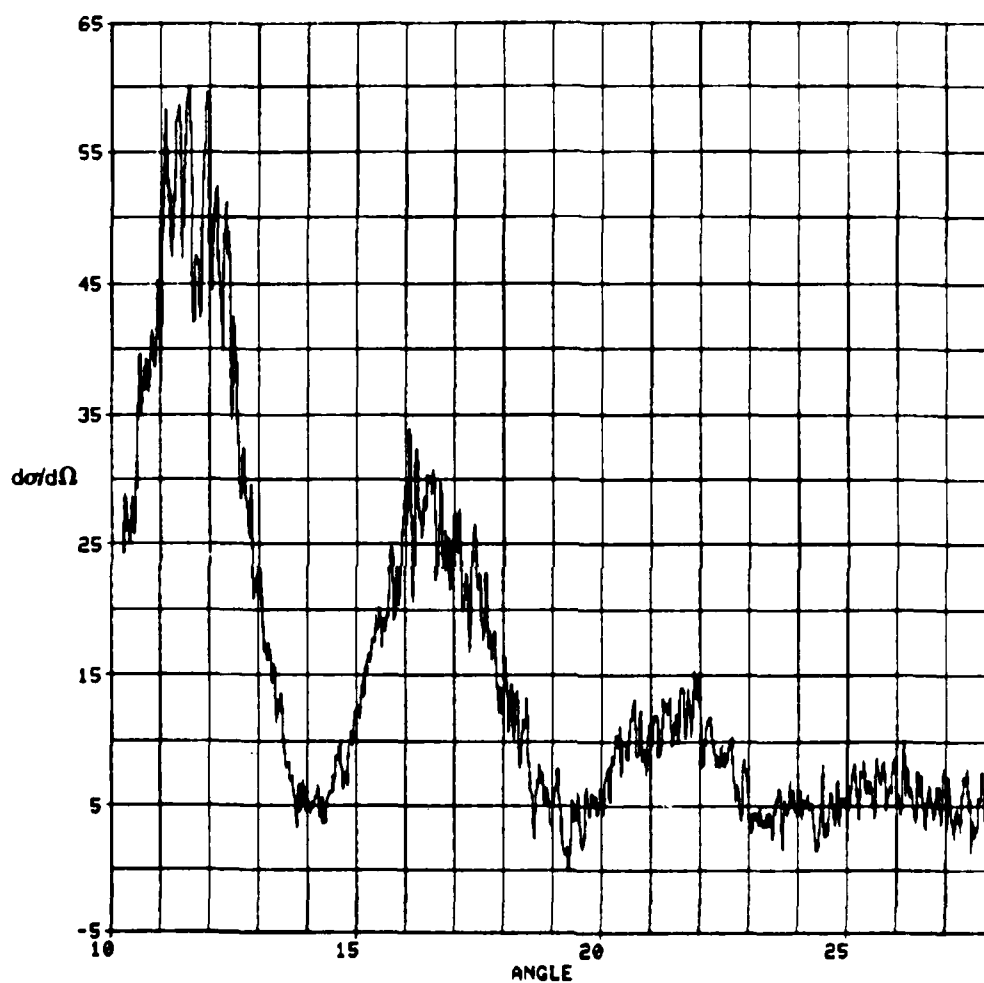


Figure 27. Differential Scattering Cross Section, Channel A, Particle 4, Sample 2

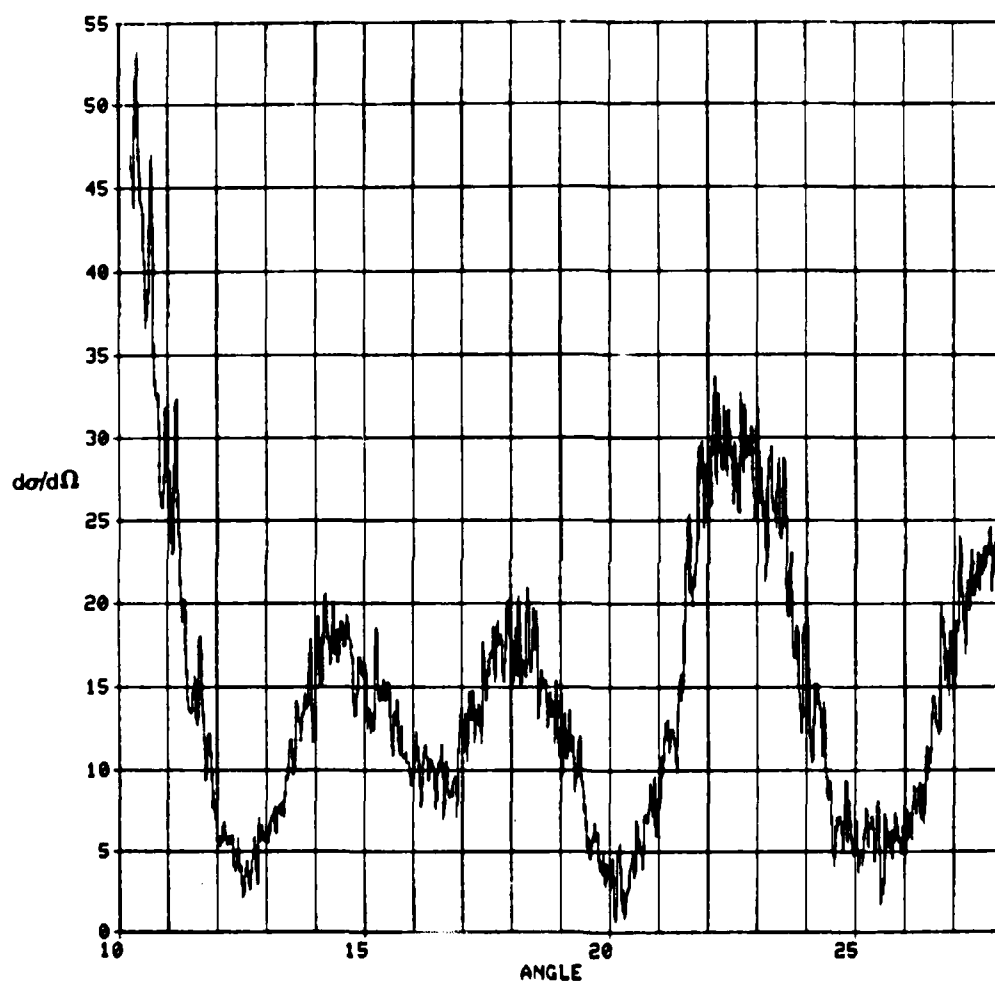


Figure 28. Differential Scattering Cross Section, Channel B, Particle 4, Sample 2

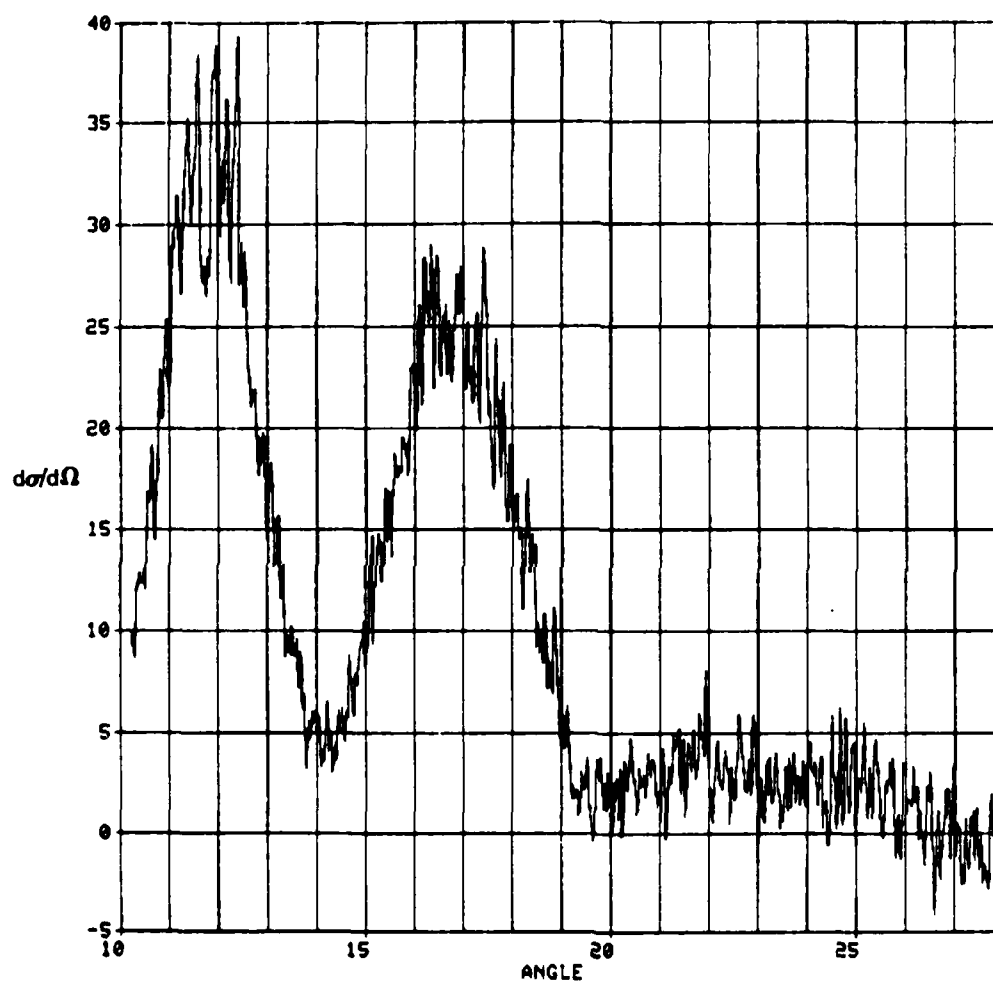


Figure 29. Differential Scattering Cross Section, Channel A,
Particle 4, Sample 3

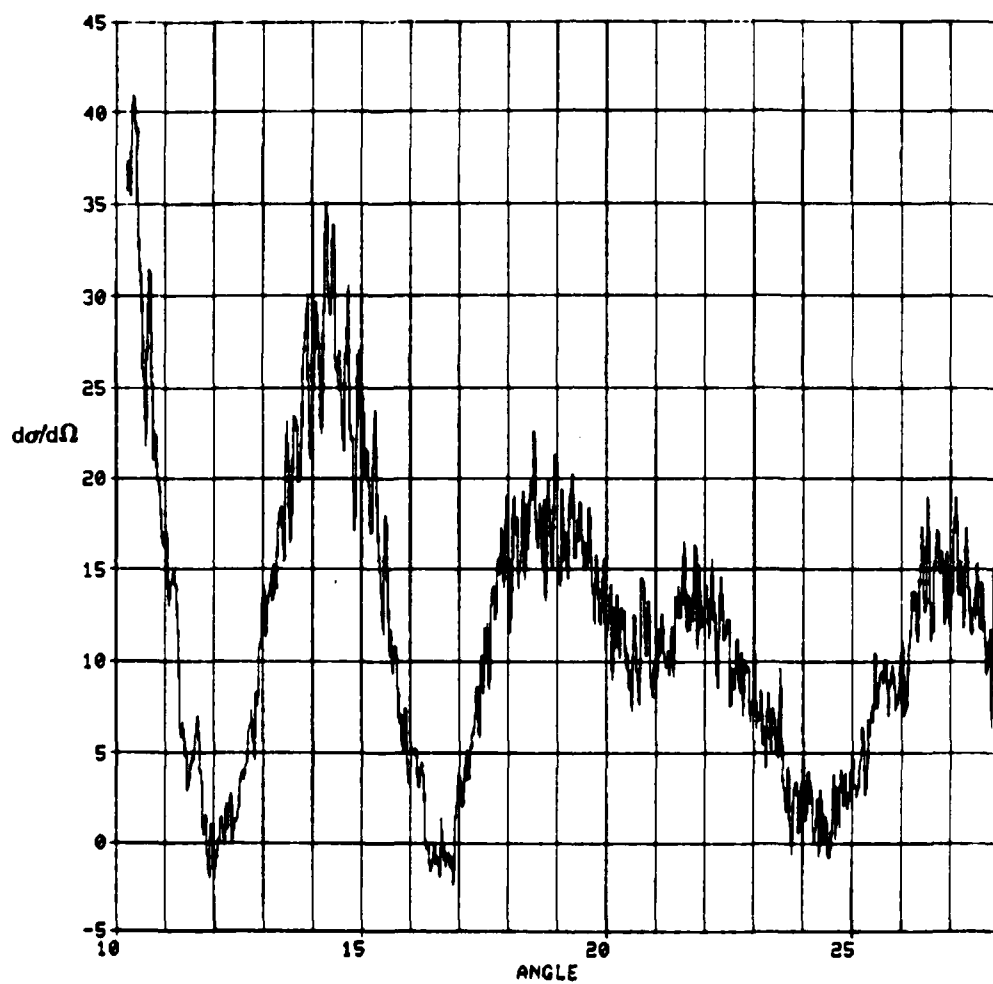


Figure 30. Differential Scattering Cross Section, Channel B,
Particle 4, Sample 3

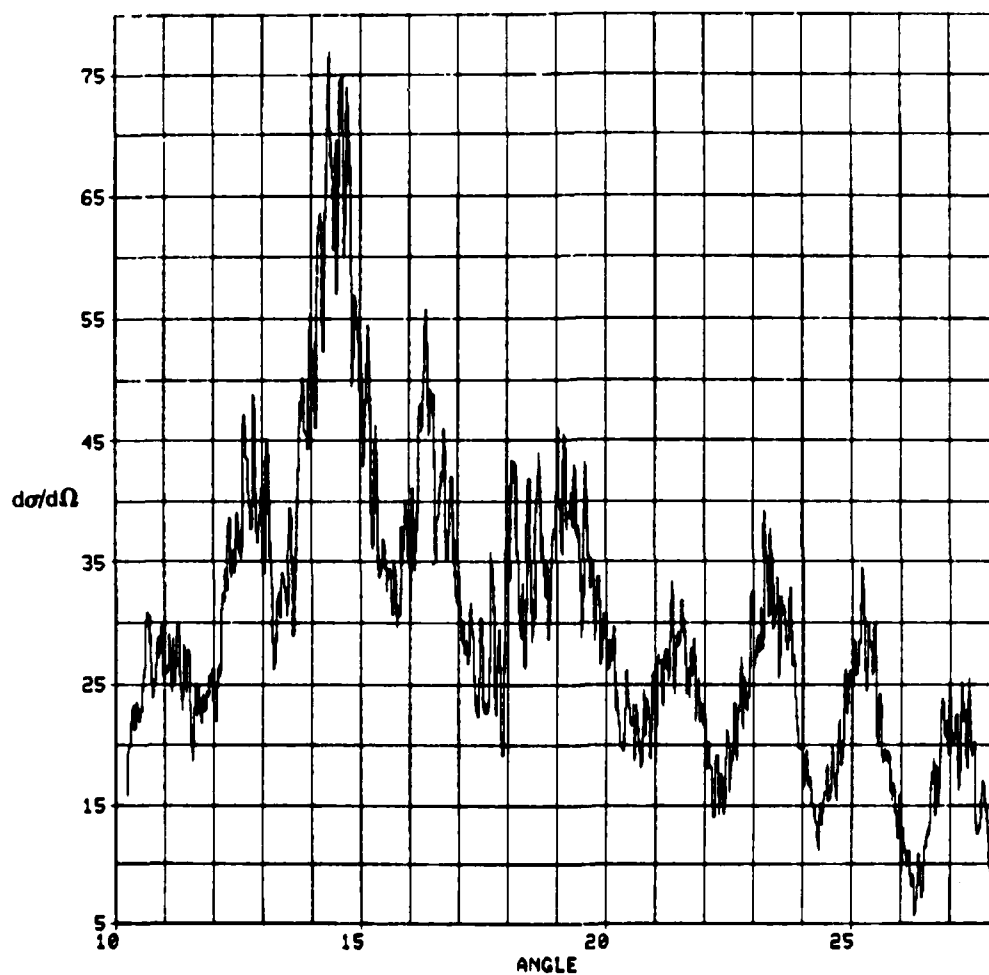


Figure 31. Differential Scattering Cross Section, Channel A,
Particle 5, Sample 1

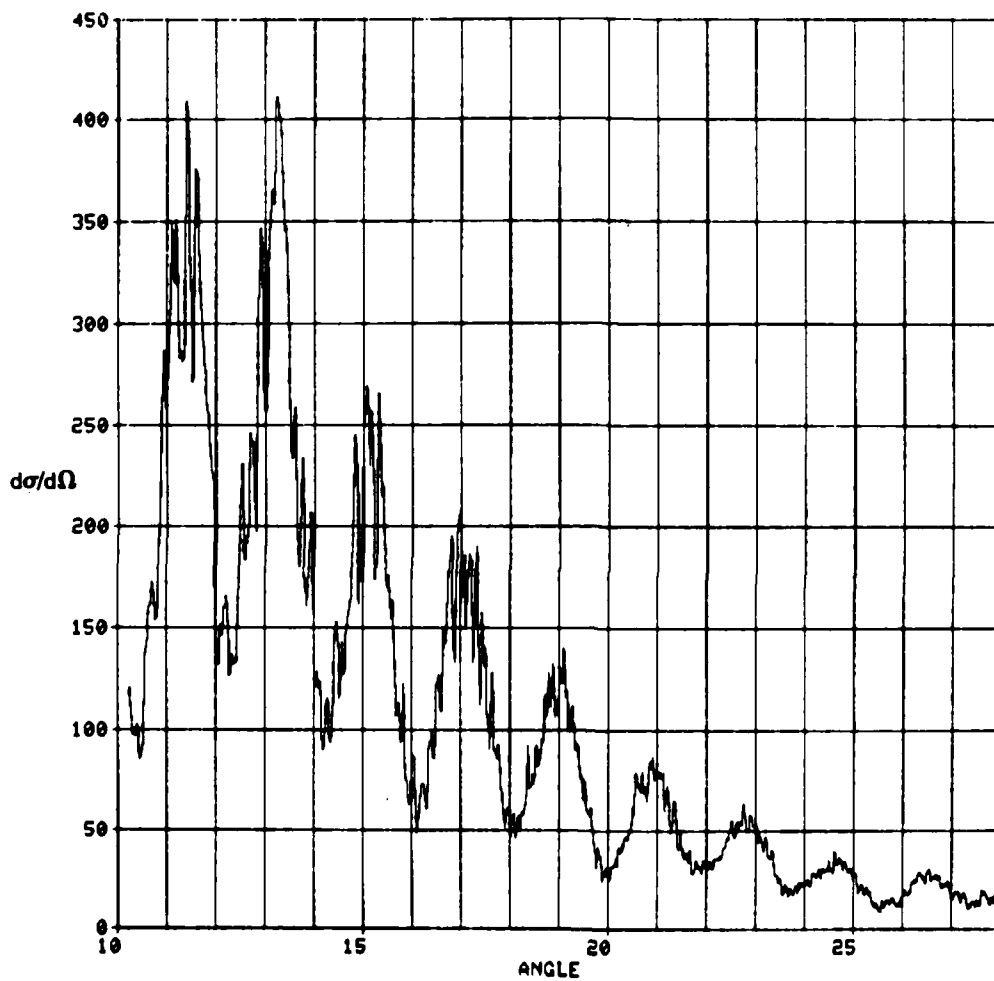


Figure 32. Differential Scattering Cross Section, Channel B,
Particle 5, Sample 1

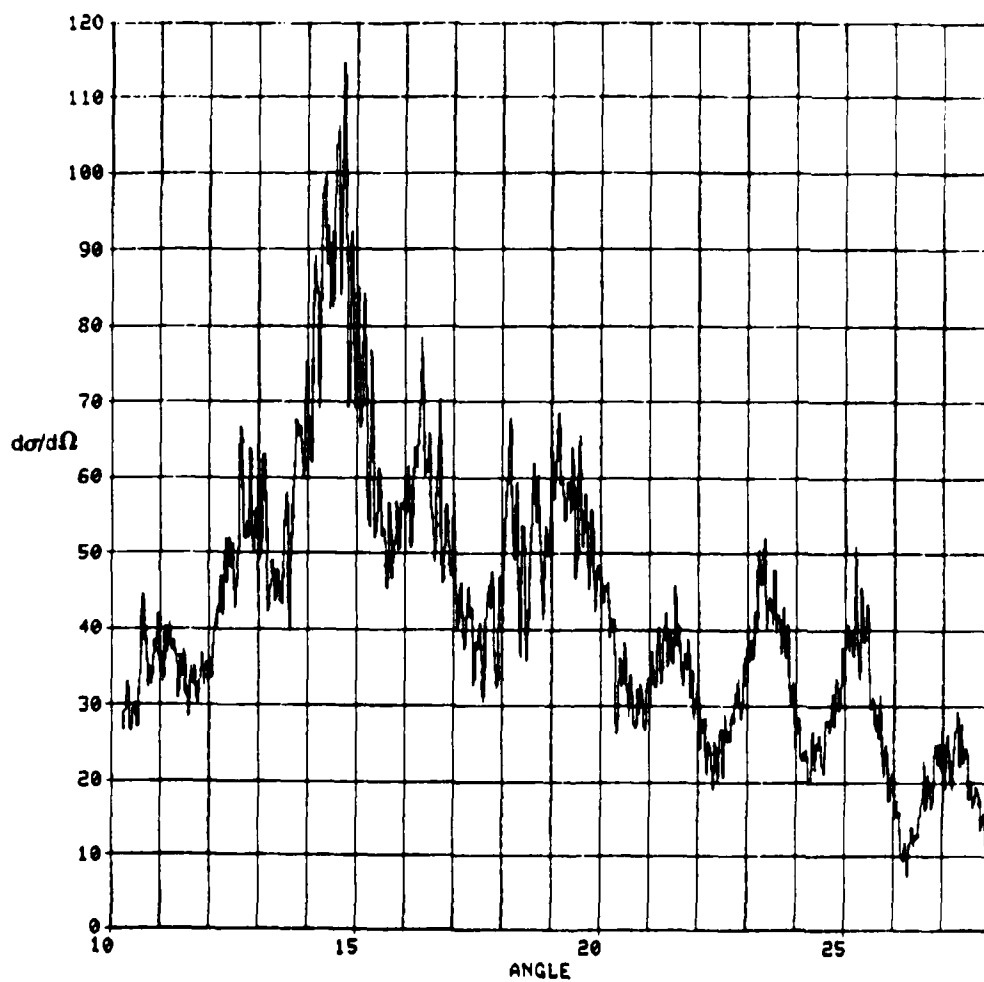


Figure 33. Differential Scattering Cross Section, Channel A, Particle 5, Sample 2

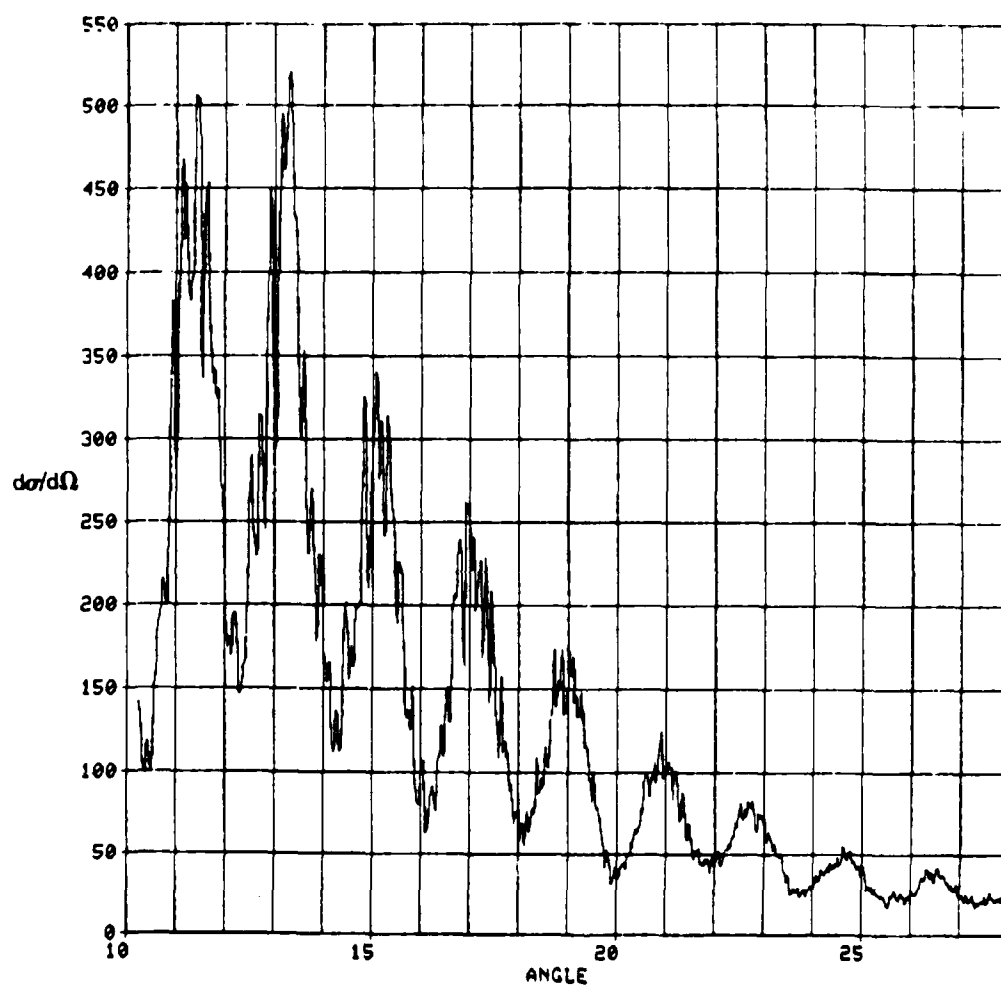


Figure 34. Differential Scattering Cross Section, Channel B,
Particle 5, Sample 2

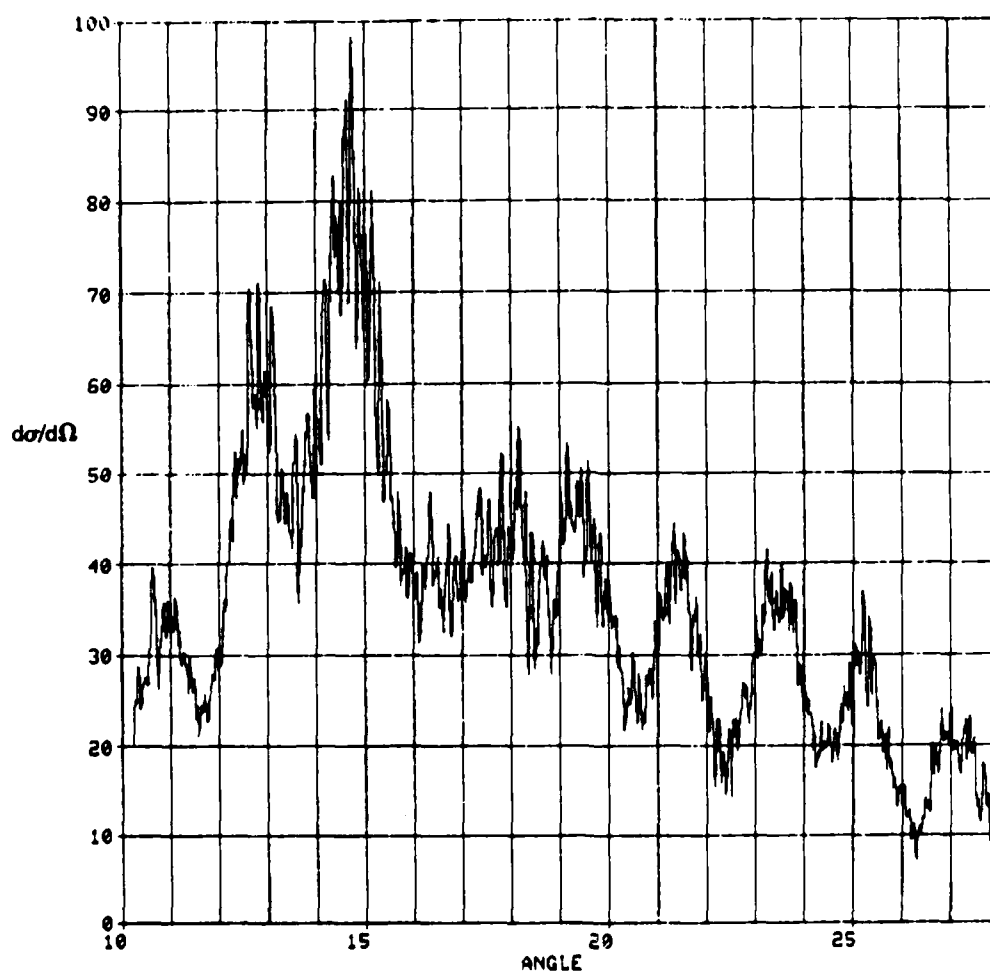


Figure 35. Differential Scattering Cross Section, Channel A, Particle 5, Sample 3

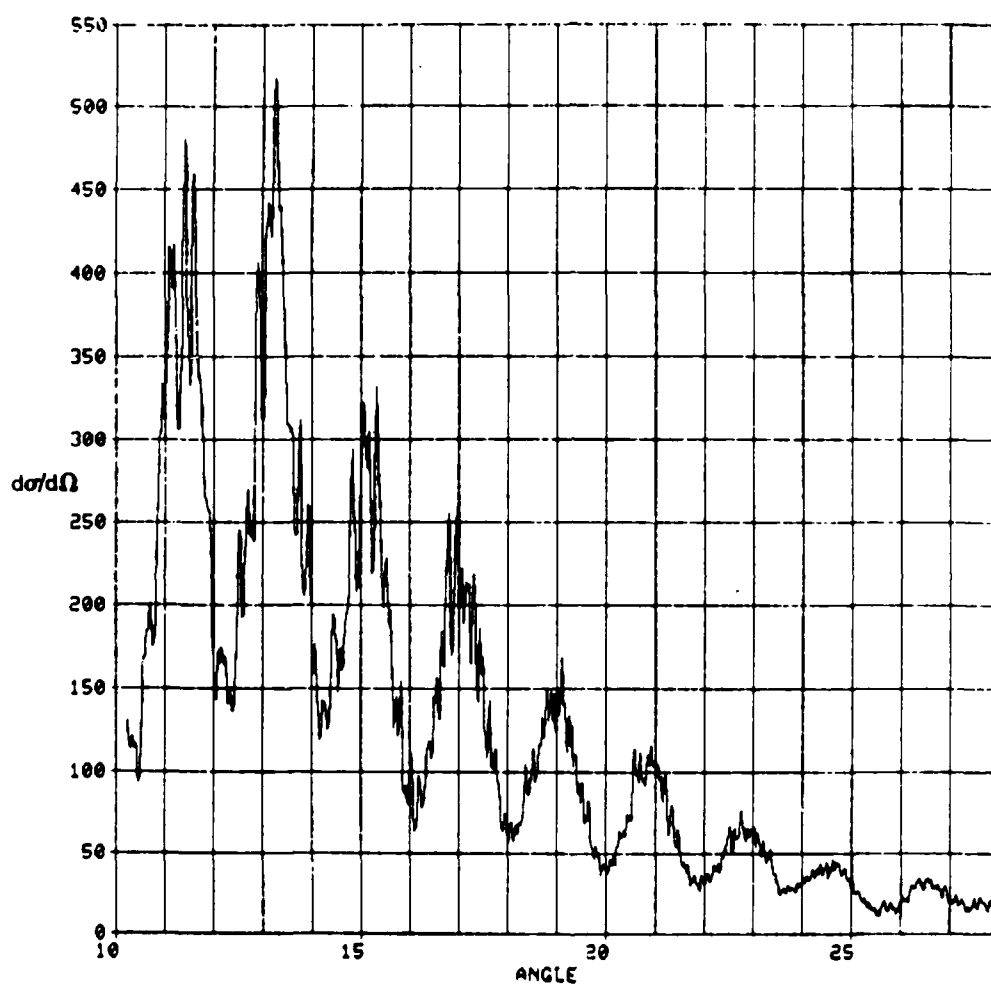


Figure 36. Differential Scattering Cross Section, Channel B,
Particle 5, Sample 3

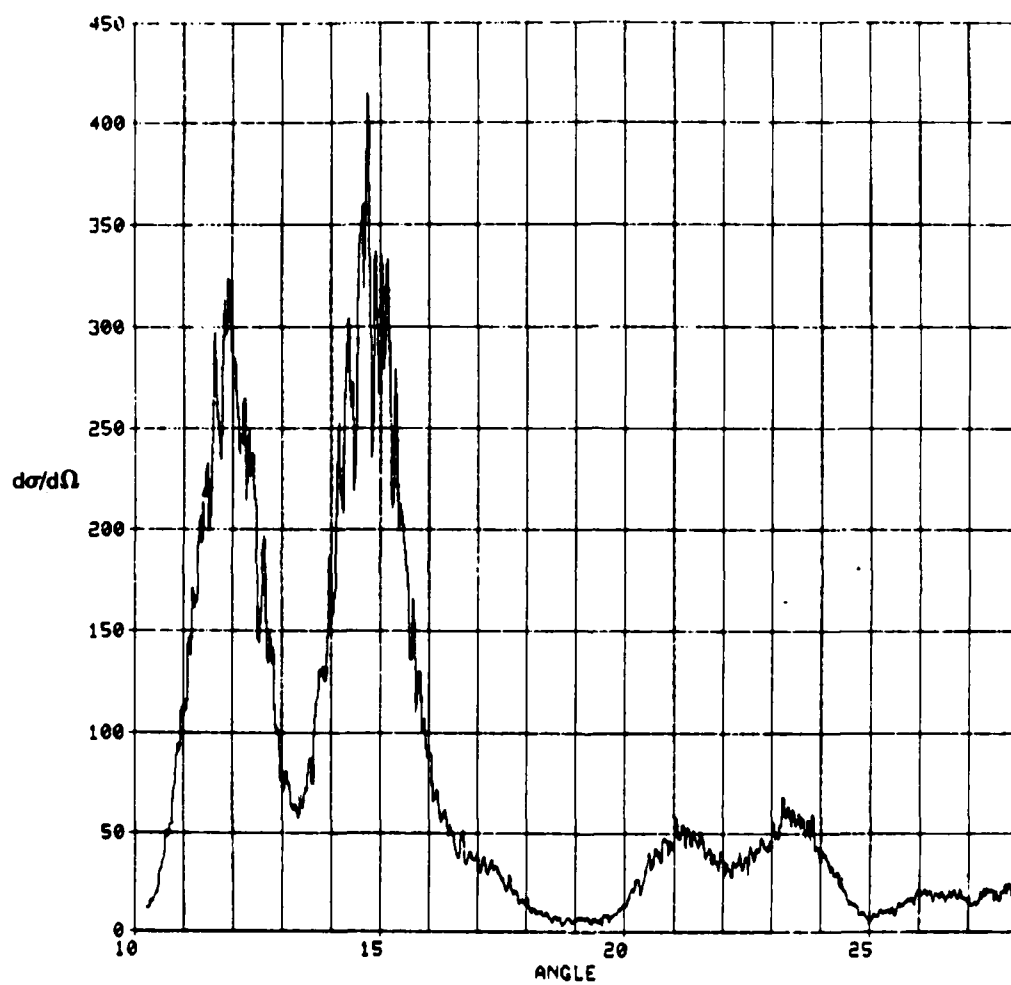


Figure 37. Differential Scattering Cross Section, Channel A,
Particle 6, Sample 1

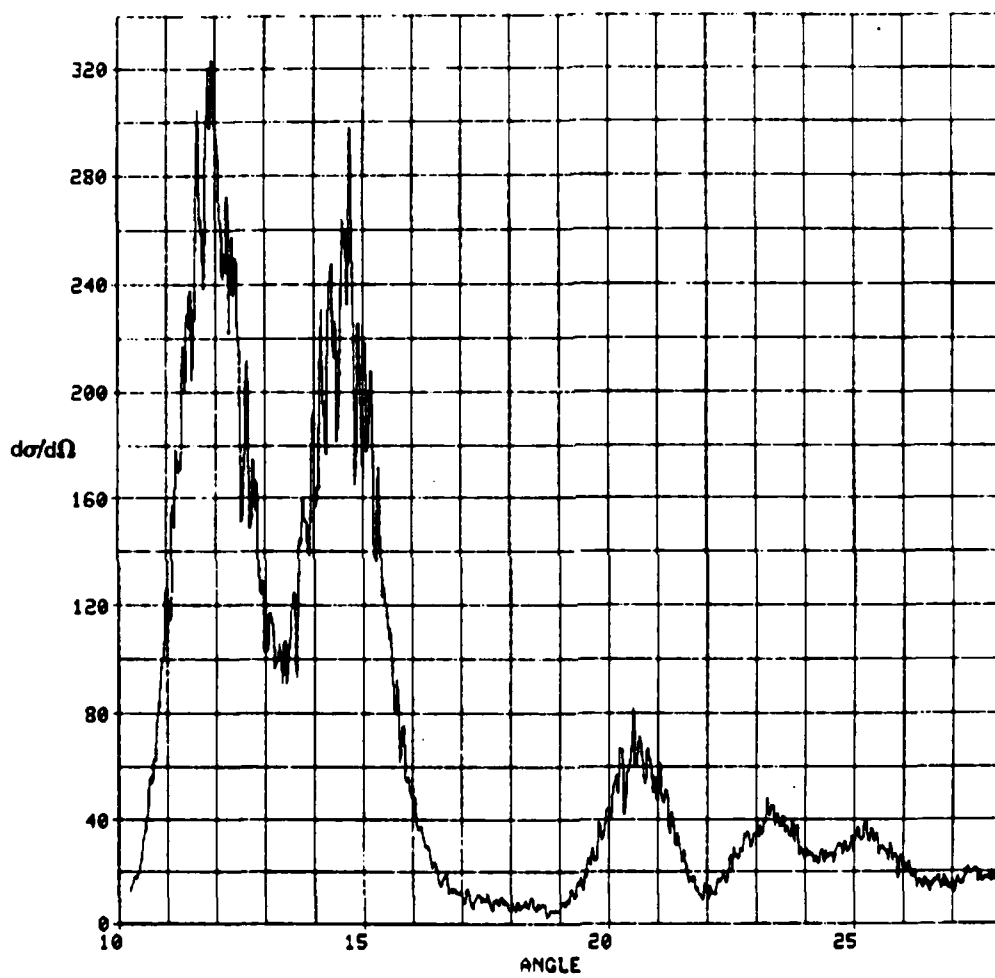


Figure 39. Differential Scattering Cross Section, Channel A, Particle 6, Sample 2

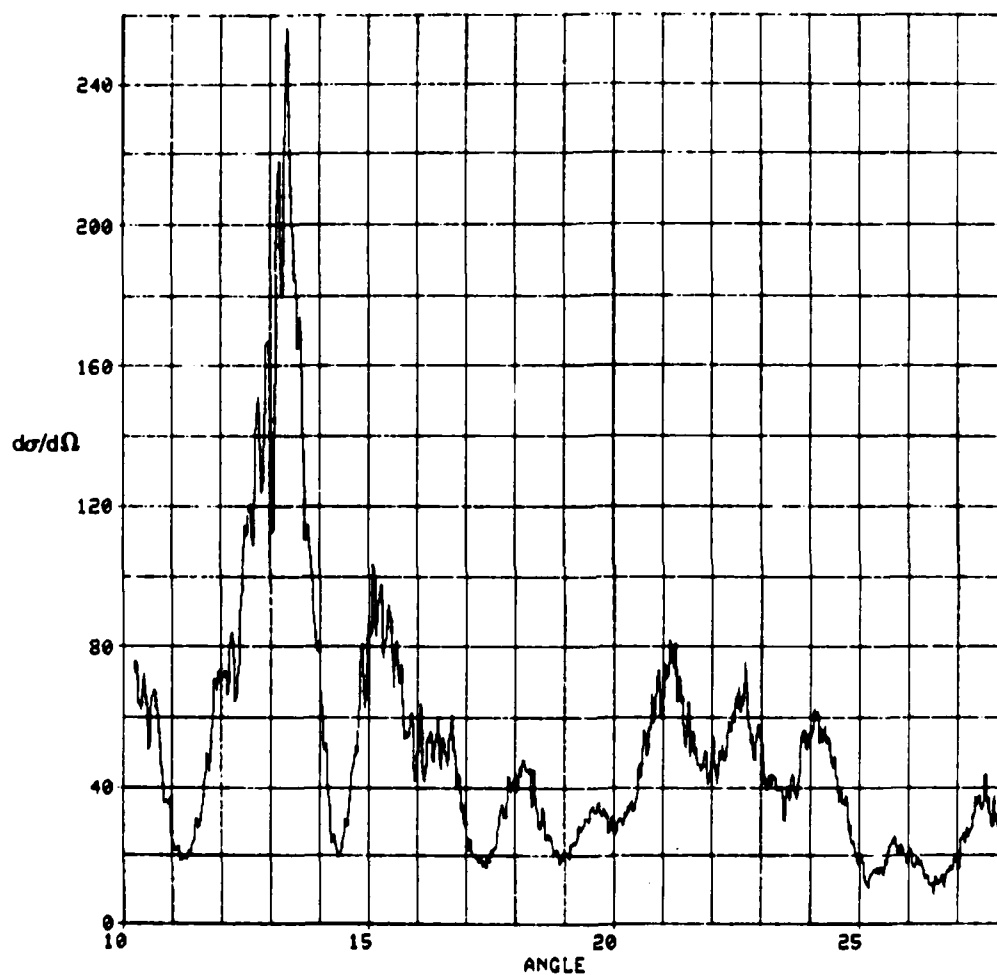


Figure 38. Differential Scattering Cross Section, Channel B, Particle 6, Sample 1

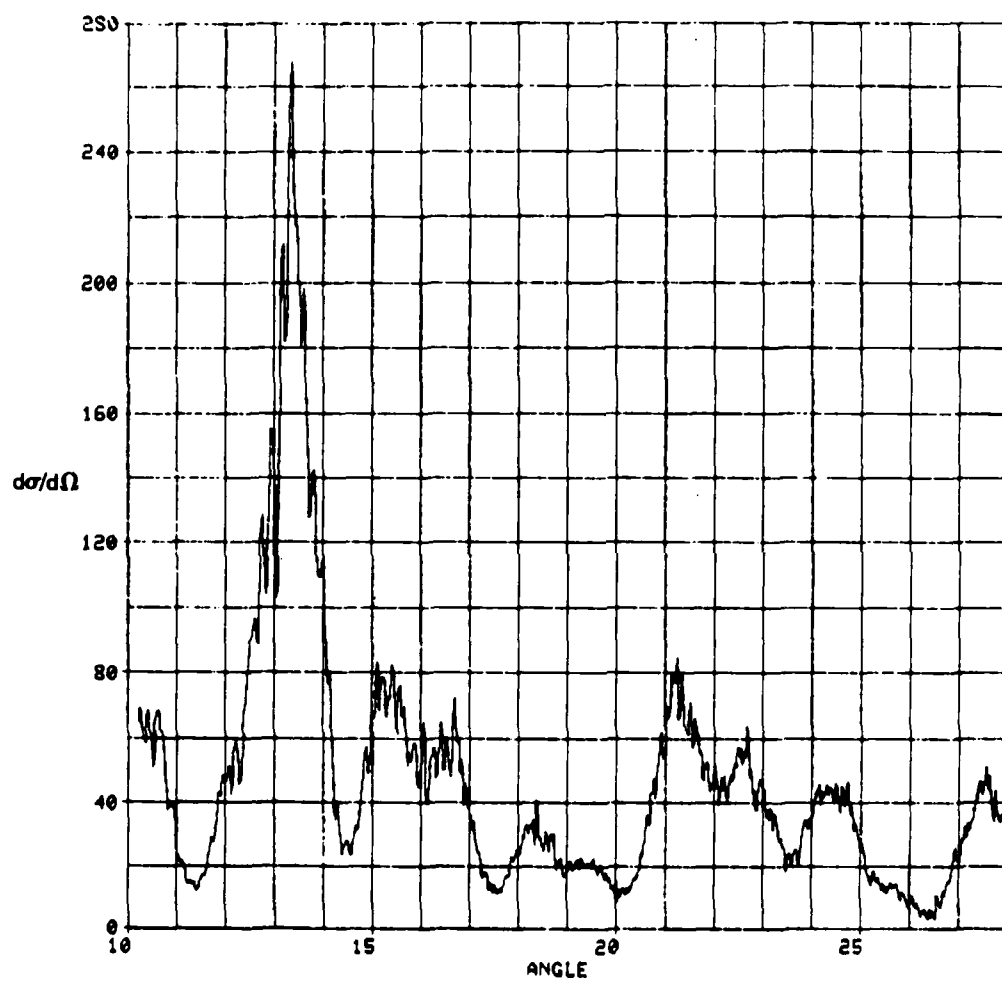


Figure 40. Differential Scattering Cross Section, Channel B,
Particle 6, Sample 2

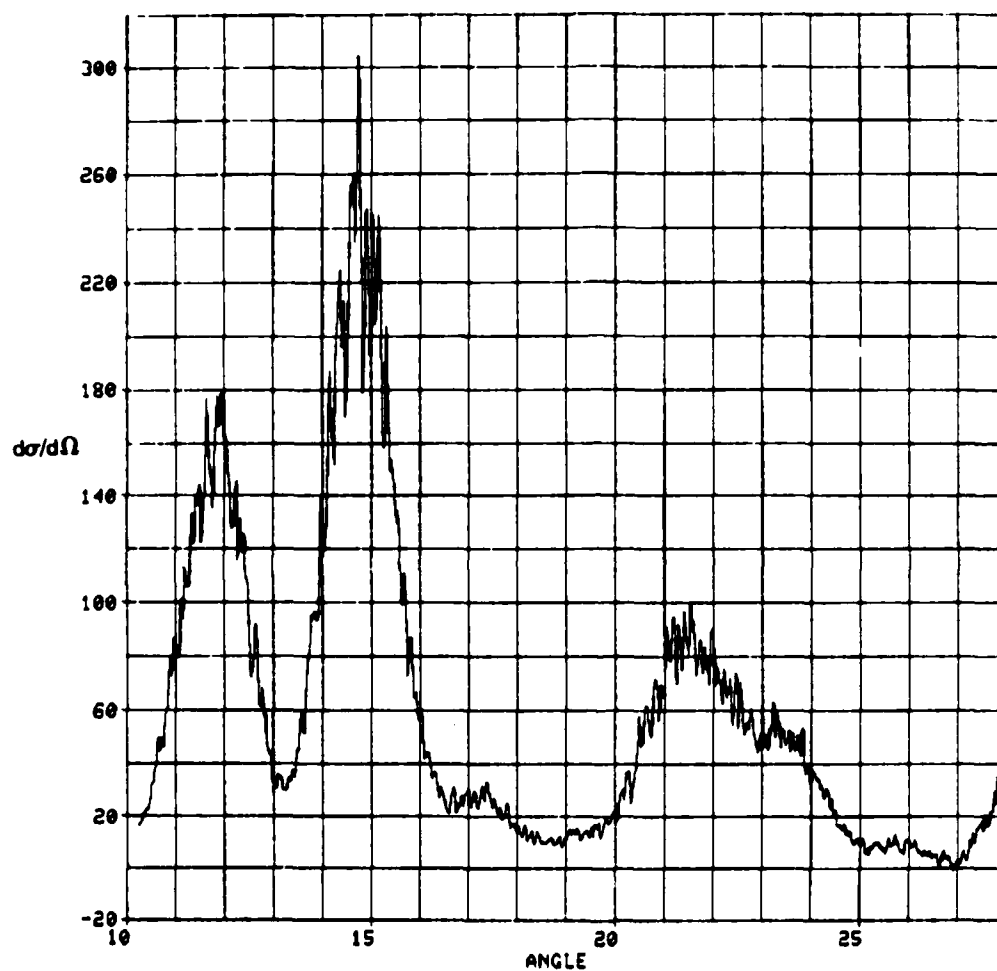


Figure 41. Differential Scattering Cross Section, Channel A,
Particle 6, Sample 3

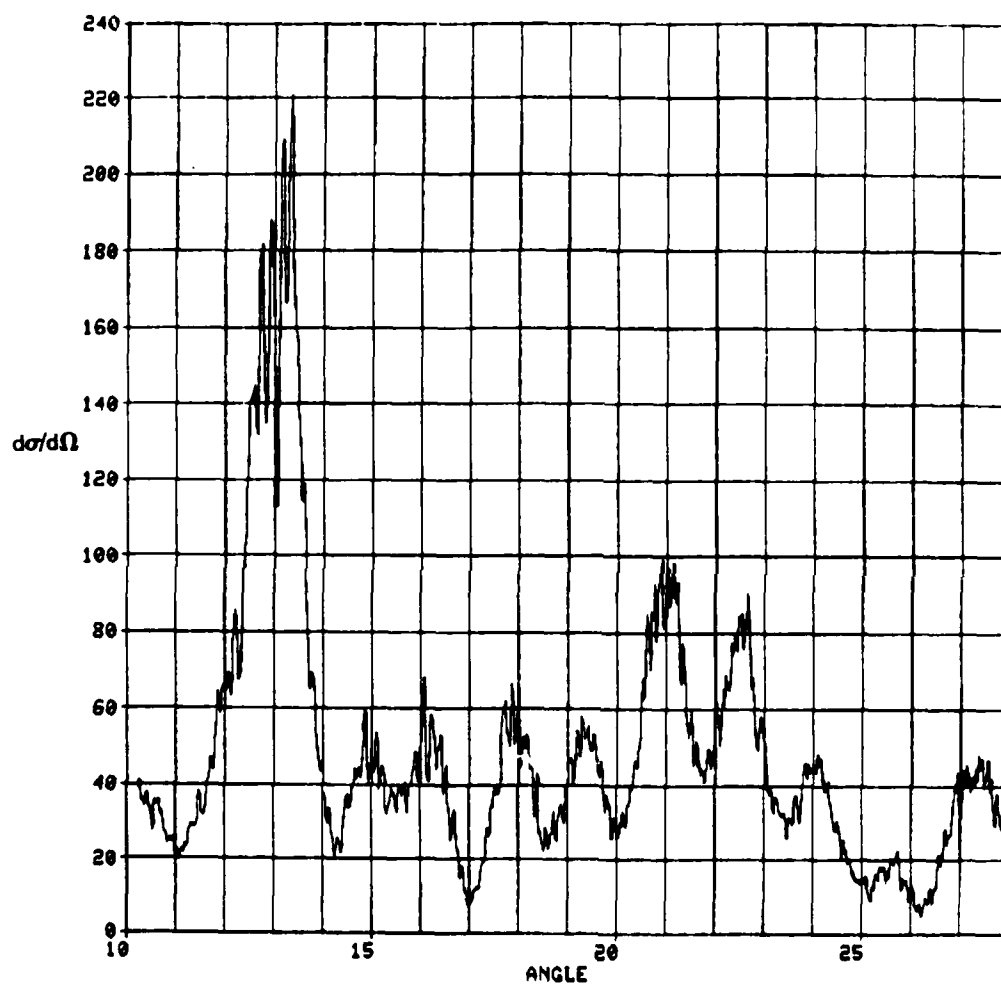


Figure 42. Differential Scattering Cross Section, Channel B,
Particle 6, Sample 3

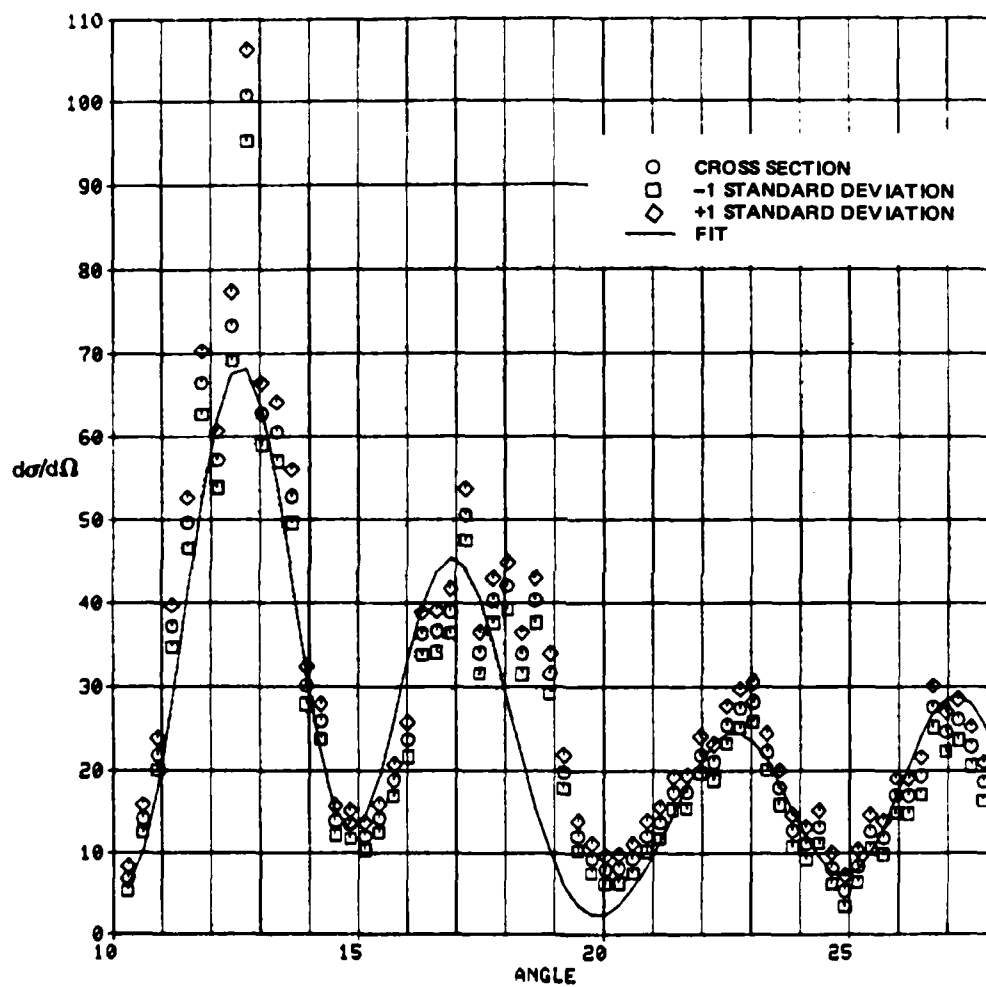


Figure 43. Mie Theory Fit, Channel A, Particle 1, Sample 1
(subset of Fig. 7)

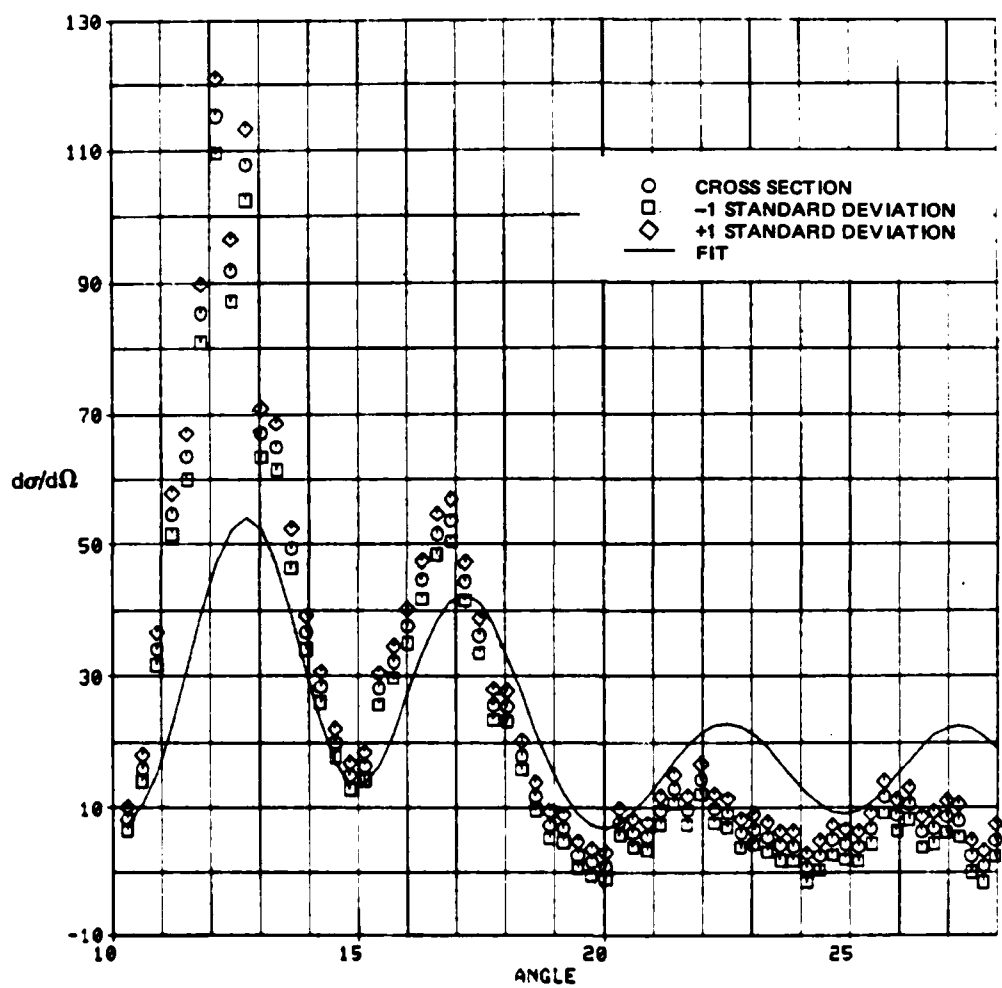


Figure 44. Mie Theory Fit, Channel 8, Particle 1, Sample 1
(subset of Fig. 8)

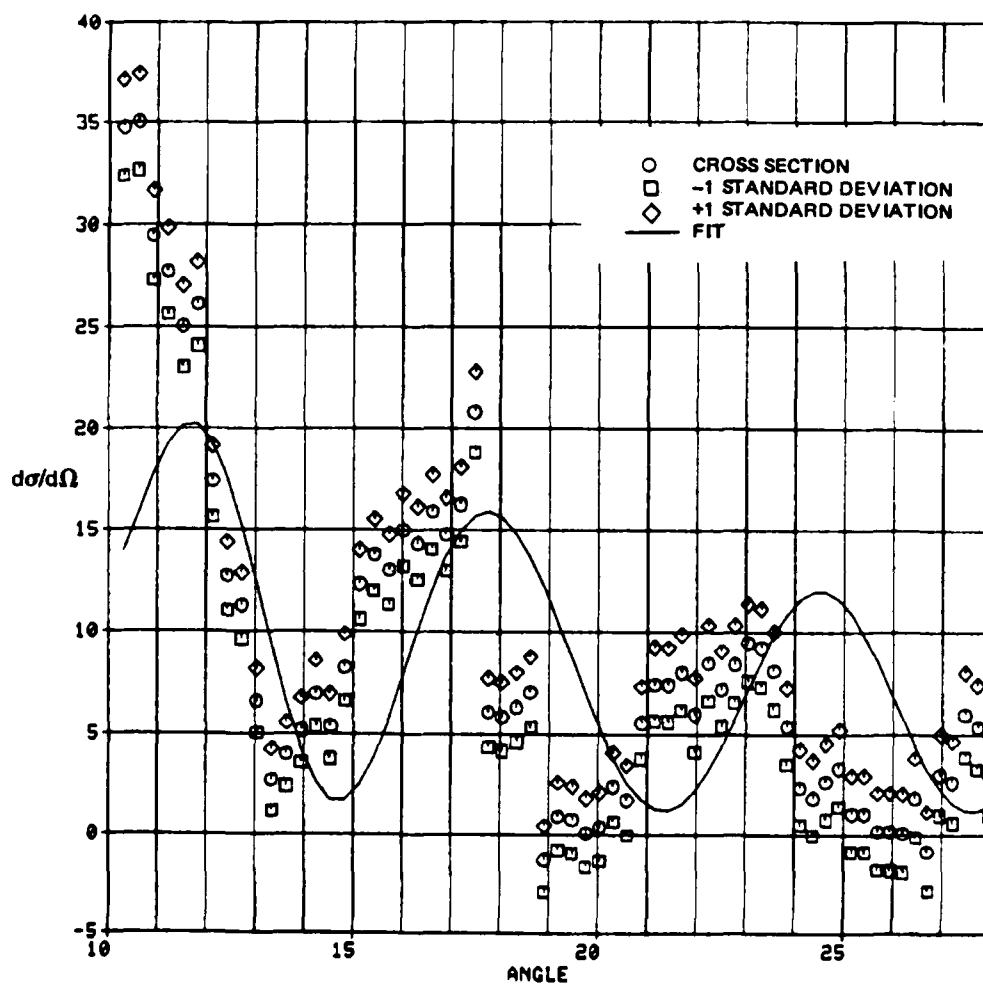


Figure 45. Mie Theory Fit, Channel A, Particle 2, Sample 1
(subset of Fig. 13)

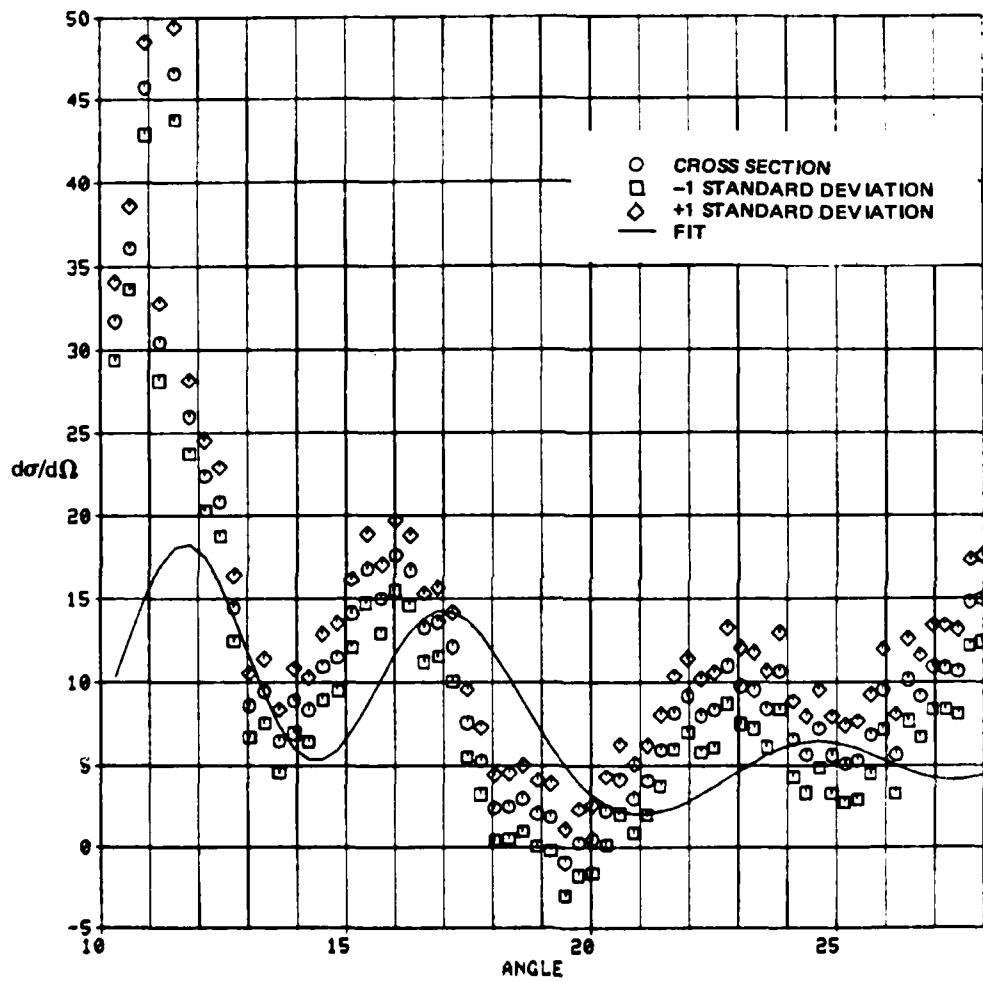


Figure 46. Mie Theory Fit, Channel B, Particle 2, Sample 1
(subset of Fig. 14)

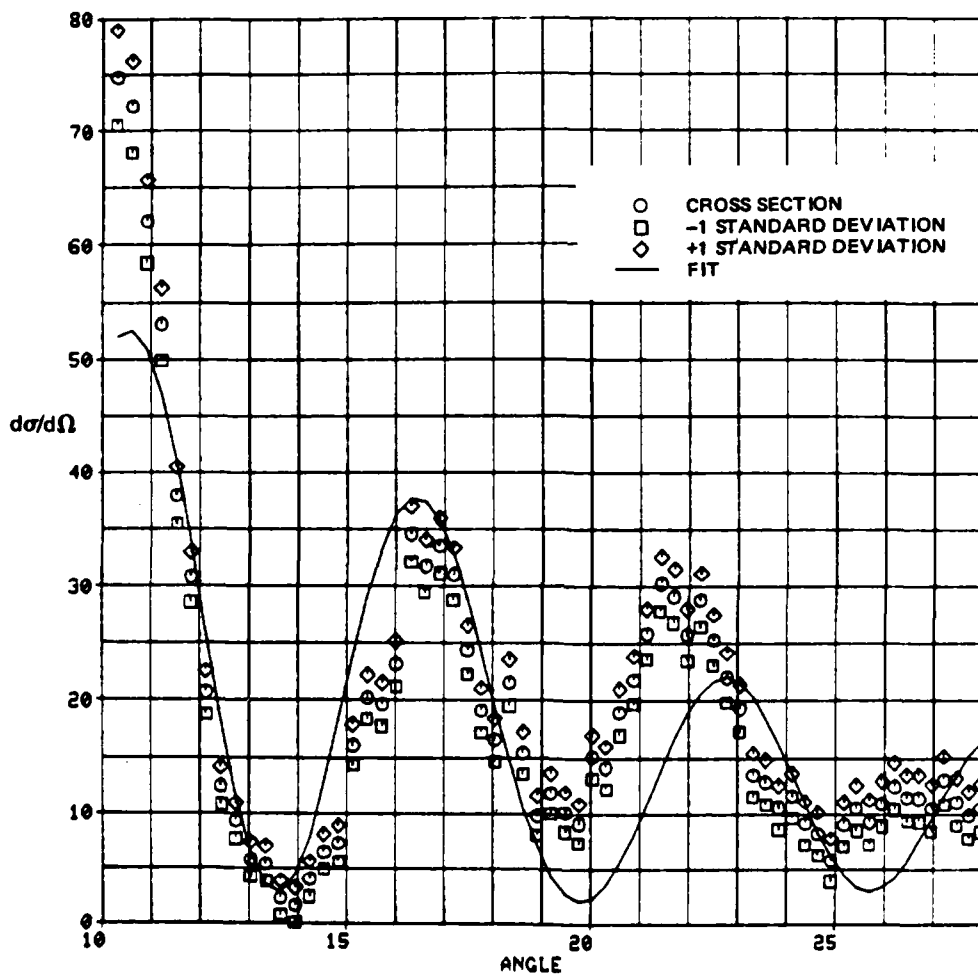


Figure 47. Mie Theory Fit, Channel A, Particle 3, Sample 1
(subset of Fig. 19)

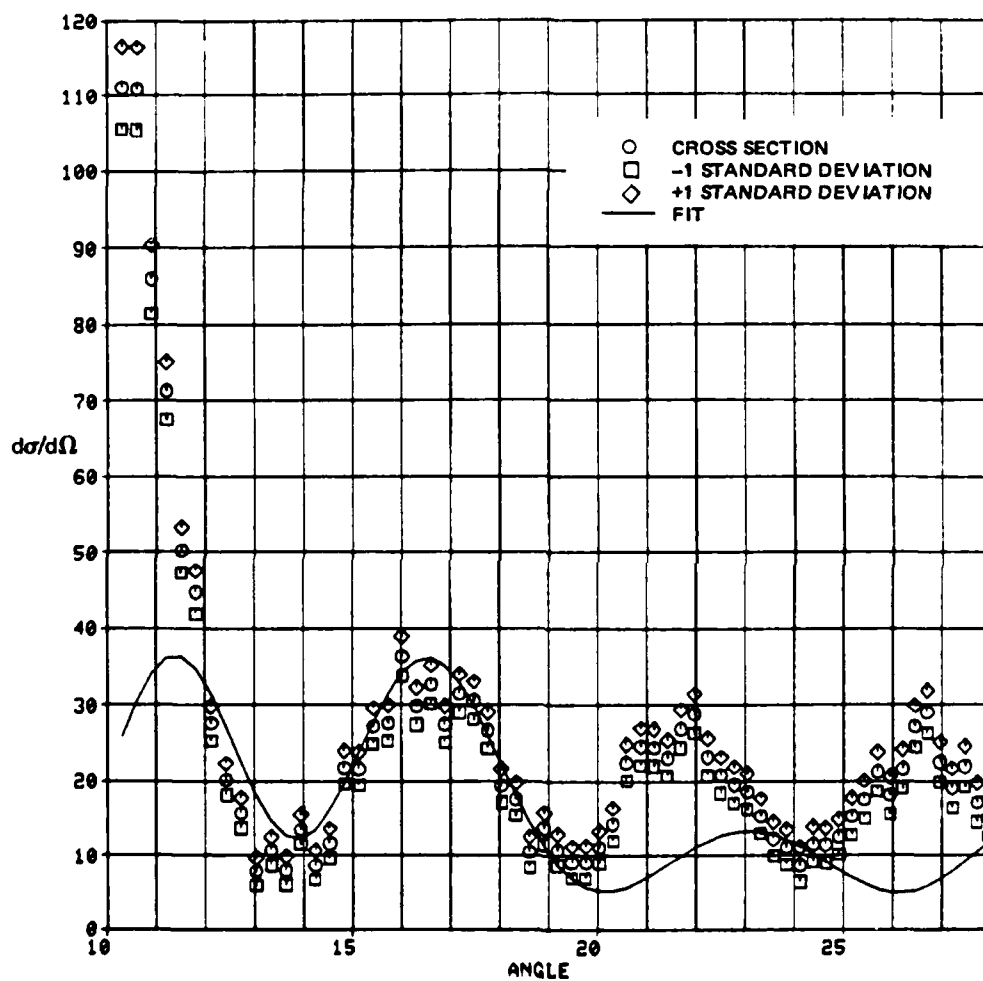


Figure 48. Mie Theory Fit, Channel B, Particle 3, Sample 1
(subset of Fig. 20)

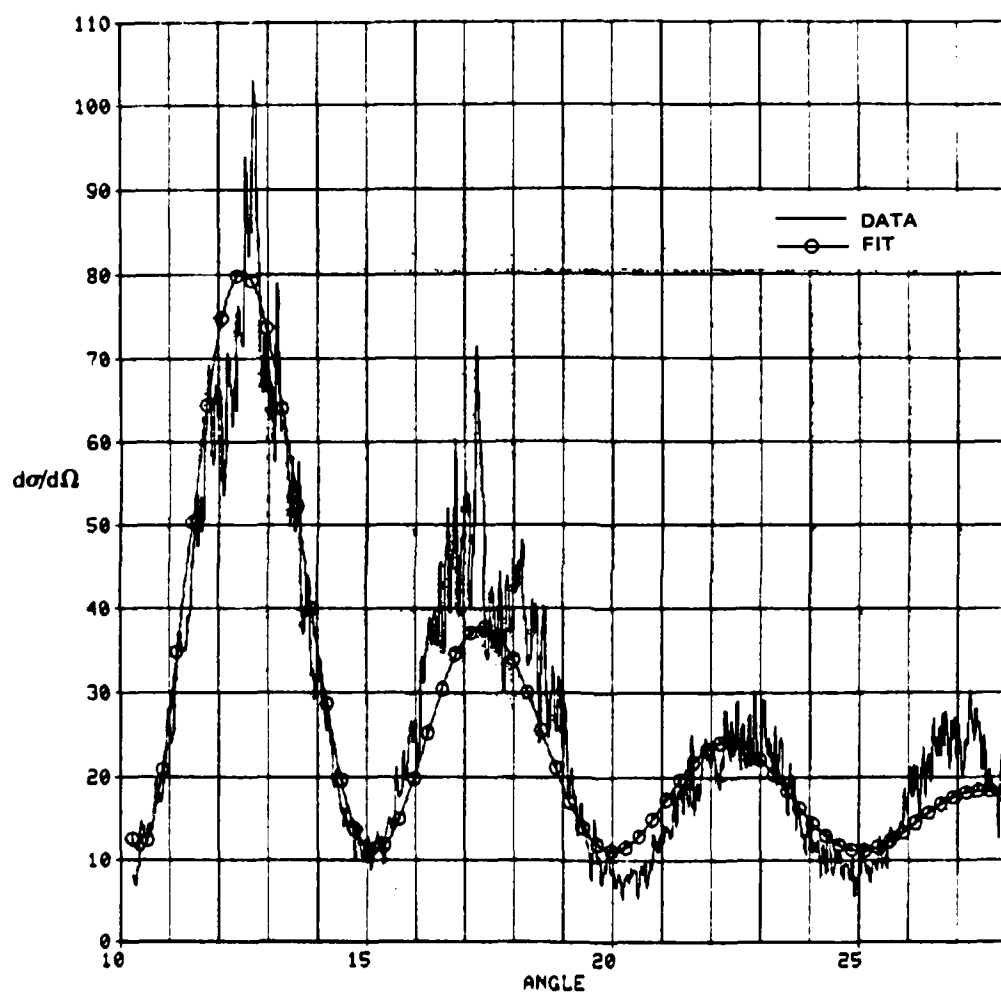


Figure 49. Diffraction Theory Fit, Channel A, Particle 1, Sample 1
(data from Fig. 7)

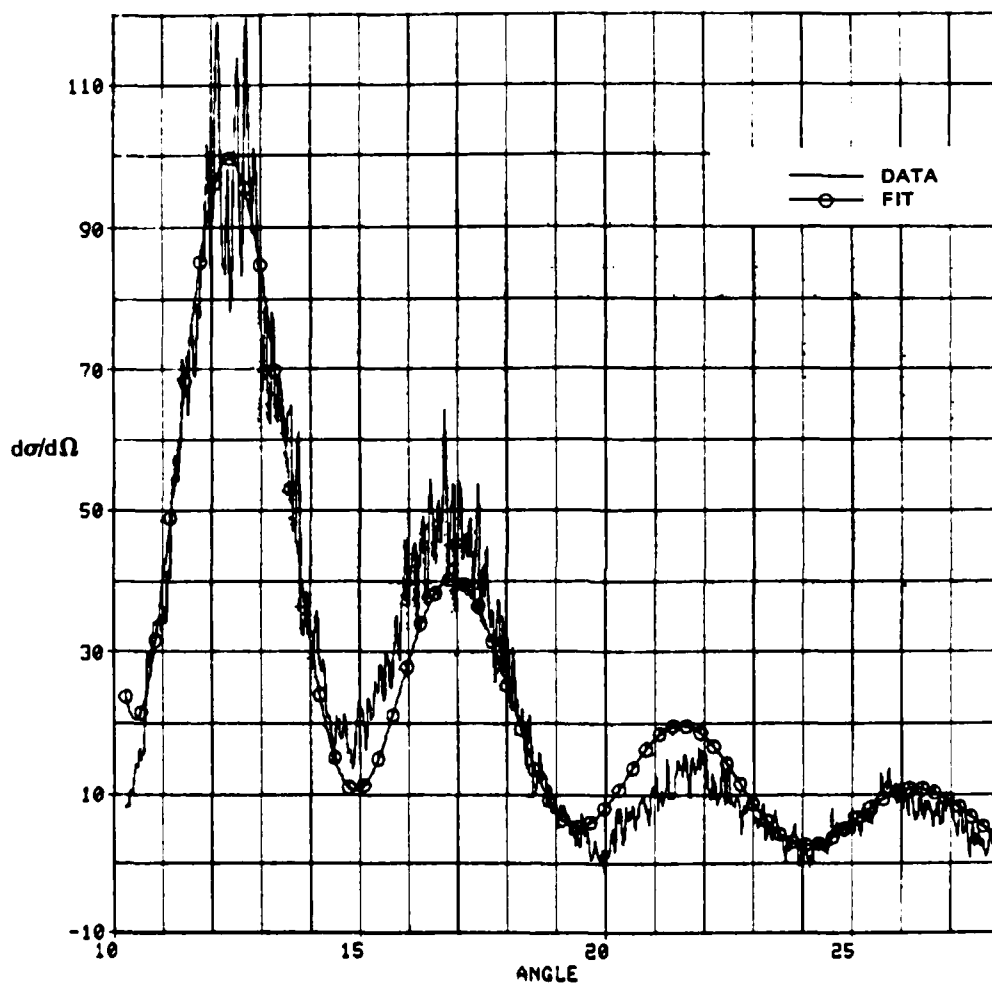


Figure 50. Diffraction Theory Fit, Channel B, Particle 1, Sample 1
(data from Fig. 8)

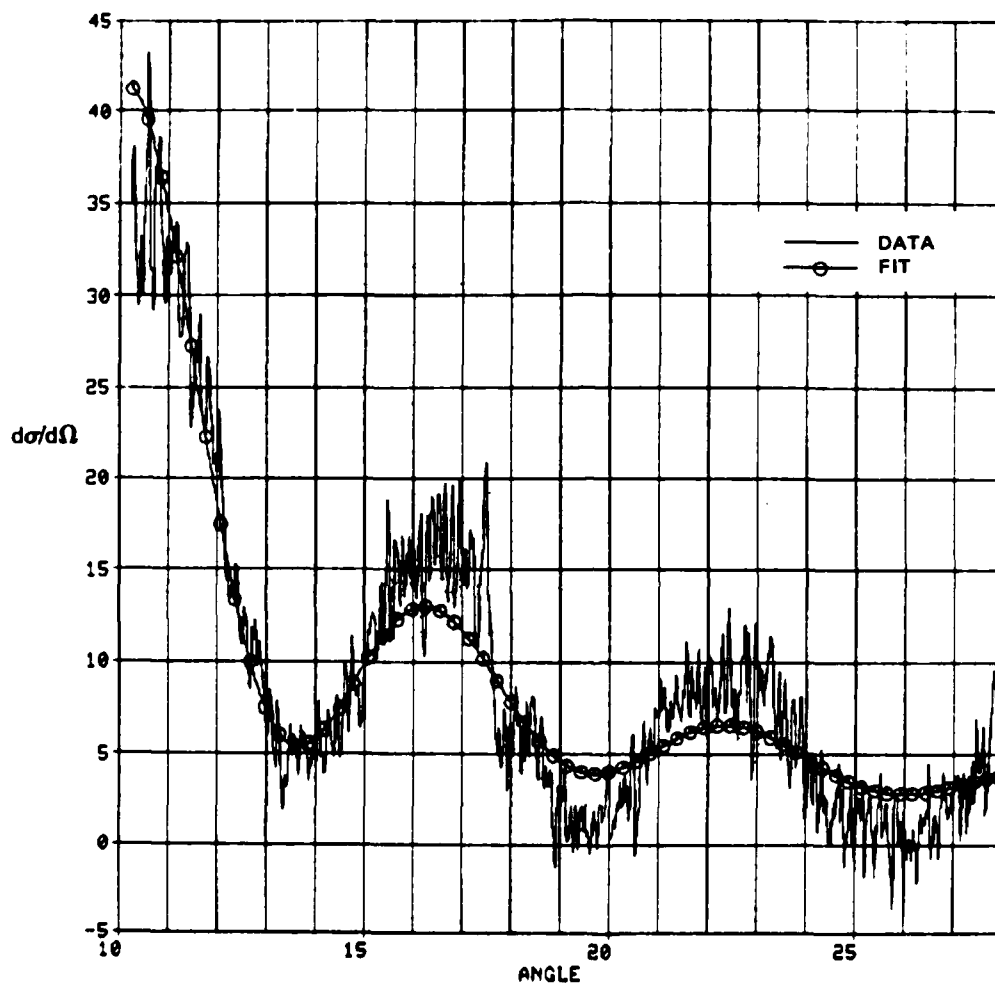


Figure 51. Diffraction Theory Fit, Channel A, Particle 2, Sample 1
(data from Fig. 13)

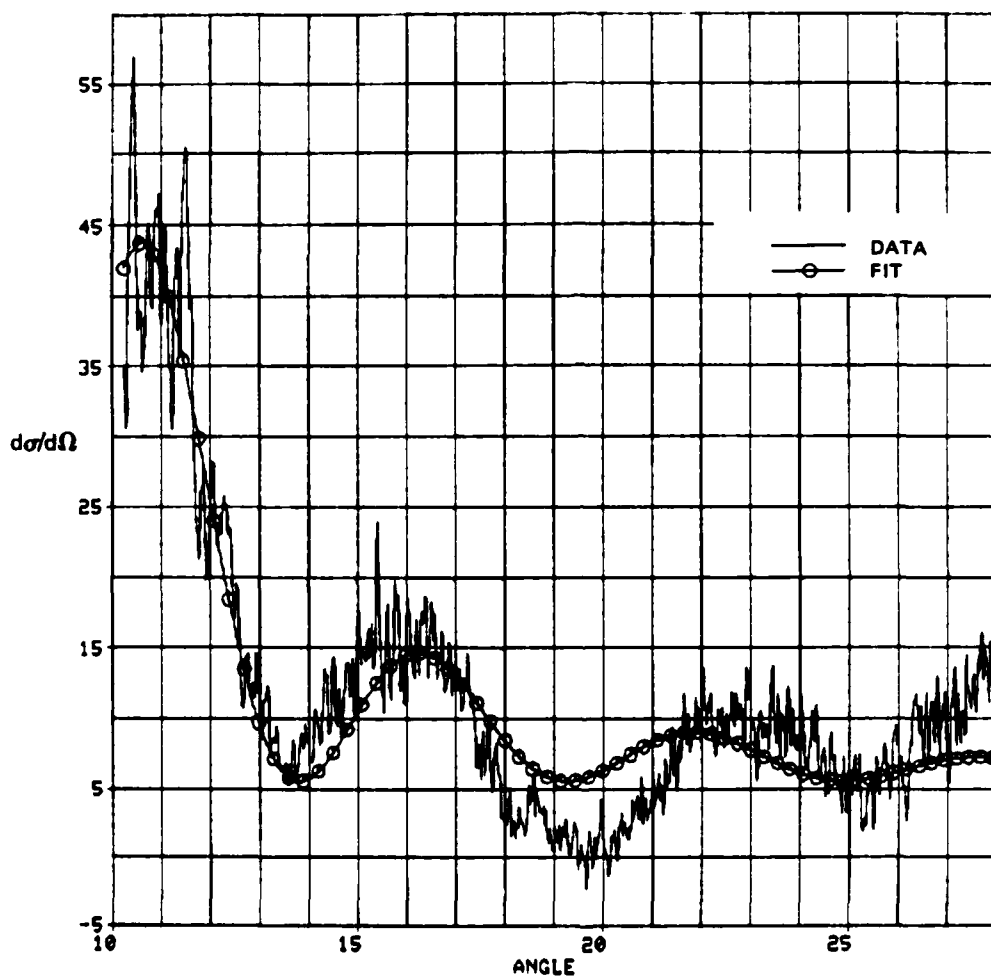


Figure 52. Diffraction Theory Fit, Channel A, Particle 2, Sample 1
(data from Fig. 14)

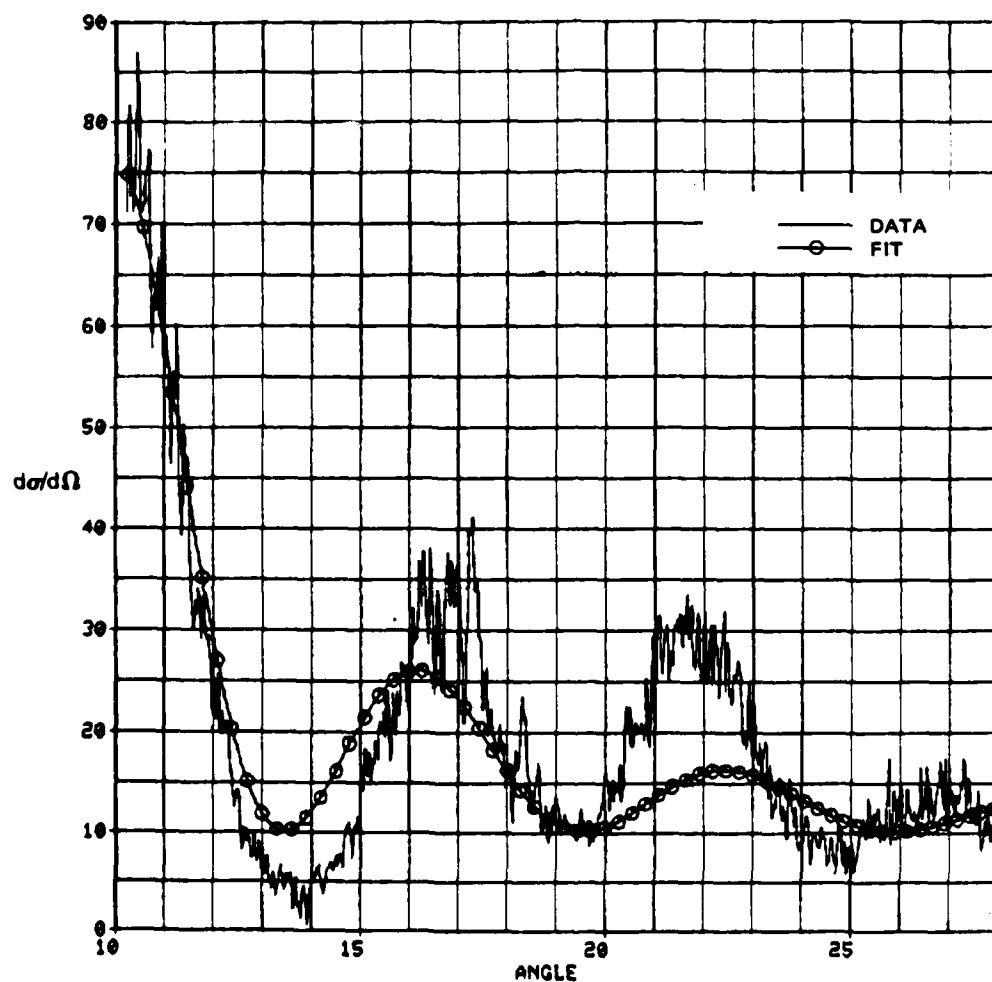


Figure 53. Diffraction Theory Fit, Channel A, Particle 3, Sample 1
(data from Fig. 19)

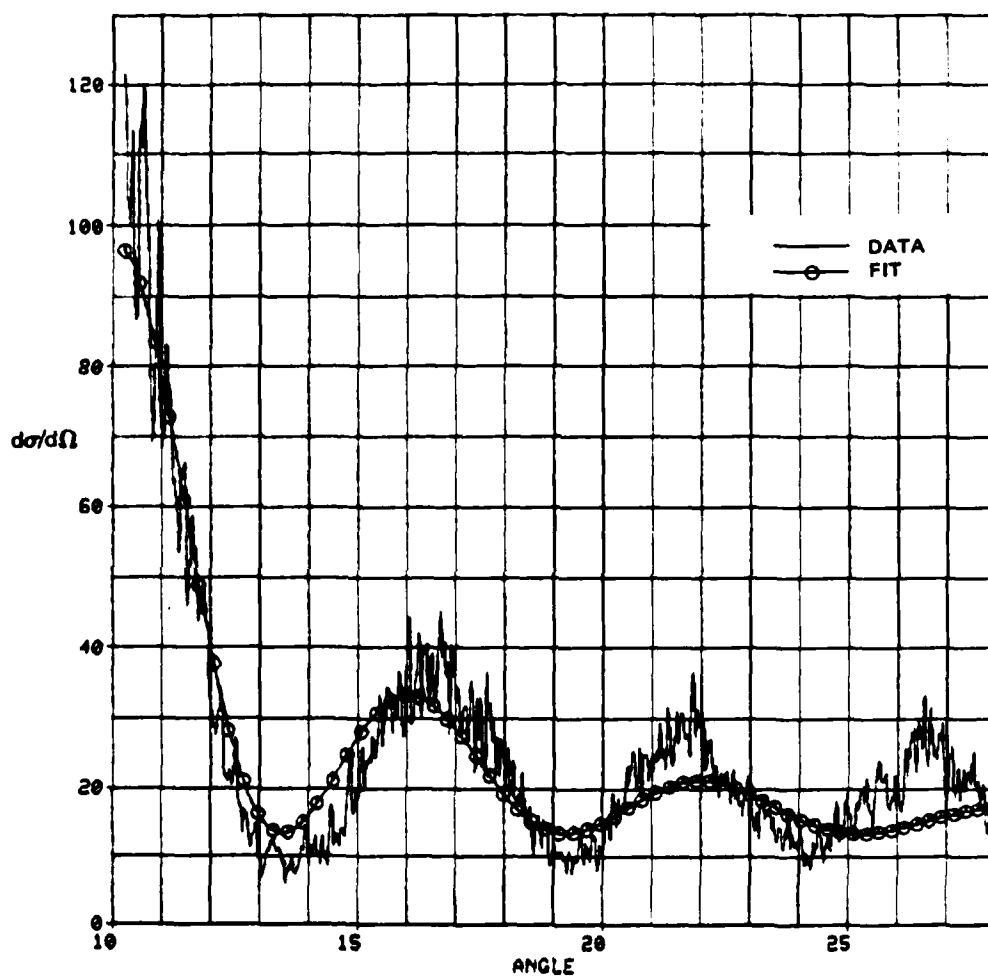


Figure 54. Diffraction Theory Fit, Channel B, Particle 3, Sample 1
(data from Fig. 20)

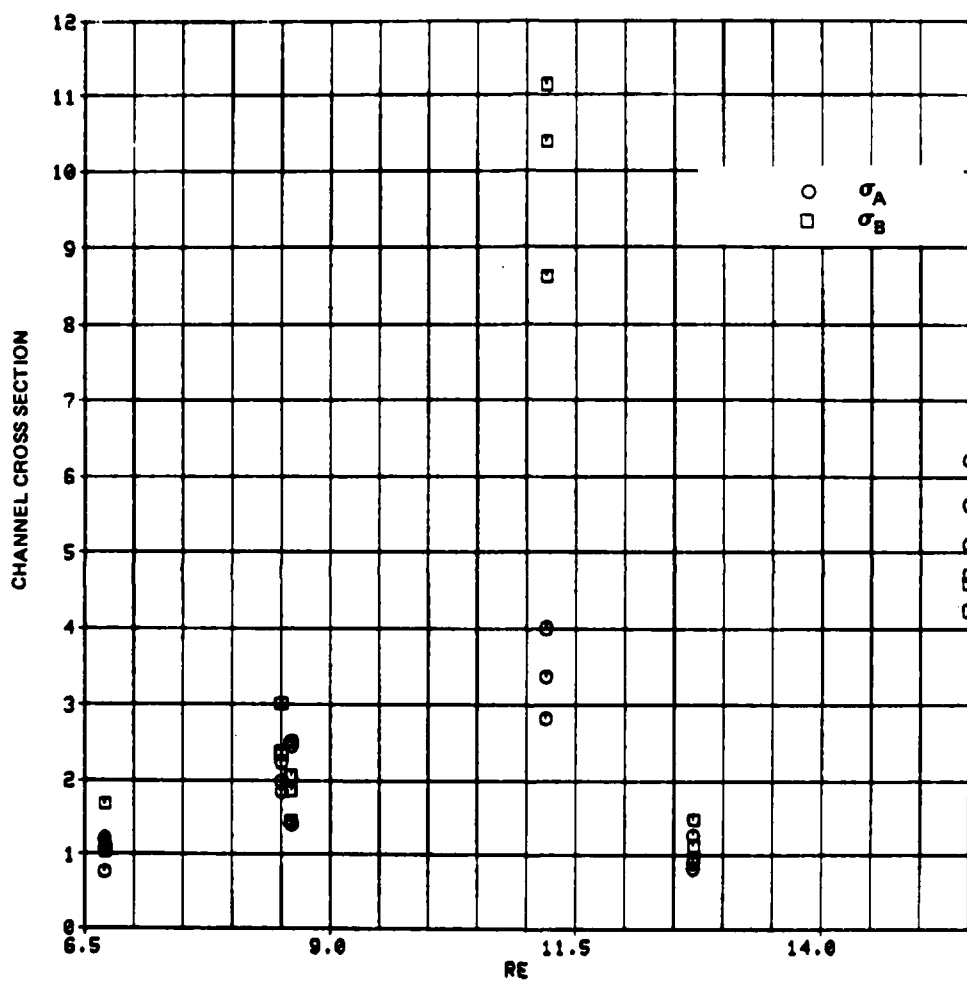


Figure 55. Channel Cross Section Versus Particle Equivalent Radius

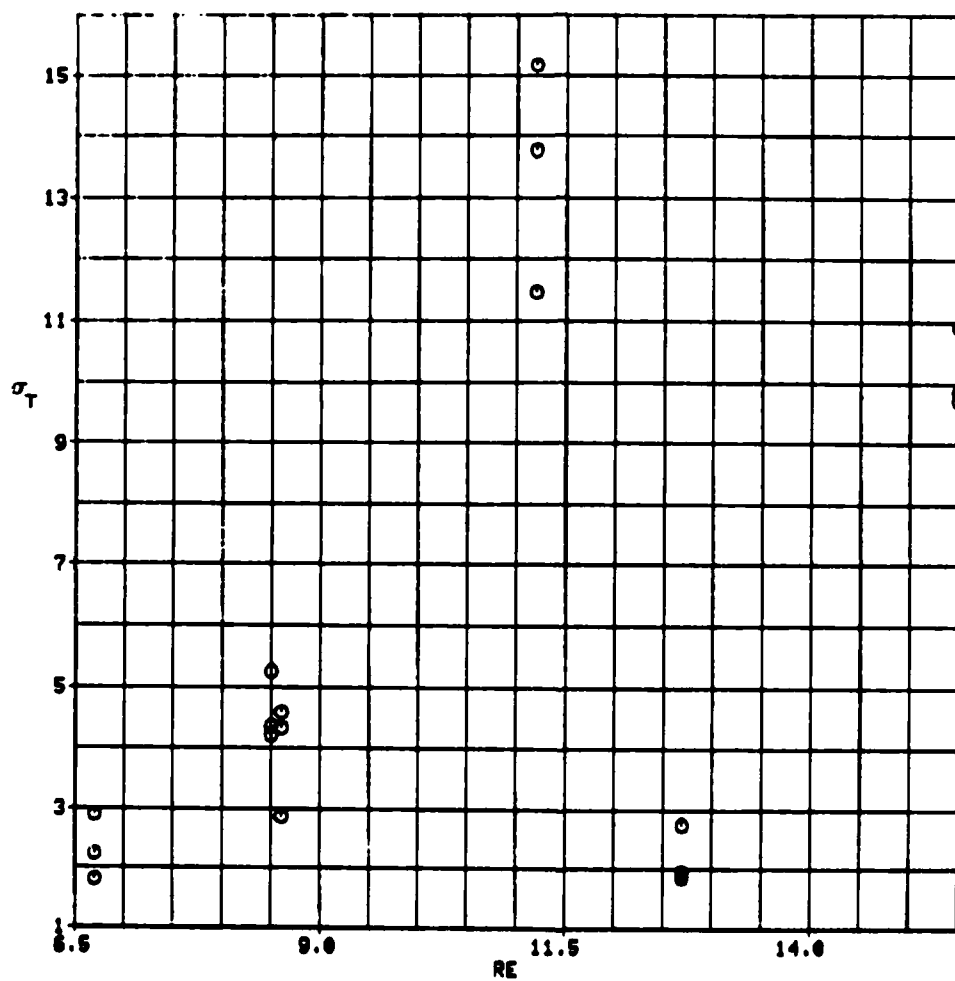


Figure 56. Total Cross Section Versus Particle Equivalent Radius

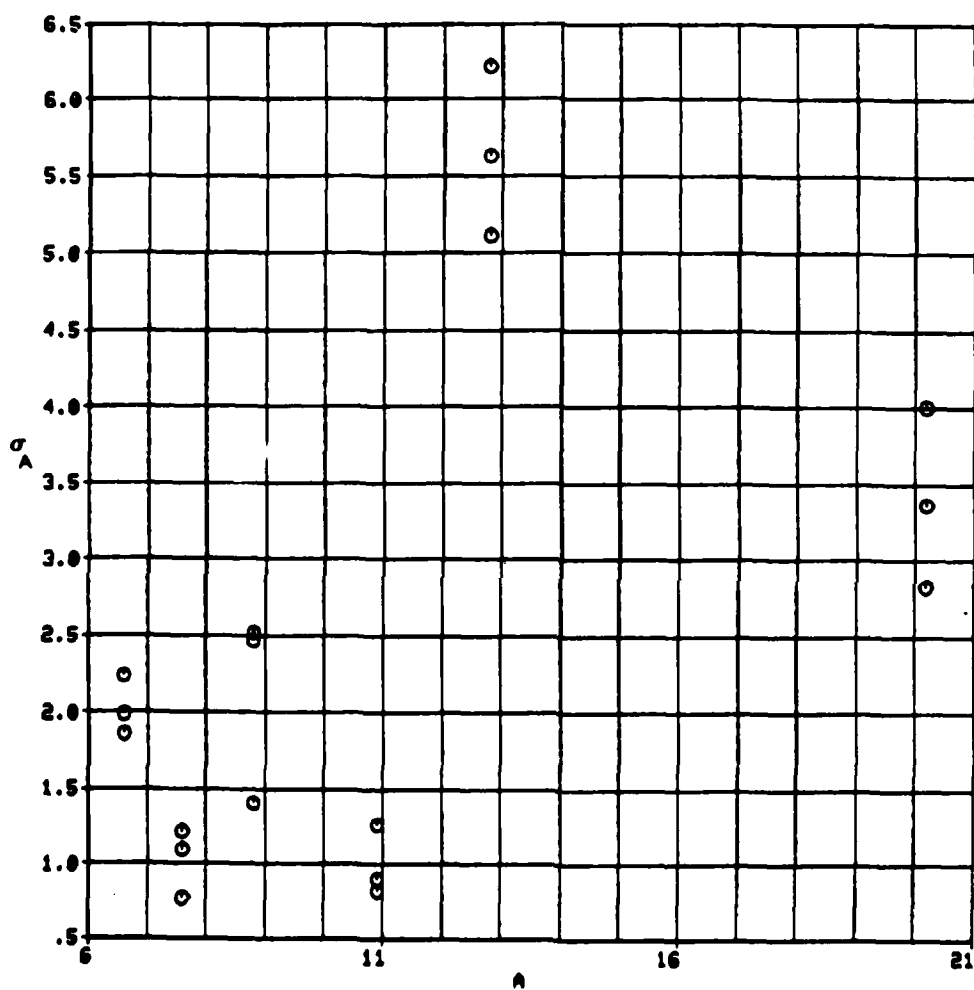


Figure 57. Channel A Cross Section Versus a Semi-Axis

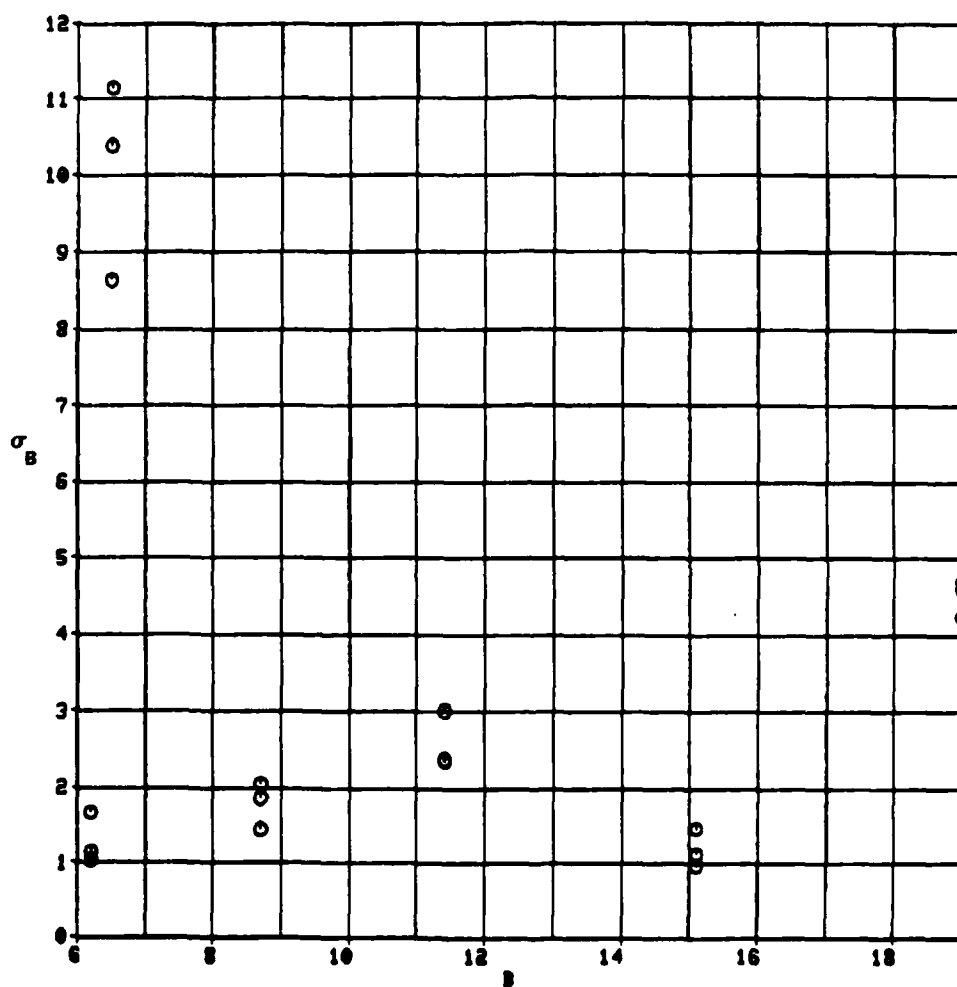


Figure 58. Channel B Cross Section Versus b Semi-Axis

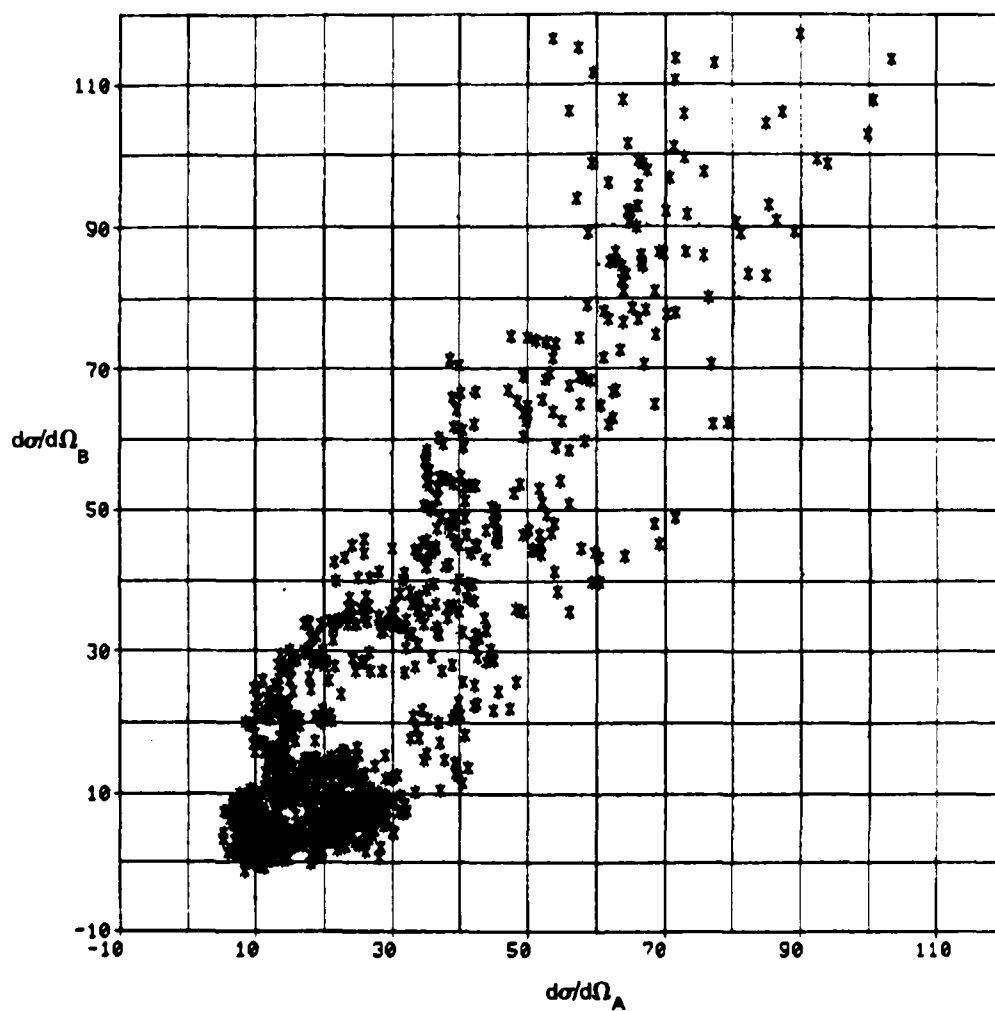


Figure 59. Scatter Plot, Channel B Versus Channel A, Particle 1, Sample 1

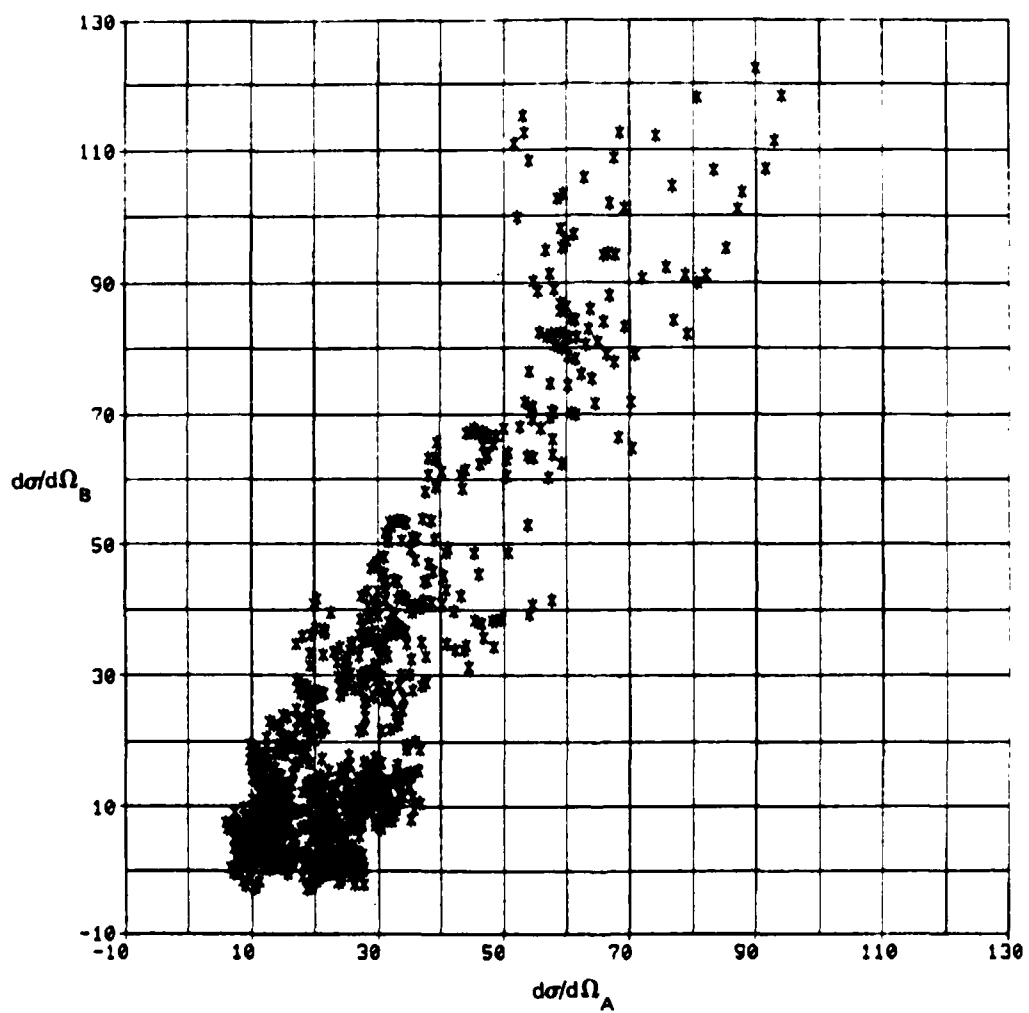


Figure 60. Scatter Plot, Channel B Versus Channel A, Particle 1,
Sample 2

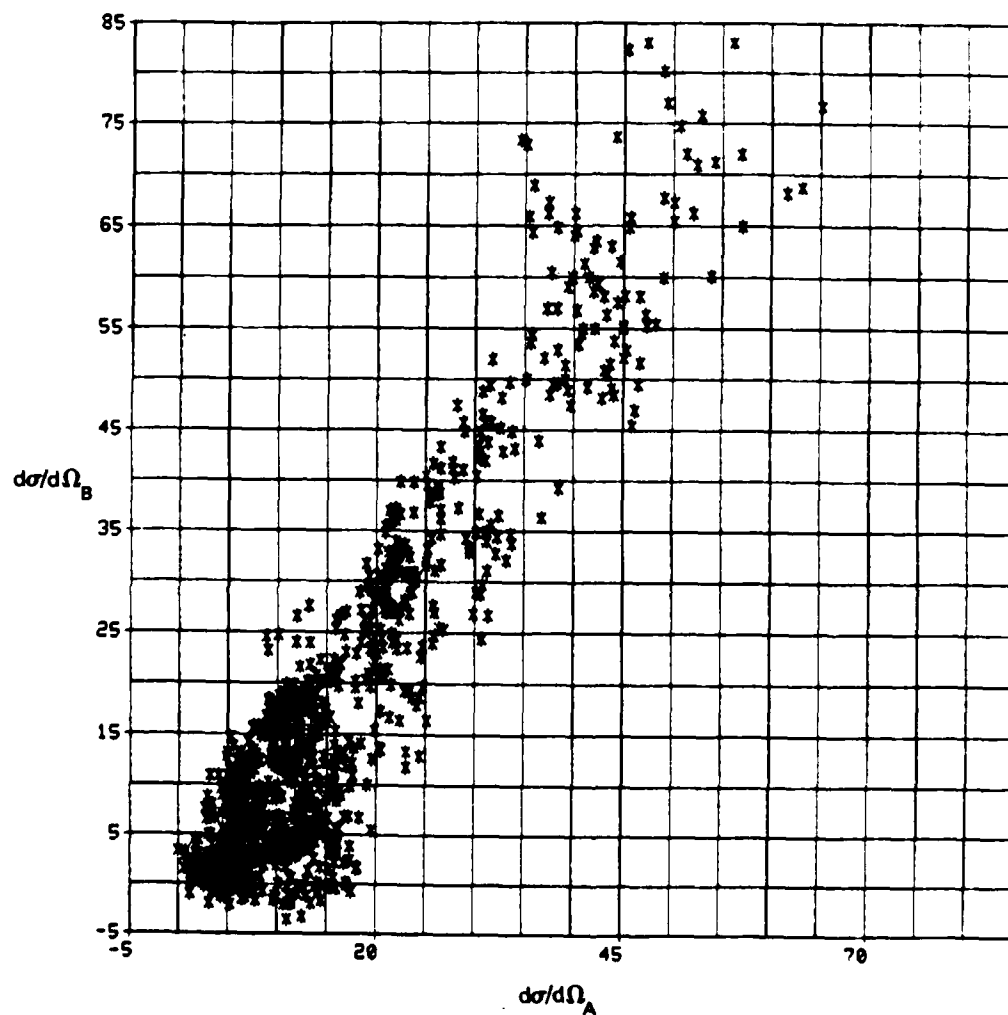


Figure 61. Scatter Plot, Channel B Versus Channel A, Particle 1, Sample 3

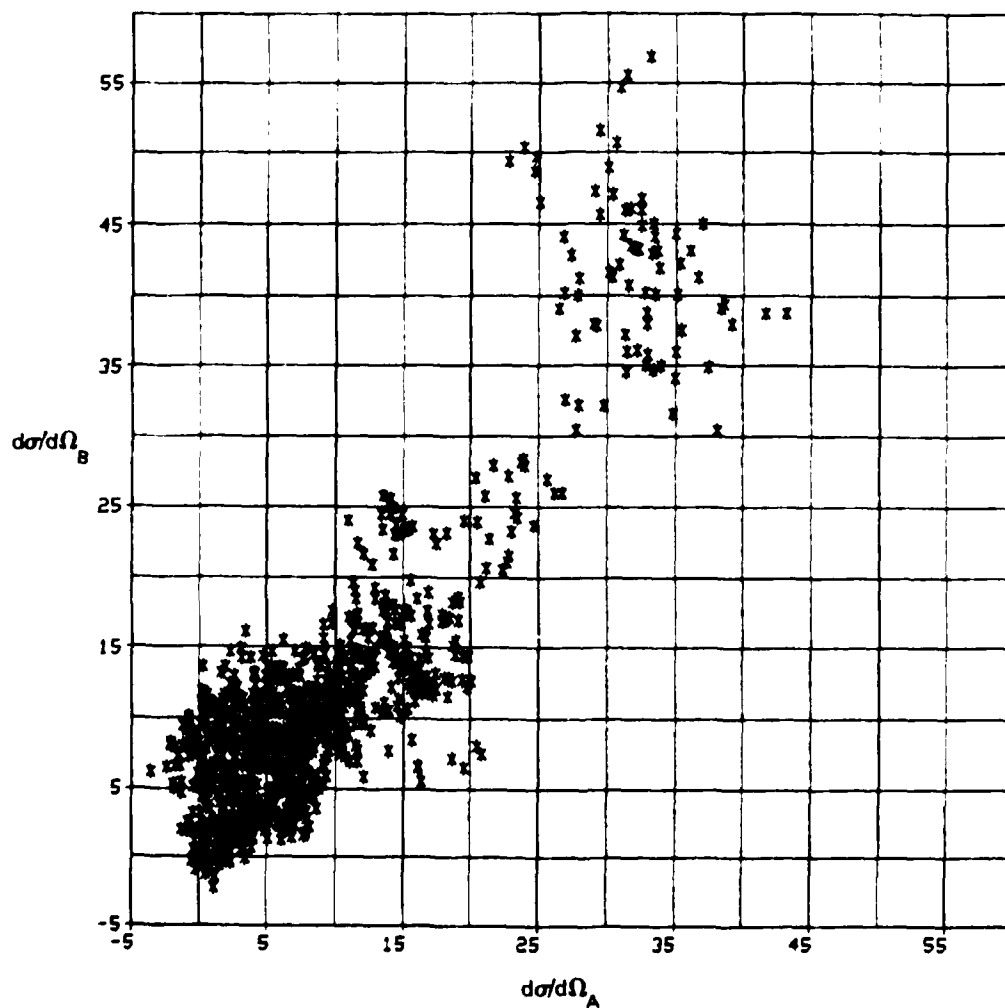


Figure 62. Scatter Plot, Channel B Versus Channel A, Particle 2, Sample 1

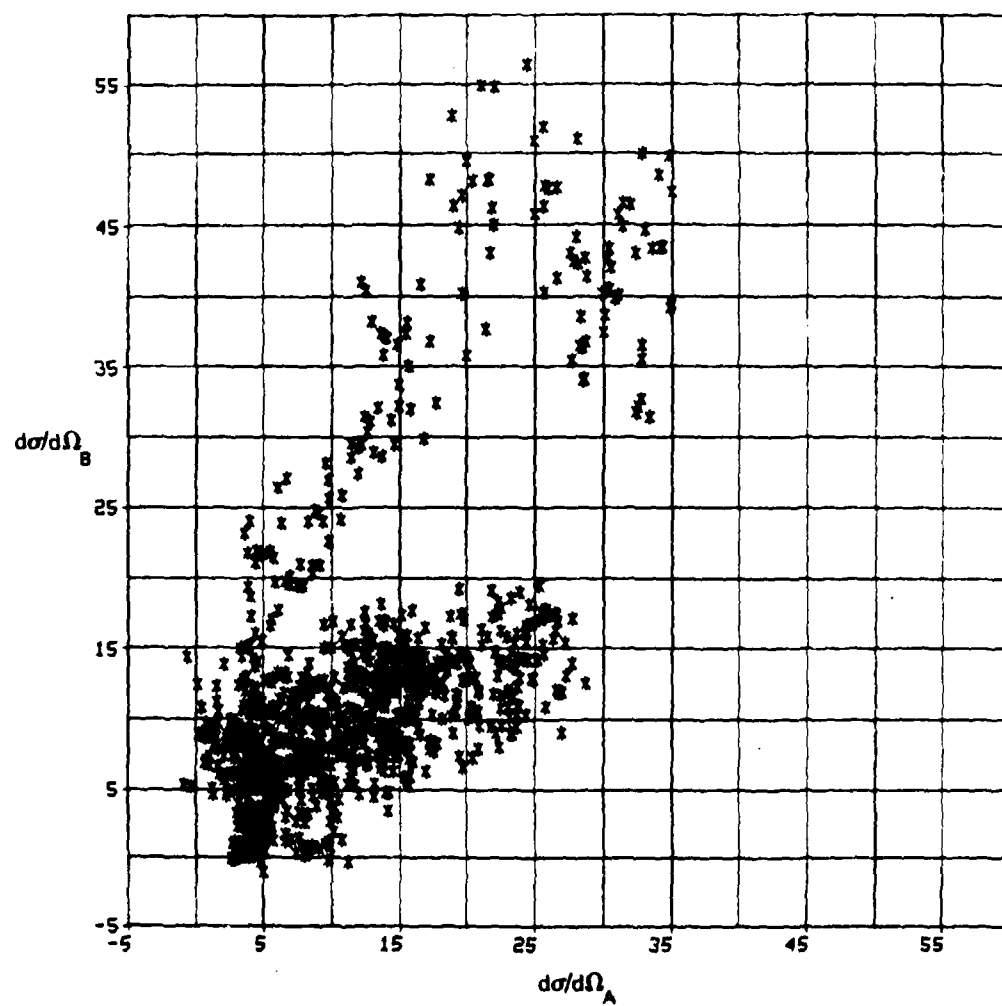


Figure 63. Scatter Plot, Channel B Versus Channel A, Particle 2, Sample 2

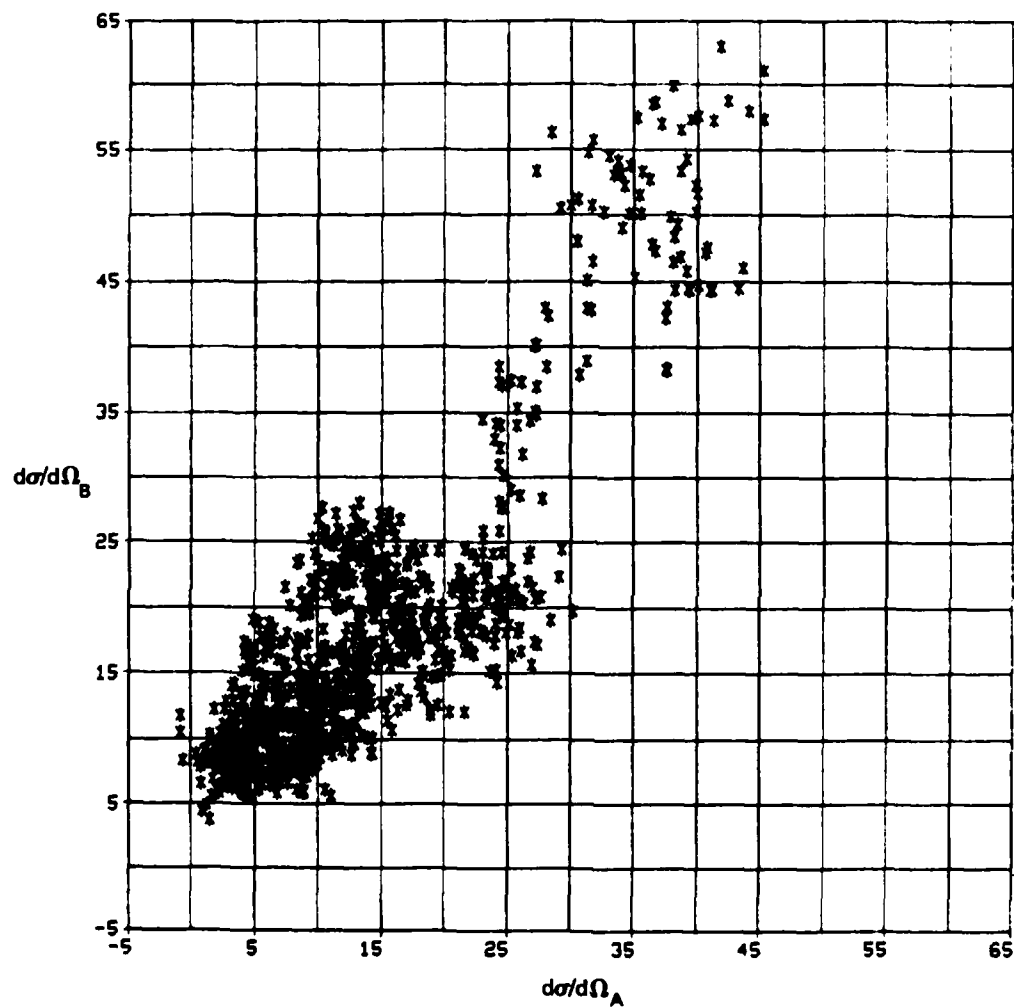


Figure 64. Scatter Plot, Channel B Versus Channel A, Particle 2, Sample 3

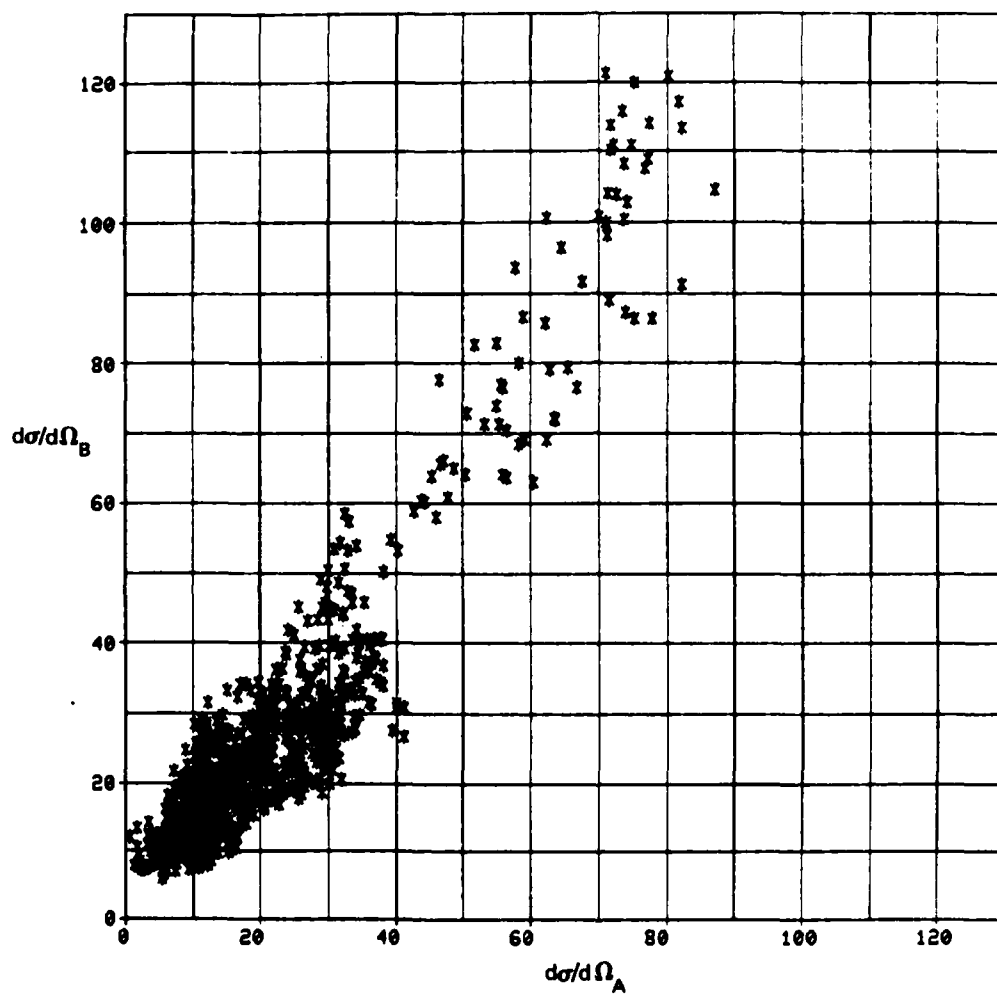


Figure 65. Scatter Plot, Channel B Versus Channel A, Particle 3,
Sample 1

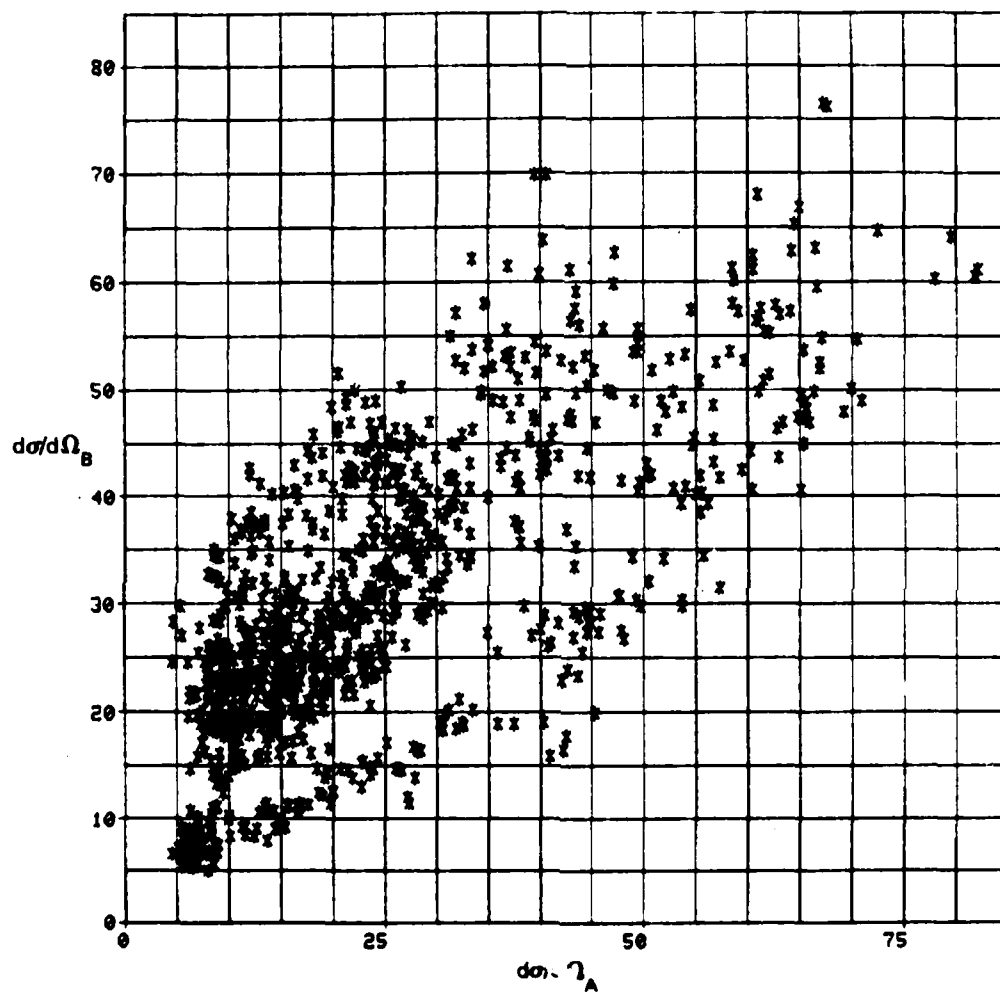


Figure 66. Scatter Plot, Channel B Versus Channel A, Particle 3, Sample 2

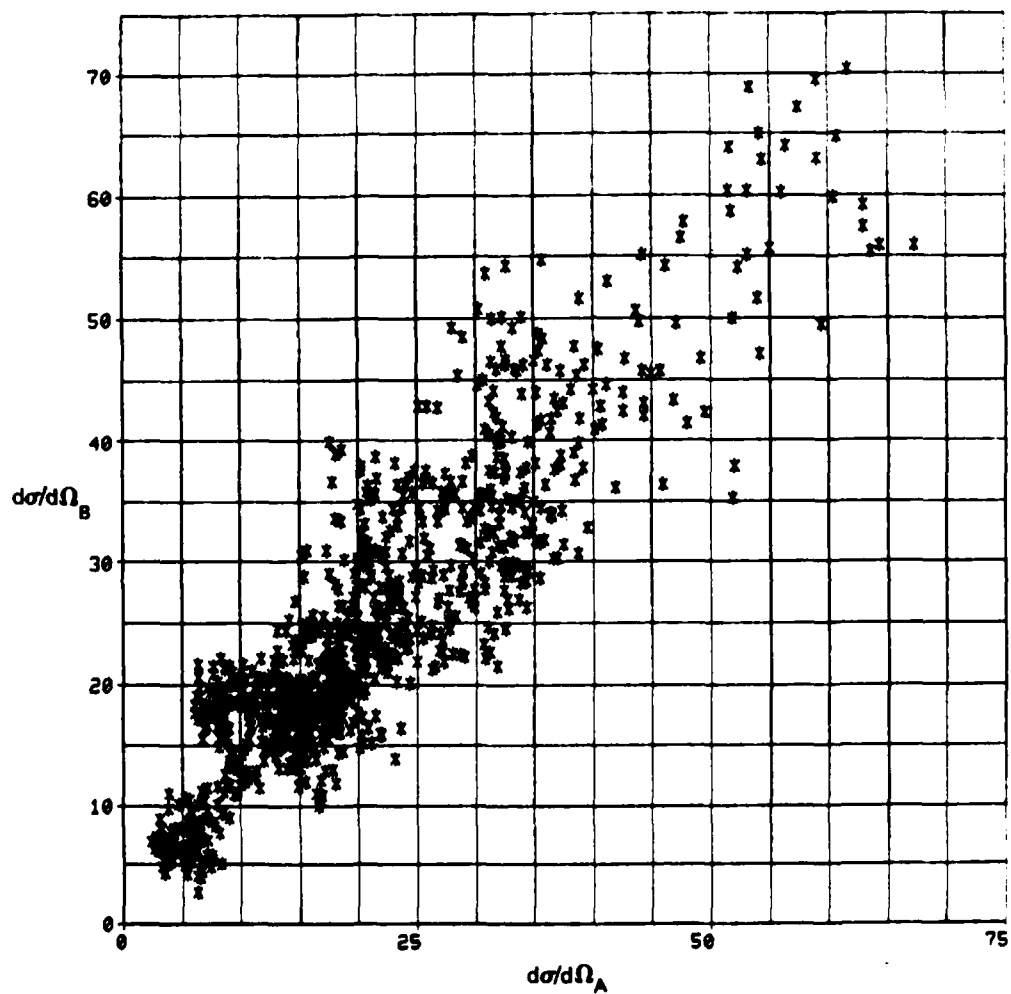


Figure 67. Scatter Plot, Channel B Versus Channel A, Particle 3, Sample 3

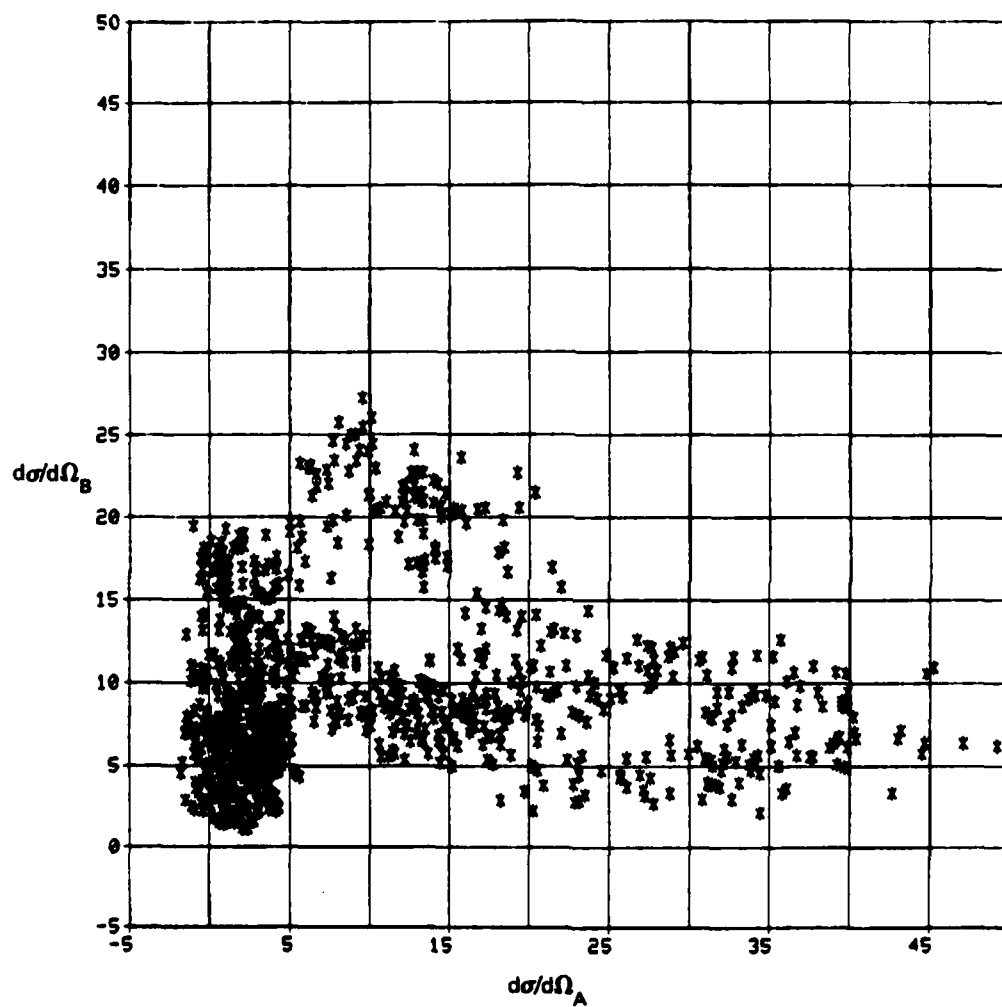


Figure 68. Scatter Plot, Channel B Versus Channel A, Particle 4, Sample 1

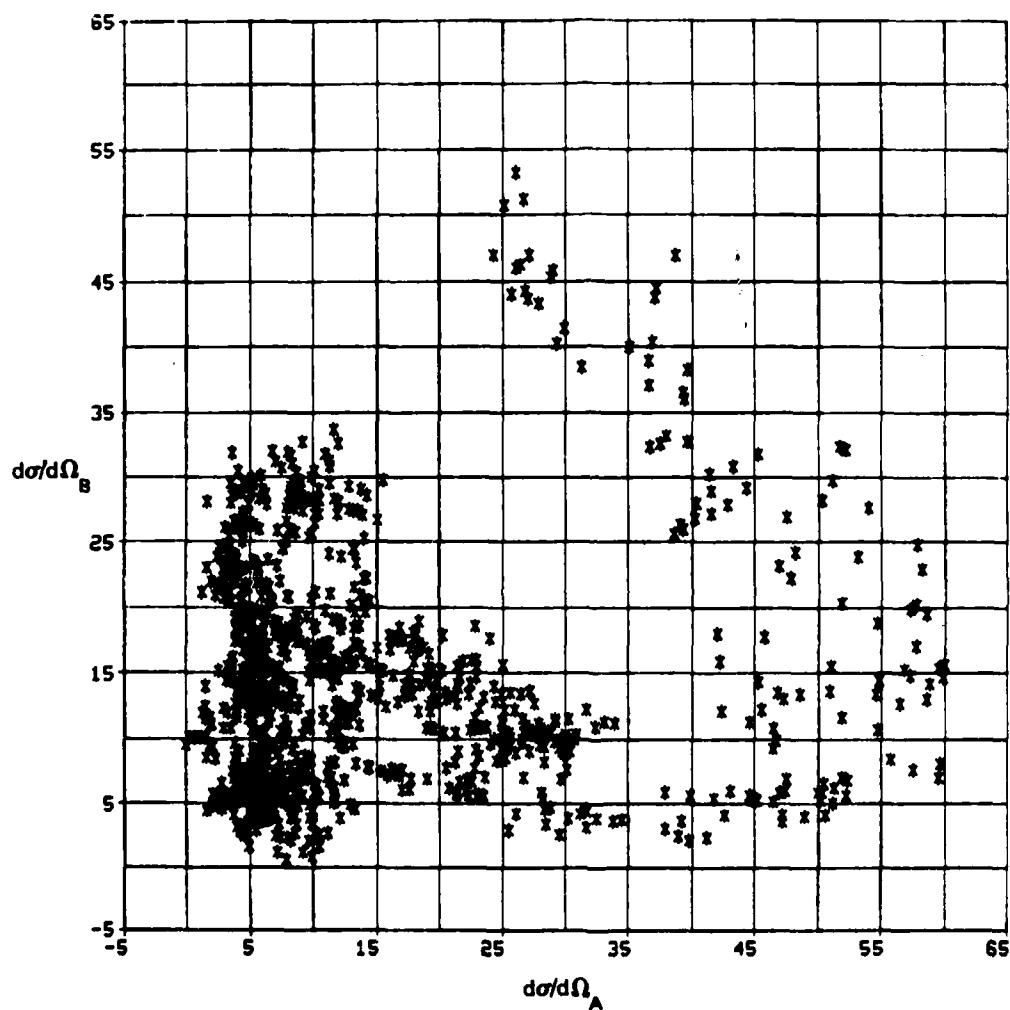


Figure 69. Scatter Plot, Channel B Versus Channel A, Particle 4, Sample 2

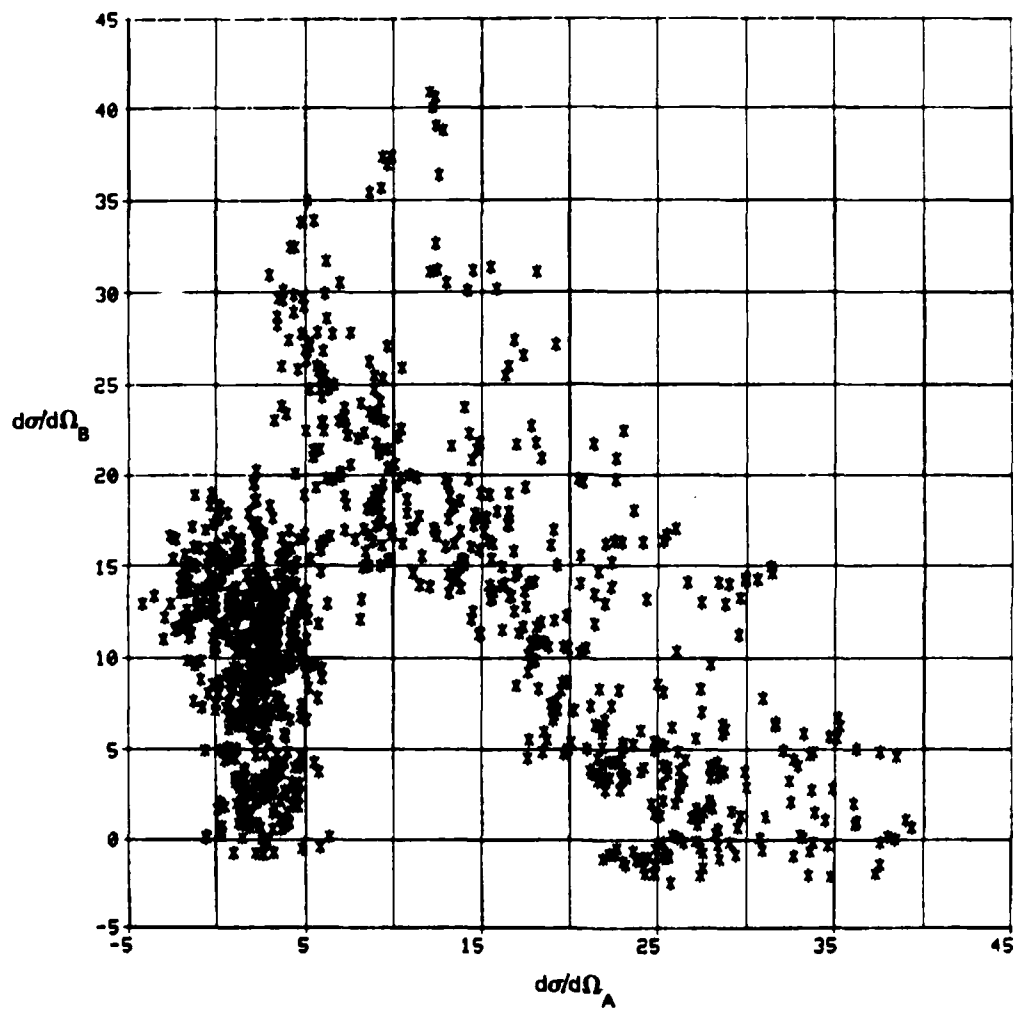


Figure 70. Scatter Plot, Channel B Versus Channel A, Particle 4, Sample 3

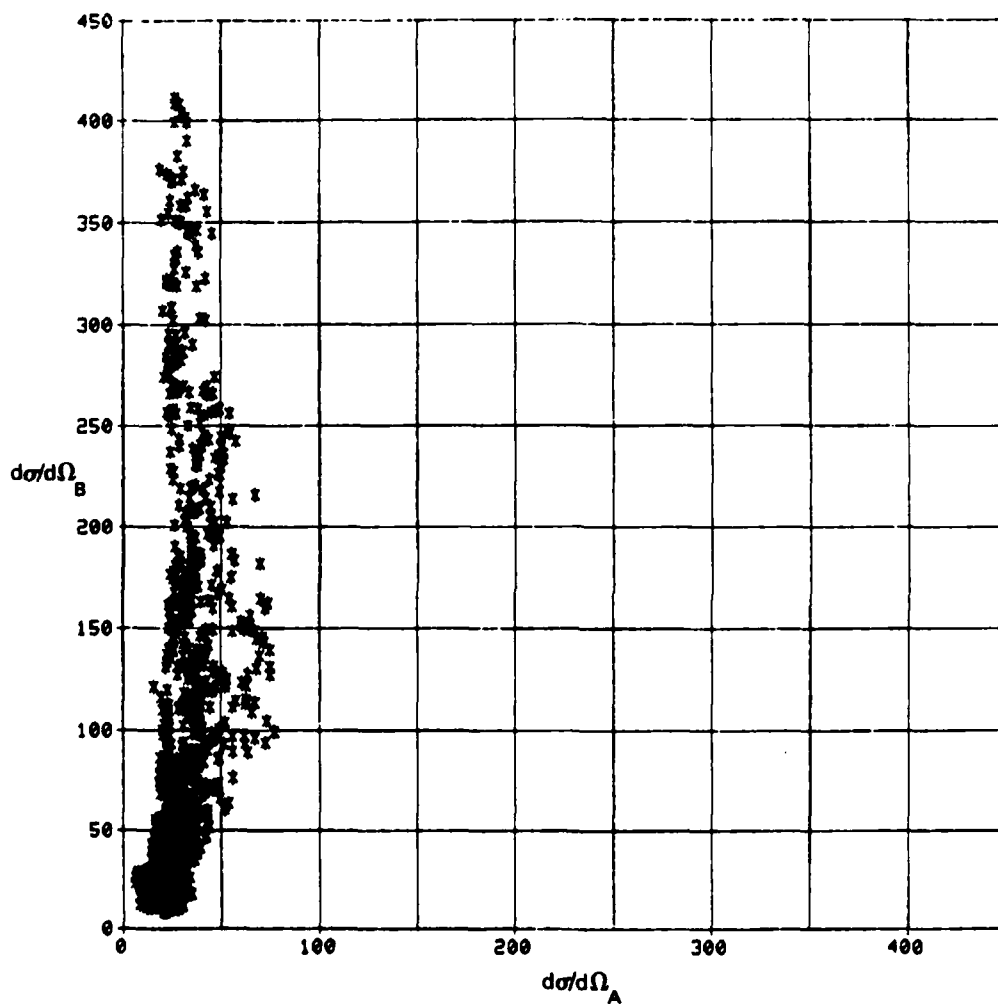


Figure 71. Scatter Plot, Channel B Versus Channel A, Particle 5, Sample 1

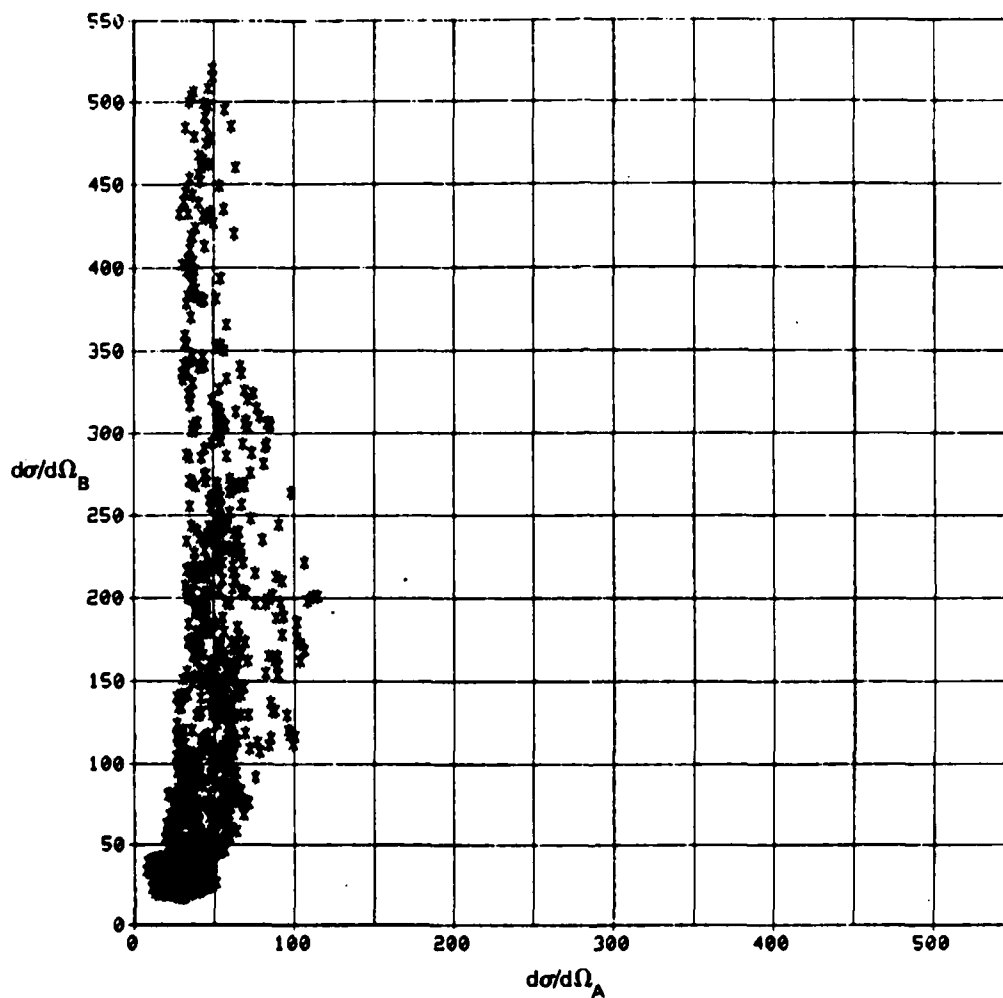


Figure 72. Scatter Plot, Channel B Versus Channel A, Particle 5, Sample 2

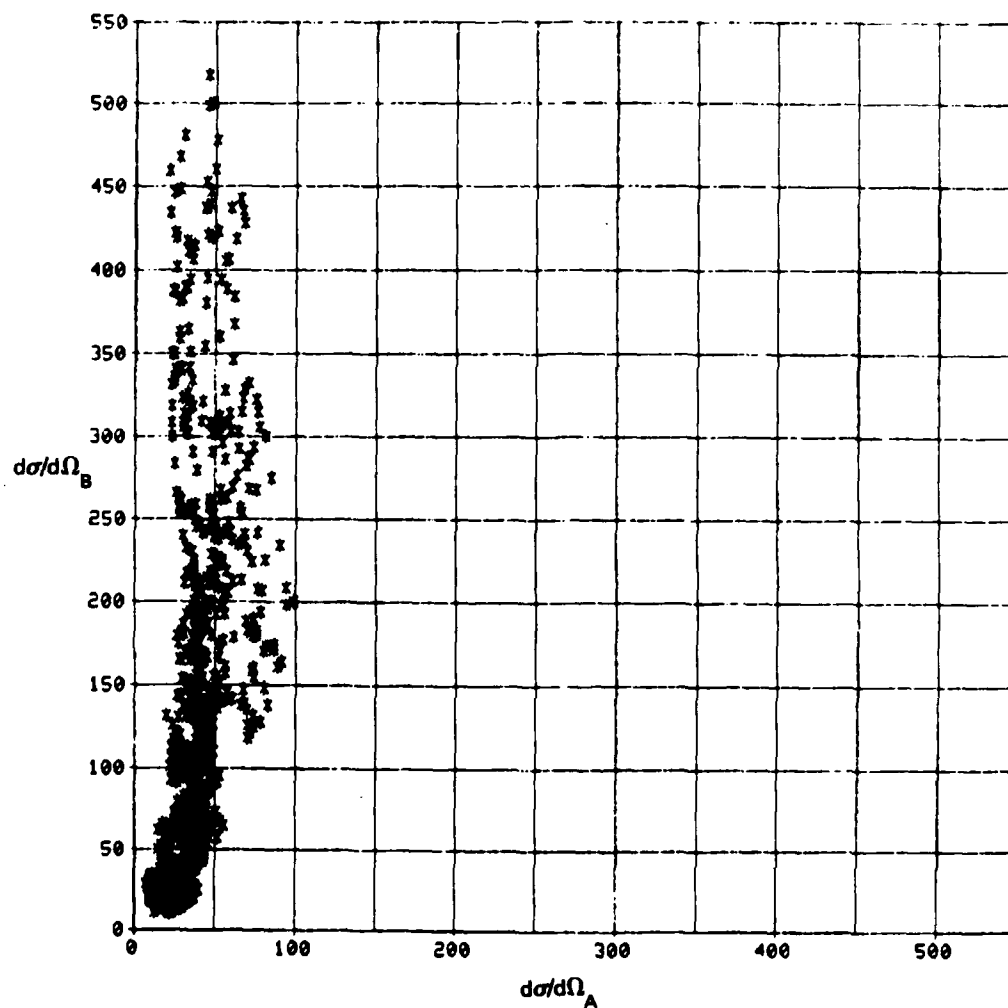


Figure 73. Scatter Plot, Channel B Versus Channel A, Particle 5, Sample 3

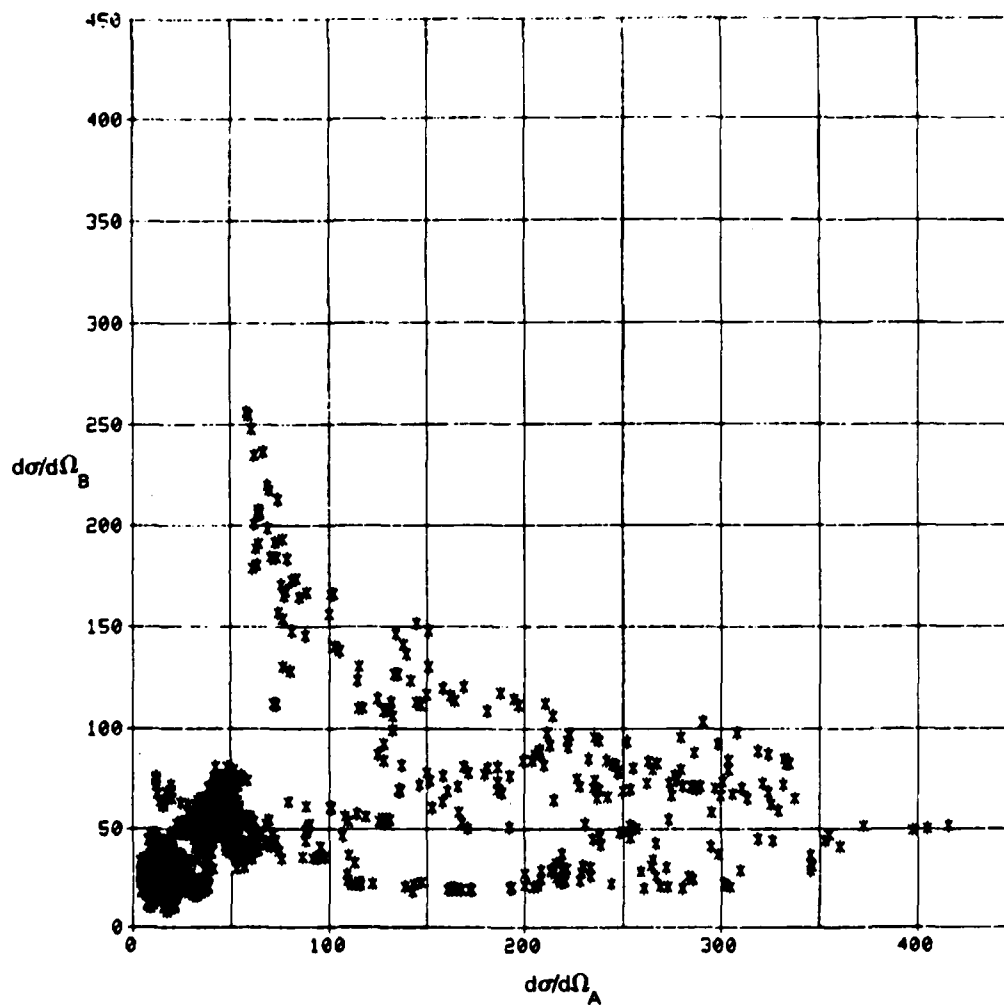


Figure 74. Scatter Plot, Channel B Versus Channel A, Particle 6, Sample 1

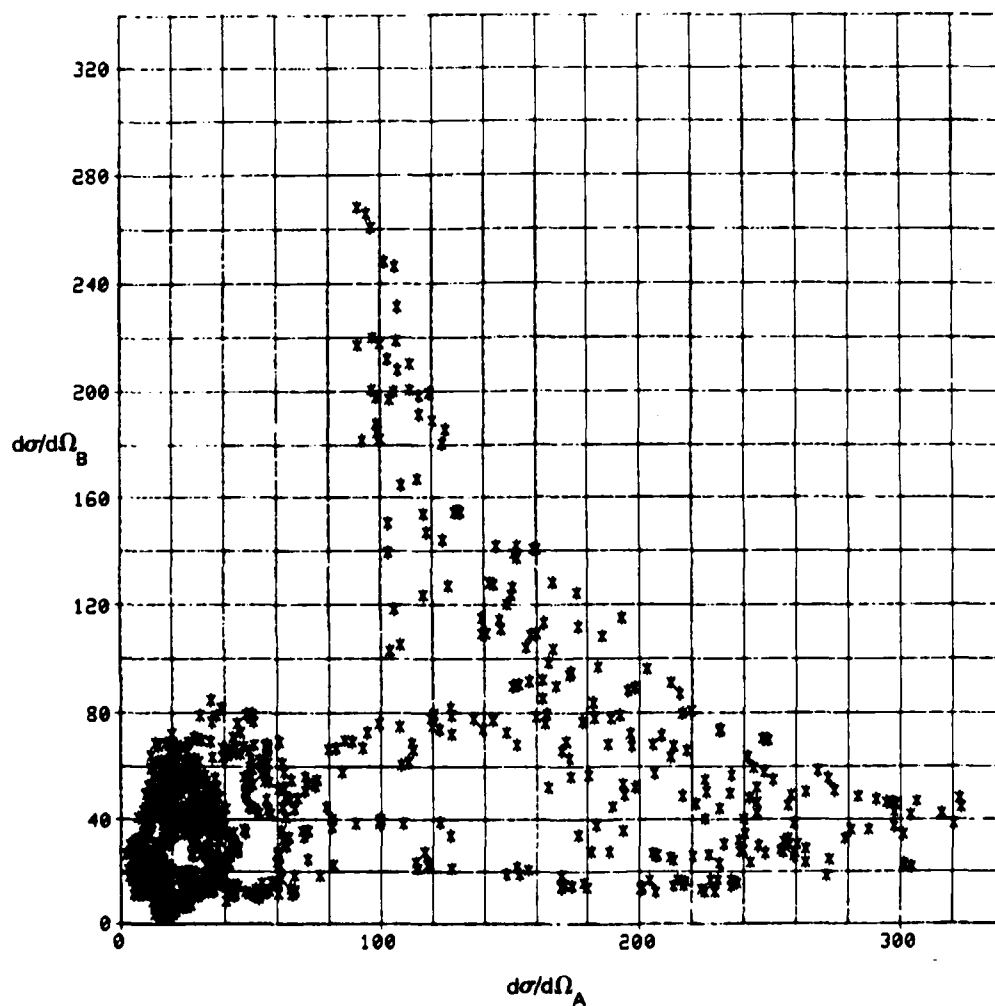


Figure 75. Scatter Plot, Channel B Versus Channel A, Particle 6, Sample 2

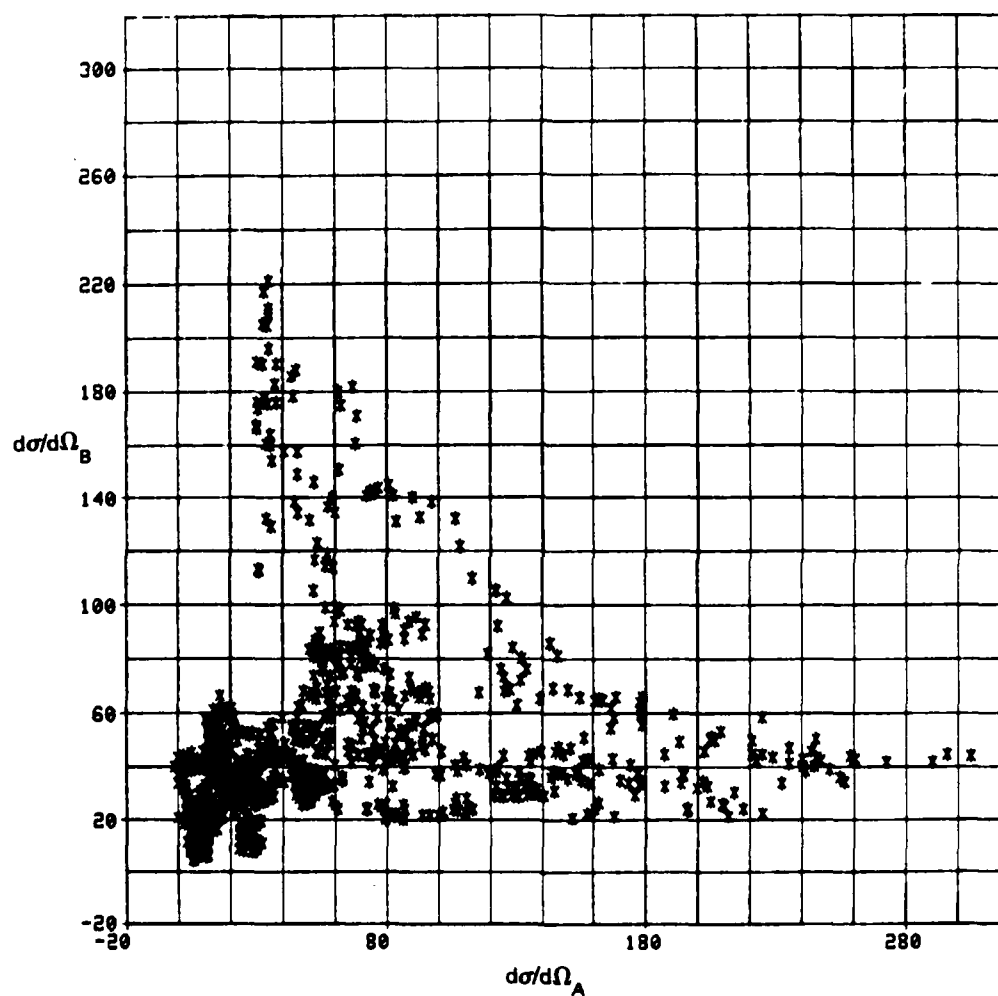


Figure 76. Scatter Plot, Channel B Versus Channel A, Particle 6, Sample 3

AD-A151 981

PARTICLE SHAPE CHARACTERIZATION(U) BOEING AEROSPACE CO
SEATTLE WA C D CAPPS OCT 84 N00014-83-C-2151

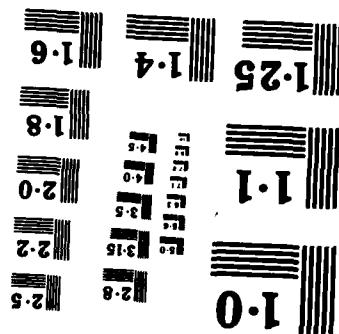
2/2

UNCLASSIFIED

F/G 20/6

NL

			END
			FILED
			DATE



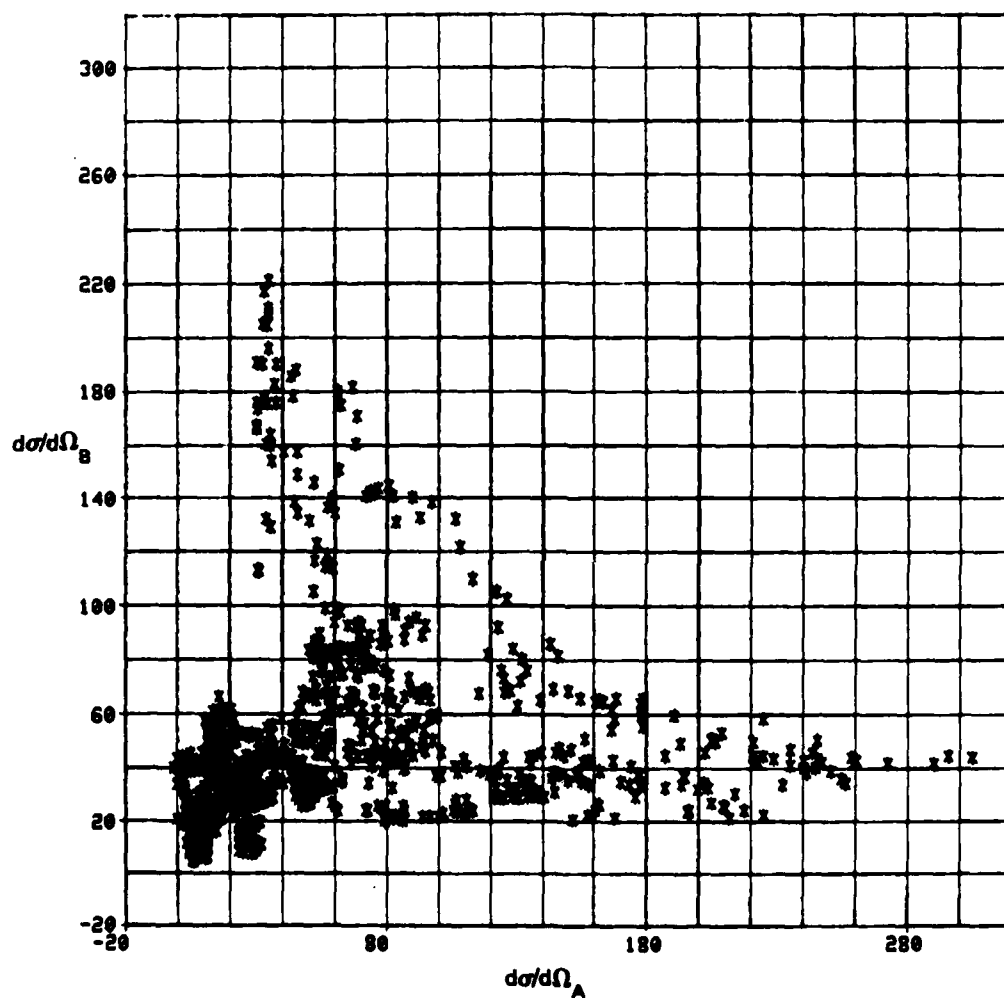


Figure 76. Scatter Plot, Channel B Versus Channel A, Particle 6, Sample 3

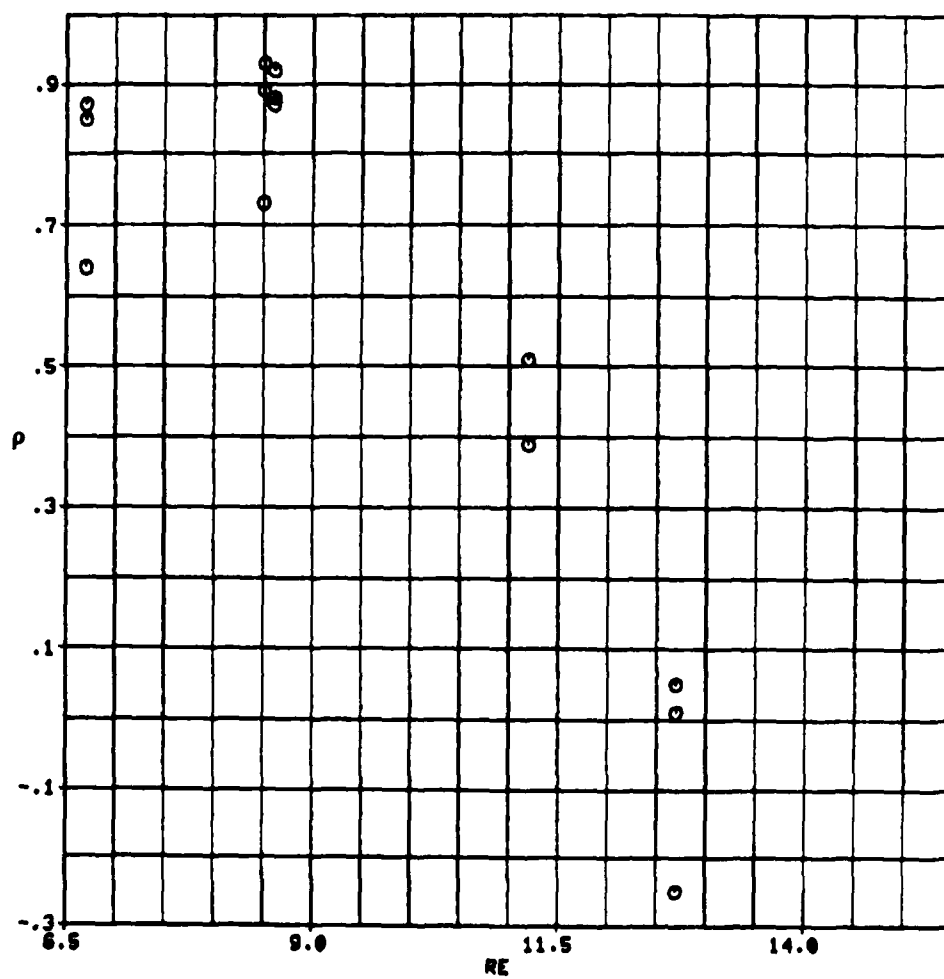


Figure 77. Correlation Coefficient Versus Equivalent Radius

END

FILMED

5-85

DTIC

